Breaking symmetry in time-dependent electronic structure theory to describe spectroscopic properties of non-collinear and chiral molecules.

Joshua James Goings

A dissertation
submitted in partial fulfillment of the
requirements for the degree of

Doctor of Philosophy

University of Washington

2017

Reading Committee:

Xiaosong Li, Chair

David Masiello

Stefan Stoll

Program Authorized to Offer Degree:
Chemistry

University of Washington

Abstract

Breaking symmetry in time-dependent electronic structure theory to describe spectroscopic properties of non-collinear and chiral molecules.

Joshua James Goings

Chair of the Supervisory Committee:
Professor Xiaosong Li
Department of Chemistry

Time-dependent electronic structure theory has the power to predict and probe the ways electron dynamics leads to useful phenomena and spectroscopic data. Here we report several advances and extensions of broken-symmetry time-dependent electronic structure theory in order to capture the flexibility required to describe non-equilibrium spin dynamics, as well as electron dynamics for chiroptical properties and vibrational effects. In the first half, we begin by discussing the generalization of self-consistent field methods to the so-called two-component structure in order to capture non-collinear spin states. This means that individual electrons are allowed to take a superposition of spin-1/2 projection states, instead of being constrained to either spin-up or spin-down. The system is no longer a spin eigenfunction, and is known a a spin-symmetry broken wave function. This flexibility to break spin symmetry may lead to variational instabilities in the approximate wave function, and we discuss how these may be overcome. With a stable non-collinear wave function in hand, we then discuss how to obtain electronic excited states from the non-collinear reference, along with associated challenges in their physical interpretation. Finally, we extend the two-component methods to relativistic Hamiltonians, which is the proper setting for describing spin-orbit driven phenomena. We describe the first implementation of the explicit time propagation of relativistic two-component methods and how this may be used to capture spin-forbidden states in electronic absorption

spectra. In the second half, we describe the extension of explicitly time-propagated wave functions to the simulation of chiroptical properties, namely circular dichroism (CD) spectra of chiral molecules. Natural circular dichroism, that is, CD in the absence of magnetic fields, originates in the broken parity symmetry of chiral molecules. This proves to be an efficient method for computing circular dichroism spectra for high density-of-states chiral molecules. Next, we explore the impact of allowing nuclear motion on electronic absorption spectra within the context of mixed quantum-classical dynamics. We show that nuclear motion modulates the electronic response, and this gives rise to infrared absorption as well as Raman scattering phenomena in the computed dynamic polarizability. Finally, we explore the accuracy of several perturbative approximations to the equation-of-motion coupled-cluster methods for the efficient and accurate prediction of electronic absorption spectra.

TABLE OF CONTENTS

LIST OF FIGURES

Figure Number Page

LIST OF TABLES

GLOSSARY

2C : Two-component

AE : Absolute error

AO : Atomic orbital

B3LYP : Becke 3-parameter hybrid exchange functional with Lee-Yang-Parr correlation

BCH : Baker-Campbell-Hausdorff

CC2 : Second-order approximate coupled cluster with singles and doubles

CCSD : Coupled cluster with singles and doubles

CIS : Configuration interaction singles

CIS(D) : Configuration interaction singles with perturbative doubles

DFT : Density functional theory

DKH : Douglas-Kroll-Heß

ECD : Electronic circular dichroism

ECP : Effective core potential

EOM : Equation-of-motion

FCI : Full configuration interaction

FWHM : Full-width at half-maximum

GHF : Generalized Hartree-Fock

GIAO : Gauge-including atomic orbitals

HF : Hartree-Fock

KS : Kohn-Sham

LANL2DZ: Los Alamos National Laboratory double-zeta basis with associated ECP

LR : Linear response

MBPT2 : Many-body perturbation theory through second order

MMUT : Modified midpoint unitary transformation

MO : Molecular orbital

MP2 : Møller-Plesset second-order perturbation theory

MSE : Mean signed error

NESC : Normalized elimination of the small component

P-EOM : Partitioned equation-of-motion

PBEPBE : Perdew-Burke-Ernzerhof exchange correlation functional

PHF : Projected Hartree-Fock

RHF : Restricted Hartree-Fock

RMS : Root-mean-squared

ROHF : Restricted open-shell Hartree-Fock

RPA : Random-phase approximation

RT : Real-time

SAC-CI : Symmetry-adapted cluster configuration interaction

SCF : Self-consistent field

TD : Time-dependent

UHF : Unrestricted Hartree-Fock

VCD : Vibrational circular dichroism

X2C : Exact two-component

ZORA : Zeroth-order regular approximation

ACKNOWLEDGMENTS

It is somewhat ironic that despite being in school for over twenty-two years now, I feel my journey is really only just beginning. I am firstly thankful to God for having given me the opportunity and ability to study the universe we live in. For me, scientific creativity — particularly through theory-building — is one of the deepest ways I can participate in the *imago dei*. Yet this process is never an individual one, and as I begin my next steps, I would be remiss not to thank the many people who have made this journey possible.

This journey would not have been possible without the support and encouragement of my advisor, Prof. Xiaosong Li. Xiaosong, without your enthusiasm and optimism I would not be where I am today. I am also grateful that you prioritized traveling as a graduate student, as well as the importance of presenting my research to other scientists. I would also like to thank the members of the Li research group, in particular Dr. Joseph May, for teaching me elements of scientific design, Dr. Feizhi Ding, for making me a more rigorous mathematician, and David Williams-Young for helping me more times than I can count with programming. I am also grateful to Patrick Lestrange and David Lingerfelt for embarking on this journey with me, as well as Joe Kasper for many good discussions as well. To the rest (there are too many to name now): thank you.

To my committee: Profs. David Masiello, Stefan Stoll, Matt Bush, and Jim Pfaendtner. Your insights have been invaluable, in particular your constant reminders that good theory must always be in service to Nature.

I would also like to thank my professors at Seattle Pacific University for cultivating my excitement for science — particularly chemistry — very early on in my education. To Prof. Karisa Pierce, I will be grateful for the many opportunities to present my graduate research

each spring to the undergraduates at SPU. Learning to present research to undergraduates always gave me a sense of context for the journey I was on. To Prof. Benjamin McFarland, I always enjoyed our discussions, in particular the intersection of science and philosophy and science and society, especially in third quarter biochemistry. To Prof. Kevin Bartlett — I think you knew far before I did that I would become a theorist, and I am forever grateful that you got me excited about the power of molecular orbital theory as a way of understanding a wide, often disparate, range of phenomena. And finally to Prof. Daniel Schofield, who gave me my first opportunity to try my hand at theoretical chemistry. I will be forever grateful to the freedom you gave me to explore what was then a very foreign area of chemistry to me. The skills I gained before graduate school proved to be invaluable. I am also thankful for your example of a person who balanced being a good scientist with being a good person.

I also want to thank my family, both in Colorado as well as here in Washington for your support. Mom and Dad, thank you for always being supportive of my career in the sciences. The freedom you gave me to explore the world as a child in the kitchen or the workshop or out in nature has probably influenced my decision to be a scientist more than I can know. To Mark and Sherry, thank you for welcoming me into your family here in Washington — I have always valued your support. To my siblings, and siblings-in-law: Heather, Ron, Sara, Bryan and Kara, thank you for loving me each in your own unique way, and always reminding me that there is more to life than science.

Lastly, to Kristi: words cannot express how thankful I am for your love and encouragement throughout all this. I am thankful everyday for your patience and grace, especially listening to my joys and frustrations, though I know most of it sounded like nonsense to you (in my defense, I don't understand much of your medical jargon, either). I am excited that you will be joining me as we take our next steps together.

DEDICATION

To my parents,

who taught me a good head was useless without a good heart,

and,

To Kristi,

who helped me follow both.

PREFACE

This dissertation focuses primarily on time-dependent electronic structure theory as a tool for obtaining new types of spectroscopic and dynamical information. The primary advances are within two-component (or non-collinear) electronic structure theory which breaks many spin symmetry constraints on the wave function. This is used primarily for two reasons: first, it is often used to obtain a lower variational energy, and second, sometimes adding small physical terms to the underlying Hamiltonian breaks the spin symmetry anyway (e.g. spin-orbit coupling). For both cases, only two-component methods have sufficient flexibility to handle these situations (at least in the single-reference ansatz).

Chapter 1 serves as an introduction to the dissertation, primarily as an overview of some of the advances in non-collinear electronic structure theory I have made over my time at the University of Washington. It gives perspective into the utility of these two-component methods, especially towards studies of spin and magnetization dynamics, as well as its natural place as the foundation for a variational relativistic theory for quantum chemistry. The chapter is meant to be light on the mathematics, with a more formal treatment of generalized Hartree-Fock and its symmetries in Appendices A and B. In light of these opening remarks we move on to Chapter 2, where we explore the origins and implications of non-collinear instabilities within Hartree-Fock (and other single-reference) methods. Given that we teach our students about the "spin-up, spin-down" nature of molecular orbitals, it is surprising to see how this mental picture of electrons fails, but it points towards the need for better ways of handling strongly correlated molecules. The treatment in this chapter makes use of the Thouless parameterization of the single Slater determinant, of which a proof is given in Appendix C. This parameterization also allows us to present a coherent, though less

common, derivation of the Hartree-Fock equations based on orbital rotations in Appendix A. This treatment naturally leads to a derivation of the two-component stability conditions in Chapter 2.

From here we move onto a study of how (non-relativistic) two-component methods describe excited states in Chapter 3. We show how two-component methods break spin symmetry in the presence of a degenerate ground state, much akin to a Jahn-Teller distortion in the spin manifold, and we explore the impact this spin symmetry breaking has on the description of electronic excited states. With this in mind we extend to a relativistic description of excited states in Chapter 4, where we obtain various spin-orbit split excited states through the explicit time propagation of the so-called "exact" relativistic two-component equations.

At this point we leave the world of two-component methodologies and explore some less conventional approaches to computing different types of spectra within time-dependent electronic structure theory. In Chapter 5 we explore a method for obtaining chiroptical properties (namely circular dichroism spectra) of chiral molecules within the explicit time propagation of the time-dependent density functional equations. Chiral molecules break parity symmetry, and this manifests itself in differing enantiomeric responses to left- and right-handed circularly polarized light. Later, in Chapter 6 we explore the effect of moving nuclei on electronic absorption spectra, showing how the Ehrenfest method can be used to obtain infrared, Raman, and absorption spectra in a single simulation. Finally, in Chapter 7 we explore economical approaches to including electron correlation in the computation of electronic absorption spectra, by truncating the so-called equation-of-motion coupled-cluster theory equations through a perturbation expansion. A detailed derivation of the approximation can be found in Appendix D.

Chapter 1

PERSPECTIVES ON NON-COLLINEAR AND TWO-COMPONENT ELECTRONIC STRUCTURE THEORY

Here we review recent developments in non-collinear electronic structure theory. After a brief historical overview of studies into broken-symmetry wave functions, we show that non-collinear wave functions are necessary for studying spin and magnetic phenomena on account of spin-symmetry breaking terms in the Hamiltonian. Recent developments applying non-collinear electronic structure theory to magnetization dynamics, spin dynamics, and spin-orbit coupling in excited-state properties are showcased. We also discuss some recent developments in non-collinear density functional theory. Finally, we comment on the future of non-collinear electronic structure theory. The work in this chapter was adapted with permission from Joshua J. Goings, Franco Egidi, and Xiaosong Li. Current development of noncollinear electronic structure theory. *Int J Quantum Chem.*, 2017;00:e25398.

History of broken spin symmetry Hartree-Fock

Mean-field, and self-consistent field (SCF), methods are the backbone of modern electronic structure theory. Since the introduction of the single-determinant ansatz by Hartree and Fock (see Appendix A), there has been a great deal of work on understanding the nature of the Hartree-Fock (HF) solutions as well as how to improve their utility in the description of atoms and molecules. It was recognized early on that the solution of the Hartree-Fock equations required a balance between two (sometimes competing) goals.[2–6] The first was that the Hartree-Fock equations would be at a variational minimum: the best SCF solution would be the lowest energy single-determinant approximation to the full configuration interaction

(FCI) equations (for a given basis). Solutions of the HF equations would always seek to find the lowest possible energy solution, so as to satisfy the variational principle. On the other hand, it was known that the underlying electronic Hamiltonian is invariant to several unitary transformations, most notably spin rotations. This invariance expresses itself as a conservation law, and the conserved quantity is total spin angular momentum S^2 as well as the spin projection along an arbitrary axis, S_z. Surely a physically meaningful solution of the HF approximation would also have good quantum numbers, so invariance to rotations in the spin manifold was built-in to the Hartree-Fock equations as a constraint in the single determinantal expression. For example, the restricted Hartree-Fock (RHF) equations contain only paired electrons in orbitals, yielding solutions with good spin quantum numbers. For a more detailed treatment of the continuous symmetries of the Hartree-Fock model, refer to Appendix B.

Unfortunately, it was quickly found that there are many cases where insisting that the HF solution be a spin eigenstate yields energies that are higher than they would otherwise be if spin symmetry constraints were relaxed. For example, in the classic example of the dissociation of H_2 one finds that when the bond is stretched to a certain distance (the Coulson-Fischer point) an RHF-to-UHF instability forms and qualitatively correct dissociation curve are obtained only in the spin symmetry broken state. The spin symmetry breaking arises when the solutions approach a (near) degeneracy. Hartree-Fock solutions are unstable in the presence of a degeneracy, and will mix in solutions of different spin character so as to lower the energy and avoid the degeneracy. This is well known for spin doublets, which are always doubly degenerate in the absence of an external magnetic field by Kramers theorem. Since doublets are always at least doubly degenerate, single-reference RHF solutions must break spin symmetry to form unrestricted (UHF) solutions; restricted open-shell (ROHF) solutions will always have a higher energy. The fact is that to have good quantum numbers, a symmetric variational solution will always introduce constraints and, in the context of variational methods, constraints can only lead to a solution of higher energy. The choice then, between good quantum numbers and the lowest energy HF solution is, for the practicing

quantum chemist, a "symmetry dilemma", as it was termed by Löwdin in 1963.[2]

Abandoning all good spin quantum numbers led to the generalized Hartree-Fock method (GHF), which was found to be the variational minimum for several molecular systems, primarily when the point group symmetry of the molecule forced a spatially degenerate ground state, such as the case of the equilateral H_3 triangle. A detailed history of the early GHF method can be found in Reference 5. The GHF solution is indeed the lowest-energy solution for many cases (see Chapter 2), but how closely do these broken-symmetry solutions represent reality as a model? Removing all possible symmetry constraints may not lead to a meaningful chemical model.

At the same time, many physical systems are known to spontaneously break symmetry.[7] For example, permanent ferromagnets arise from the spontaneous breaking of time reversal (and, implicitly, spin rotation) symmetry. The rigid lattice of solids is the result of breaking continuous translation symmetry. Yet spontaneous symmetry breaking is usually valid only for large collections of particles, where restoration of symmetry requires large amounts of energy, far beyond thermal and quantum fluctuations. One must make a distinction between artifactual and spontaneous symmetry breaking. This is a point that has been very clearly brought to the quantum chemical community in recent years by the Scuseria group (see References 8, 9 and citations therein). Because symmetry breaking is the by-product of a mean-field description, it can be considered artifactual. In practice, restoration of broken-symmetry states for molecular systems serves to lower the energy further. For true spontaneous symmetry broken states, restoration of symmetry via projection operators will not lower the energy of the system.

There are, however, cases of molecular systems where a broken-symmetry description is necessary. These are systems where a certain continuous symmetry is broken by symmetry breaking terms in the Hamiltonian — either from an external force, such as from an external magnetic field, or an internal force, such as the spin-orbit operator from a relativistic Hamiltonian. In these cases, the symmetry breaking is a product of the underlying physics. For phenomena involving magnetic fields and spin-orbit couplings, a spin non-collinear

approach must be used.

Stability and broken-symmetry

Whether one is dealing with spin-orbit coupling, external (static) magnetic fields, or geometrically frustrated systems, one needs to be certain that the final non-collinear solution is at a true variational minimum, rather than a higher-energy saddle point. Such a condition is necessary for properties based on energy derivatives, as well as an initial condition for electronic dynamics, not to mention reaction barrier heights and other properties based on energy differences. The stability of different classes of broken-symmetry wave functions has been studied by Seeger and Pople,[3] and has recently been explored with particular regard to molecular ring test systems.[10] In Chapter 2, we will show that the non-collinear solution for Cr_3 could be as much as 7.5 kcal mol^{-1} lower in energy than the lowest collinear solution (see Fig. 2.5 in Chapter 2).

In the absence of symmetry breaking terms in the Hamiltonian, for non-collinear wave functions there are often several degenerate or nearly degenerate states near the ground state. Thus while it is often unnecessary to test for wave function stability in routine RHF and UHF calculations (simple organic molecules, say), for non-collinear GHF wave functions stability testing is an absolute requirement. In our experience, GHF solutions rarely converge to the minimum on the first try, and often require multiple re-optimizations after stability tests in order to get a ground-state non-collinear solution at its variational minimum. Closely related to this is the suitability of the initial guess for the GHF wave function: because non-collinear solutions often arise in molecules with spatially degenerate ground states (point group D_{3h}, for example), initial guesses with suitable spatial overlap with the ground-state wave function are required, else the solution converges to an irreducible representation of a subgroup of the point group (a lower-symmetry solution). For example, instead of the E' state of D_{3h}, the wave function will converge to either B_2 or A_1 in the reduced symmetry C_{2v} point group. For non-collinear solutions arising from a symmetry breaking term in the Hamiltonian (e.g. spin-orbit or magnetic field), the problem of converging to higher energy saddle points, in

our experience, seems to be less severe.

Use in magnetization dynamics

An interesting recent development in non-collinear electronic structure theory has been in the application of non-collinear methods to electronic dynamics. Because non-collinear wave functions allow for smooth transitions between various spin configurations, they allow for dynamical simulations of molecules under the influence of magnetic fields. Furthermore, non-collinear methods can be modified to include relativistic effects, such as spin-orbit coupling, which mixes spin states on account of the spin-orbit operators. The first extension of real-time electronic dynamics to fully *ab initio* non-collinear solutions was reported in 2014.[11] In this work, non-collinear GHF solutions were allowed to time evolve in the presence of an external magnetic field. Because of the non-collinear nature of the solutions, the spin magnetization was allowed to evolve in time coupled to a magnetic field, and the numerical simulations matched the analytically predicted Larmor frequency for simple test systems, and served as a proof of concept that spin dynamics could be captured with real-time non-collinear methods. Recently, the real-time non-collinear method was used to extract magnetic exchange couplings for several magnetic systems by Peralta and Scuseria.[12]

There have been a few interesting areas of research in non-collinear spin dynamics. The first is the extension of non-collinear *ab initio* spin dynamics to include nuclear couplings through the Ehrenfest method.[1] In this method, the nuclei couple to the non-collinear spin-dependent terms and *vice versa*. Since non-collinear methods allow the spin state of a system to evolve smoothly, the non-collinear Ehrenfest method was applied to bond breaking, where the total system may pass through several spin states during dissociation. A clear example is given by the dissociation of the H_2 molecule, seen in Fig. 1.1. Initially in a ground-state singlet, as the hydrogens separate, the singlet solution passes into the triplet state. Interestingly, the spin states mix and coupling between the spin states is observable in the evolution of the atomic magnetic moments during dissociation. At large distances, each atomic magnetic moment correspond to $m_s = +1/2$ and $m_s = -1/2$, respectively.

However, due to the mean field approach of Ehrenfest dynamics, the mixing of spin states artificially raises the energy at large distances. Finally, *ab initio* real-time non-collinear

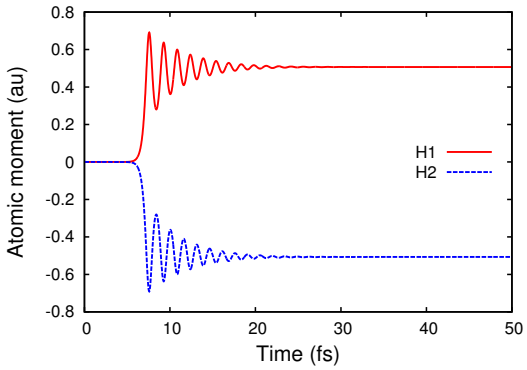

Figure 1.1: Atomic magnetic moments of H_2 during dissociation from equilibrium with non-collinear Ehrenfest method (B3LYP/6-31G). The molecule had an initial vibrational kinetic energy of 7.25 eV. As the hydrogen atoms separate over time, the local spins take on non-zero values, so that by full dissociation around 25 fs each has an atomic magnetic moment of 1/2 μ_B. The oscillatory phenomenon between 8 fs and 20 fs corresponding to an energy of 2.7 eV, corresponding to coherence between the singlet ionic state and the triplet ground state in the avoided crossing region. Dissociation follows along a mean Ehrenfest potential between different spin states. Adapted from Reference 1.

dynamics have been extended to the relativistic regime, where spin-orbit coupling operators force non-collinear solutions. The first demonstration of relativistic non-collinear electronic dynamics was at the four-component level of theory,[13] which was later extended to the exact two-component (X2C) Hamiltonians.[14,15] A detailed discussion of the latter work can be found in Chapter 4. In both these cases, the accurate treatment of spin-orbit coupling requires the use of non-collinear wave functions, and is critical to the accurate treatment of excitation energies for heavy elements. The spin-orbit coupling effectively mixes spin states which, particularly for heavy elements, weakly allows otherwise spin-forbidden processes. This also leads to a qualitatively different electronic absorption spectra with respect to collinear methods, as peaks split based on the strength of the spin-orbit coupling. The dynamical methods have been found to be in excellent agreement with linear-response methods in a

study where employing X2C Hamiltonian[16–19] to model relativistic effects.[20] The real-time non-collinear X2C method has also recently been applied to investigate nonlinear optical properties of heavy elements, where spin-orbit corrections may be important.[14,15]

Conclusion

For magnetic and spin phenomena, non-collinear electronic structure theory is the natural choice on account of spin-symmetry breaking terms in the Hamiltonian (spin-orbit and external magnetic fields). The extension of non-collinear wave functions to dynamical methods, such as real-time time-dependent theory and non-collinear Ehrenfest dynamics in recent years have paved the way to incorporate magnetic and spin phenomena into molecular and electronic dynamics. Properly accounting for external magnetic fields with London orbitals as well as including additional spin-coupling terms, such as the Breit operator, in the Hamiltonian has seen more development over the past few years, but their extension to dynamic and time-dependent properties remains to be seen. Such developments are necessary for studies of non-equilibrium phenomena driven by external and internal magnetic perturbations, such as spin transport, spin crossover, and spin dephasing.[21]

In addition to the need for new developments incorporating additional spin coupling terms and magnetic fields, one future area of development that needs to be addressed is the extension of relativistic non-collinear methods to the treatment of solids and periodic systems. Most of the developments in relativistic non-collinear electronic structure theory have been applied to finite systems like molecules and clusters, yet solid-state applications stand the most to gain from these approaches. This is because small relativistic non-collinear terms in the Hamiltonian, such as spin-orbit coupling, become large in extended periodic systems and can strongly alter the band structures. In particular, periodic systems lacking inversion symmetry experience momentum-dependent spin-orbit effects (Rashba spin-orbit coupling) that are linear in electron momentum. This has led to several advances in non-equilibrium spin dynamics, which allow for electrical control of spin and magnetization, as well as new states of matter (e.g. topological insulators). Clearly, this is a place where extending the

developments in relativistic non-collinear quantum chemistry to periodic systems can shine.

Quantum chemistry has made great strides in the development of non-collinear electronic structure theory, often guided and inspired by developments in solid-state physics. Extending the techniques of non-collinear quantum chemistry to periodic boundary conditions should allow condensed-matter physicists to reap the fruits of these developments, as non-collinear electronic structure methods come full circle.

Chapter 2

STABILITY OF THE COMPLEX GENERALIZED HARTREE-FOCK EQUATIONS

For molecules with complex and competing magnetic interactions, it is often the case that the lowest-energy Hartree-Fock solution may only be obtained by removing the spin and time-reversal symmetry constraints of the exact non-relativistic Hamiltonian. To do so results in the complex generalized Hartree-Fock (GHF) method. However, with the loss of variational constraints comes the greater possibility of converging to higher energy minima. Here we report the implementation of stability test of the complex GHF equations, along with an orbital update scheme should an instability be found. We apply the methodology to finding the local minima of several spin-frustrated hydrogen rings, as well as the non-collinear molecular magnet Cr_3, illustrating the utility of the broken-symmetry GHF method and some of its lesser-known nuances. The work in this chapter was adapted with permission from Joshua J. Goings, Feizhi Ding, Michael J. Frisch, and Xiaosong Li. Stability of the complex generalized Hartree-Fock equations. *J. Chem. Phys.*, 142(15):154109, 2015.

Introduction

It has been known for a while that requiring approximate, variational Hamiltonians to have the same symmetries as the exact Hamiltonian adds additional constraints to the variational problem.[3–6,22] Such constraints can only raise the energy, contrary to the goal of the variational method. As first pointed out by Löwdin,[2] the practicing quantum chemist is faced with a dilemma: should one seek an approximate solution that is a true variational minimum, or should one seek solutions that retain the correct symmetry of the exact solution?

For approximate Hartree-Fock solutions, one cannot have both simultaneously. Insisting that we abandon symmetry constraints, we recover the generalized Hartree-Fock equations (GHF). GHF is a non-collinear method, meaning that spin-orbitals are allowed to be a superposition of spin-up and spin-down states. This allows each spin quantization axis to rotate freely, which is necessary for systems with complex and competing magnetic interactions, such as geometrically frustrated systems. GHF and non-collinear approaches will be necessary for their description.[9,23–29] For example, taking the advantage of the flexibility in the spin degrees of freedom, we have recently applied the time-dependent formalism of GHF to *ab-initio* non-relativistic spin dynamics.[11]

The complex GHF method is part of a family of broken-symmetry methods in the independent-particle model. The broken-symmetry methods were first mapped out by Fukutome,[4] and later clarified and renamed by Stuber and Paldus.[22] The real-valued unrestricted Hartree-Fock (UHF) method, for example, is the name of the Hartree-Fock method that breaks $\hat{S}^2$ symmetry but is invariant to complex conjugation and rotations by $\hat{S}_z$. As is well known, UHF solutions are not eigenfunctions of $\hat{S}^2$, and this is to be expected from symmetry analysis. A thorough description of broken symmetries in the independent-particle model is given by Stuber and Paldus.[22] Invariance to symmetry operations provides good quantum numbers. Thus a true GHF solution cannot be classified by any spin quantum numbers. As will be shown later, broken symmetries also imply degeneracies which provides a route to restoration of symmetry (and good spin quantum numbers).[8,30] One such route is to take a linear superposition of broken-symmetry solutions. Recently, the projected Hartree-Fock method[31,32] has been proposed and tested as a route to restore symmetry in broken-symmetry solutions. In any case, it is crucial to note that such restoration may only be done at the multireference level. We do not concern ourselves with multireference solutions any longer, and explore single-determinant solutions from here on out.

An even more concerning issue arises even at the single-determinantal level. Removing symmetry constraints from the Hartree-Fock model provides the additional degrees of freedom necessary to converge to a true broken-symmetry minimum (if one exists). However, with

the additional degrees of freedom comes the increased chance of converging not to the true energetic minima, but rather a higher-order energy saddle point. GHF is notorious for converging to higher-energy saddle points. By changing the initial GHF guess, one may converge to all sorts of higher order solutions. Thus when using GHF, it is critical to ensure that the solution obtained is a true local minimum. Furthermore, if the solution is not a true local minimum, methods must be devised to reoptimize GHF so that it does converge on the true energetic minimum. Here we report the derivation and implementation of the stability conditions and orbital rotations necessary to ensure the true GHF minimum is obtained. Having done this, we explore the utility of GHF when it is applied to surprisingly tricky spin-frustrated ring systems.

Theory

Much work has gone into deriving the general stability conditions for the Hartree-Fock equations, and we briefly derive these conditions following the work of Cízek and Paldus.[33] In the present work we adopt the notation that indices i, j, k, l refer to occupied orbitals, a, b, c, d refer to virtual orbitals, and p, q, r, s refer to any orbital. We also adopt Einstein summation, where the summation over common indices is implied. We begin with the Thouless representation of a single determinant. Thouless showed that any single Slater determinant can be transformed into another non-orthogonal single determinant via the transformation[34]

$$|\tilde{\phi}\rangle = e^{\hat{T}_1}|0\rangle \tag{2.1}$$

where $\hat{T}_1$ is a single-particle excitation operator

$$\hat{T}_1 = \sum_{ia} t_i^a \{a_a^\dagger a_i\} \tag{2.2}$$

In order to ensure that the Thouless transformation is enacted by a unitary transformation, we insist on the condition that $\hat{T}_1$ is skew-Hermitian, i.e.

$$\hat{T}_1 = -\hat{T}_1^\dagger \tag{2.3}$$

which implies that

$$t_i^a = -t_a^{i*} \tag{2.4}$$

Consider the connected energy functional

$$E = \langle \tilde{\phi} | \hat{H}_N | \tilde{\phi} \rangle_c = \langle 0 | e^{\hat{T}_1^\dagger} \hat{H}_N e^{\hat{T}_1} | 0 \rangle_c \tag{2.5}$$

where

$$\hat{H}_N = \hat{H} - \langle 0 | \hat{H} | 0 \rangle = \hat{F}_N + \hat{V}_N = f_{pq} \{ a_p^\dagger a_q \} + \frac{1}{4} \langle pq || rs \rangle \{ a_p^\dagger a_q^\dagger a_s a_r \} \tag{2.6}$$

and $\hat{H}$ is our Hamiltonian. $\hat{F}_N$ and $\hat{V}_N$ are the one- and two-body operators; the elements f_{pq} are the elements of the Fock matrix and $\langle pq || rs \rangle$ are the antisymmetrized two-electron integrals. For this parameterized functional, expanding through second order in $\hat{T}_1$ gives

$$E = \langle 0 | \hat{H}_N + \hat{T}_1^\dagger \hat{H}_N + \hat{H}_N \hat{T}_1 + \hat{T}_1^\dagger \hat{H}_N \hat{T}_1 + \frac{1}{2} \hat{T}_1^\dagger \hat{T}_1^\dagger \hat{H}_N + \frac{1}{2} \hat{H}_N \hat{T}_1 \hat{T}_1 | 0 \rangle_c \tag{2.7}$$

Taking the first variation of E with respect to the Thouless parameters $q_i^a = (t_i^a, t_i^{a*})$ about $\hat{T}_1 = \hat{T}_1^\dagger = 0$, gives

$$\frac{\partial E}{\partial q_i^a} = \begin{pmatrix} \langle \phi_i^a | \hat{H}_N | 0 \rangle_c \\ \langle 0 | \hat{H}_N | \phi_i^a \rangle_c \end{pmatrix} = \begin{pmatrix} f_{ai} \\ f_{ia} \end{pmatrix} \tag{2.8}$$

which must equal zero if the energy functional is minimized. Thus $f_{ia} = 0$ which are the off-diagonal elements of the Fock matrix, which is Brillouin's theorem. Taking the second

variation of E with respect to the Thouless parameters yields

$$\frac{\partial^2 E}{\partial q_i^a \partial q_j^b} = \begin{pmatrix} \langle \phi_i^a | \hat{H}_N | \phi_j^b \rangle_c & \langle \phi_{ij}^{ab} | \hat{H}_N | 0 \rangle_c \\ \langle 0 | \hat{H}_N | \phi_{ij}^{ab} \rangle_c & \langle \phi_j^b | \hat{H}_N | \phi_i^a \rangle_c \end{pmatrix} \tag{2.9}$$

For the Hartree-Fock equations to be stable, the second variation must be positive semidefinite, i.e. $\delta^{(2)} E \geq 0$. Putting the second variation in matrix form, we obtain the Hessian

$$\begin{pmatrix} \mathbf{A} & \mathbf{B} \\ \mathbf{B}^* & \mathbf{A}^* \end{pmatrix} \tag{2.10}$$

where

$$A_{ia,jb} = (\epsilon_a - \epsilon_i)\delta_{ia,jb} + \langle aj || ib \rangle, \qquad B_{ia,jb} = \langle ab || ij \rangle \tag{2.11}$$

For the complex GHF equations, the orbital energies will be real as they are the eigenvalues of a Hermitian matrix. The antisymmetrized two-electron integrals, however, will be complex. Thus in the complex GHF case, $\mathbf{A} \neq \mathbf{A}^*$ and $\mathbf{B} \neq \mathbf{B}^*$. At any stationary solution to the Hartree-Fock equations, the above Hessian may be constructed and diagonalized. Strictly negative eigenvalues indicate an instability, and the corresponding eigenvector indicates the direction in which the Hartree-Fock energy will decrease. This can be accomplished by taking the eigenvector corresponding to the lowest eigenvalue (steepest descent) and constructing a complex-valued $(2N \times 2N)$ mixing matrix $\mathbf{K}$, where N is the number of basis functions.[3]

$$\mathbf{K} = \begin{pmatrix} \mathbf{0} & -\mathbf{J}^\dagger \\ \mathbf{J} & \mathbf{0} \end{pmatrix} \tag{2.12}$$

Where $\mathbf{J}$ is the $(O \times V)$ eigenvector corresponding to the lowest eigenvalue. This mixing matrix is exponentiated to give the unitary rotation matrix that transforms the old set of

MO coefficients $\mathbf{C}$ to a new set of rotated MO coefficients $\mathbf{C}'$

$$\mathbf{C}' = \mathbf{C}e^{-s\mathbf{K}} \tag{2.13}$$

where s is some small step in the direction $\mathbf{K}$. The new rotated MO coefficients may be fed back into the SCF procedure and the Hartree-Fock solutions re-optimized. With a suitable step-size, the Hartree-Fock equations will converge to a lower-energy solution, and the stability test may be performed again.

Discussion

Among the first row elements, GHF solutions are rare. That is, GHF solutions are identical to the RHF (or UHF) solutions in most cases. However, molecular systems involving geometric frustration are prime targets for a GHF analysis because their frustrated spins must break $\hat{S}_z$ symmetry in order to minimize Pauli repulsion. Geometrically frustrated systems have long been a target for GHF and non-collinear DFT methods.[9,23–29] Thus, to explore the applicability of our GHF stability tests, we examined a series of neutral hydrogen rings, ranging from 3 to 15 hydrogens. Each hydrogen was spaced 1 Å around a circle. The advantage of studying such a system is threefold: first, the system is simple enough that we can be guided by chemical intuition, second, at such a spacing the hydrogen rings act similar to 1D hydrogen chains that prefer an antiferromagnetic alignment, and third, each odd-membered ring will be geometrically frustrated. There are few theoretical or experimental studies of hydrogen rings,[35,36] but this appears to be the first to study the geometrically frustrated neutral, odd-numbered hydrogen rings. This geometric frustration means that a GHF solution must exist which minimizes the repulsion from the frustrated spin alignment. It bears mentioning that although the system appears to be artificial, equilateral H_3^+ is among one of the most common ions in interstellar gases,[37,38] and H_3 has been observed experimentally.[39] Furthermore, recent combined theoretical/experimental reports have demonstrated the evidence of sigma-aromatic H_5^- when complexed with ZnPt.[40] The complex GHF code, stability tests, and orbital update

codes were implemented in the development version of Gaussian.[41] All tests were performed using a cc-pVDZ basis,[42] which is the minimum necessary to describe the polarization of hydrogenic s-functions.

Following Blaizot and Ripka,[30] we define a broken-symmetry solution as a solution to the approximate Hamiltonian that cannot be classified according to an irreducible representation of the symmetry group of the exact non-relativistic Hamiltonian. In other words, the approximate solution does not carry the quantum numbers of the exact Hamiltonian. For example, while spin projection m_s is a good quantum number for the exact Hamiltonian, it is not necessarily a good quantum number for the GHF solutions that approximate it.

Qualitatively, the differences between the UHF and GHF solutions are given in Figures 2.1 and 2.2, respectively. The magnetization is defined according to the Hirshfeld partitioning given in references 11, 43. The spin density in the non-collinear approach is a mapping of the 2-norm of the spin magnetization vector[44] onto the total density. This ensures that the spin density is always positive and always real. It is also worth noting that GHF will provide complex density matrices, however, the density matrix is Hermitian and will correspond to a real observable, thus the total density yields real-valued observables. The charge density is a mapping of the electrostatic potential to the total density. A quantitative energetic comparison is given in Table 2.1. For even numbered rings, GHF and UHF results are identical. Both converge to the same antiferromagnetic spin distribution, aside from the six- and ten-membered rings. The six- and ten-membered rings do not have antiferromagnetic ordering because they are sigma aromatic, following Hückel's $4j + 2$ rule. This is further evidenced by the large energetic stabilization of these rings relative to the other rings. The fourteen membered ring break this pattern however, and shows the beginning of slight antiferromagnetic ordering. In this case, the local ordering of the molecule is moving away from cyclical and towards linear, thus breaking Hückel aromaticity in the large-n case. Although RHF results are not shown, the energetic ordering for even membered rings goes RHF $>$ UHF $=$ GHF, aside from the aromatic cases. This is understandable, as RHF cannot treat antiferromagnetic ordering. For odd membered rings, UHF and GHF provide

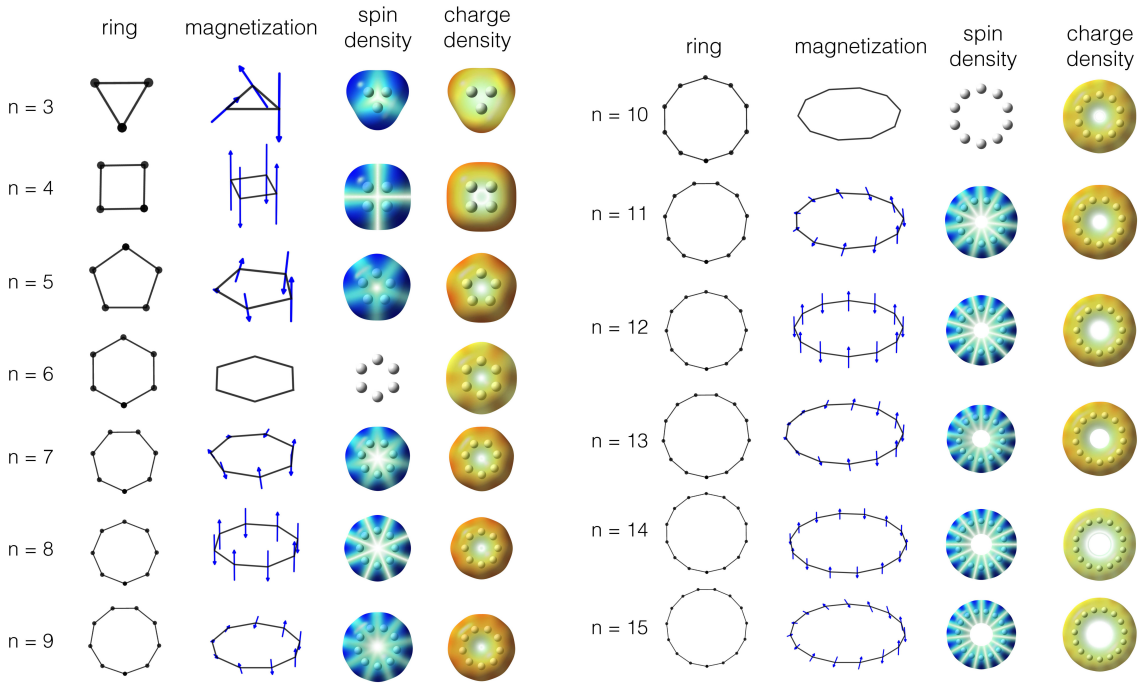

Figure 2.1: Local GHF energetic minima of hydrogen rings sizes 3 to 15. Odd-membered rings break the axial symmetry of the axis normal to the molecular plane; this is unique to GHF solutions and minimizes Pauli repulsion. The spin density is the 2-norm of the magnetization vector at each point in space, with blue being the greatest in magnitude. Charge density is represented as the electrostatic potential mapped to the total density, with red color showing a greater electronic population.

very different solutions. This is the result of geometrically frustration. GHF solutions are always lower energy than the UHF solutions, which is to be expected because it allows for broken-symmetry solutions. The stabilization over UHF ranges from 0.9 kcal mol^{-1} for $n = 3$, to nearly 10.0 kcal mol^{-1} for $n = 15$. UHF requires collinear ordering of magnetization, as its solutions are constrained to be eigenfunctions of $\hat{S}_z$, and this is clearly seen in the ordering of the magnetization vectors in Figure 2.2. GHF, on the other hand, has its lowest energy solutions with magnetization vectors arranged in a non-collinear manner. This Möbius-like periodicity of magnetization ordering in GHF results in a totally symmetric distribution of

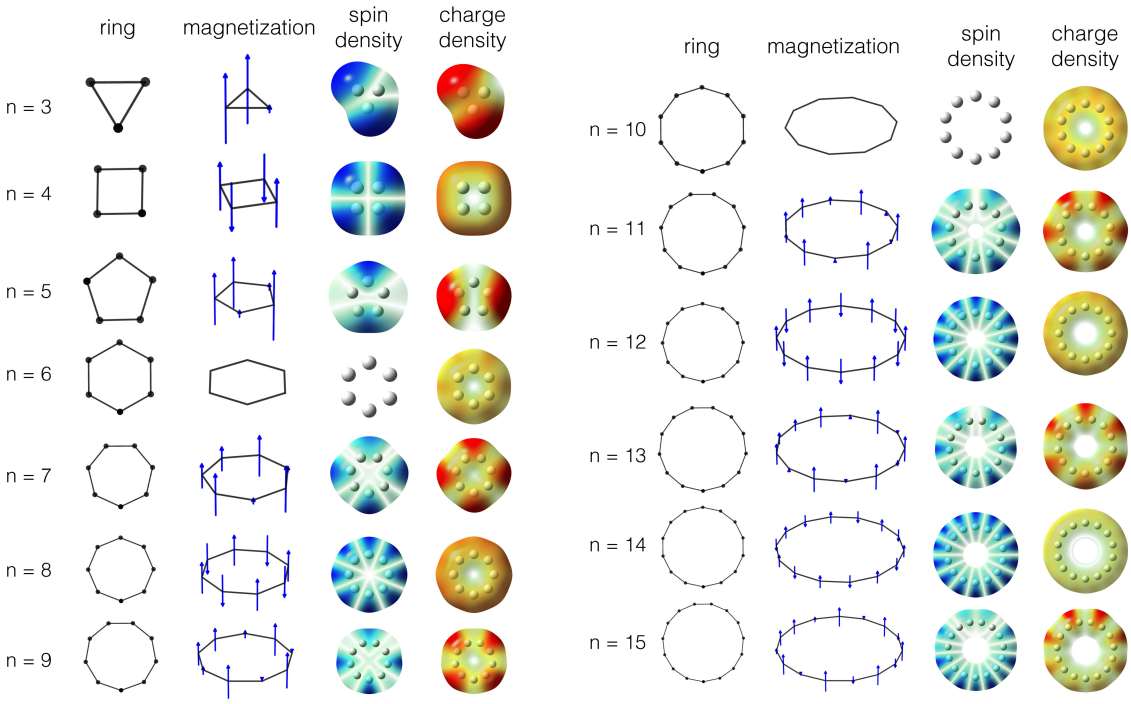

Figure 2.2: Local UHF energetic minima of hydrogen rings sizes 3 to 15. Unlike GHF, the UHF cannot break $\hat{S}_z$ symmetry (hence collinear magnetizations), resulting in asymmetric spin distribution through the odd-numbered rings. This raises the energy compared to their GHF counterparts. The spin density is the 2-norm of the magnetization vector at each point in space, with blue being the greatest in magnitude. Charge density is represented as the electrostatic potential mapped to the total density, with red color showing a greater electronic population.

spin density throughout the structure. The distribution of magnetic coupling is maximized in the GHF solutions. On the other hand, UHF solutions must order spins in a lower-symmetry distribution which is especially clear in the $n = 3$ and $n = 5$ cases. The charge density further confirms this distribution, with a lower-symmetry charge distribution as the result of electrons pairing locally instead of delocalizing throughout the ring as in the GHF solutions. While neither the UHF nor the GHF solution is an eigenfunction of $\hat{S}^2$, and GHF is not even an eigenfunction of $\hat{S}_z$, it is interesting to look at the expectation values of these spin operators, given in Figure 2.3. The GHF solution has a net zero expected value of $\hat{S}_z$ for all ring sizes

Table 2.1: Comparison of energetic minima between GHF and UHF for various H_n rings. Energies are given in kcal mol^{-1} from an infinitely separated n-hydrogen reference. The fourth column gives the difference in energy between GHF and UHF. Energies decrease monotonically except for at $n = 6$ and $n = 10$, corresponding to aromatic stabilization. The far right column gives the number of zeros in the GHF Hessian. All other eigenvalues are positive. For strictly unique GHF solutions, we see three zeros, corresponding to broken-symmetry modes along the x, y, and z spin rotations. When GHF solutions lie on the UHF manifold we see two zeros, corresponding to broken-symmetry modes along the x and y spin rotations. When GHF solutions lie on the RHF manifold, as in the $n = 6$ and $n = 10$ cases, we see no zeros, corresponding to a fully spin-symmetric solution.

n	ΔGHF	ΔUHF	Δ(GHF-UHF)	GHF Zeros
3	-6.21	-5.30	-0.91	3
4	-15.04	-15.04	0.00	2
5	-59.53	-56.20	-3.33	3
6	-159.35	-159.35	0.00	0
7	-122.34	-118.88	-3.46	3
8	-153.69	-153.69	0.00	2
9	-187.20	-181.79	-5.41	3
10	-251.48	-251.48	0.00	0
11	-236.73	-230.50	-6.23	3
12	-270.94	-270.94	0.00	2
13	-293.98	-286.08	-7.90	3
14	-340.08	-340.08	0.00	2
15	-342.85	-332.63	-10.22	3

considered, which is characteristic of these broken-symmetry solutions. The individual atomic spin magnetizations cancel out. In UHF, such global cancellation of spin magnetization cannot occur in odd-membered rings on account of geometric frustration. The expected value of $\hat{S}^2$ increases for both GHF and UHF as ring size increases, showing increasing spin contamination in these systems.

While the absence of negative Hessian eigenvalues assures us that the GHF solutions are indeed at a local minimum, we may wonder if the solutions obtained are unique. It turns out that broken-symmetry solutions are not unique. In fact, for any broken-symmetry we may find an infinite number of degenerate solutions. This is not difficult to show. Consider a

symmetry depending on some real parameter θ of the Hamiltonian that satisfies the following:

$$\hat{U}(\theta)\hat{H}\hat{U}(\theta)^{\dagger} = \hat{H} \tag{2.14}$$

Now, consider some GHF solutions that break the above symmetry and are related by the transformation

$$|\phi\theta\rangle = \hat{U}(\theta)|\phi\rangle; \qquad |\phi\theta\rangle \neq |\phi\rangle \tag{2.15}$$

It then follows that

$$\langle\phi\theta|\hat{H}|\phi\theta\rangle = \langle\phi|\hat{H}|\phi\rangle \tag{2.16}$$

Which is to say that there degenerate GHF solutions which depend on θ, which may be discrete or continuous. Continuously broken symmetries lead to zeros in the Hessian, though the converse is not necessarily true,[30] and many of the implications of broken symmetries in Hartree-Fock have been studied recently.[8] Broken continuous symmetry (which is a manifestation of Goldstone's theorem for finite systems), however, is the origin of the zeros in the GHF Hessian for the hydrogen rings studied. GHF solutions that are uniquely GHF (i.e. impossible to obtain *via* UHF, etc.) have three zeros in the Hessian. This corresponds to broken spin symmetry modes along the x,y, and z axes. For GHF solutions that have unique solutions in the UHF manifold, there are two zeros observed in the Hessian, and these correspond to broken spin symmetry modes along the x and y axes (meaning $\hat{S}^2$ is not associated with a good quantum number, but $\hat{S}_z$ is). For GHF solutions that lie in the RHF manifold, as is the case for $n = 6$ and $n = 10$, there are no zeros; that is, the solutions are invariant to all spin symmetry operations.

Broken-symmetry modes can be thought of as collective excitations without a restoring force, and they lead to distinct, degenerate solutions. We can show this empirically by rotating the GHF molecular orbitals in the direction of the zero eigenvalues using our stability updating scheme. Following these eigenmodes will lead us to energetically degenerate and (possibly) distinct solutions to the GHF equations. Following such an approach, we have

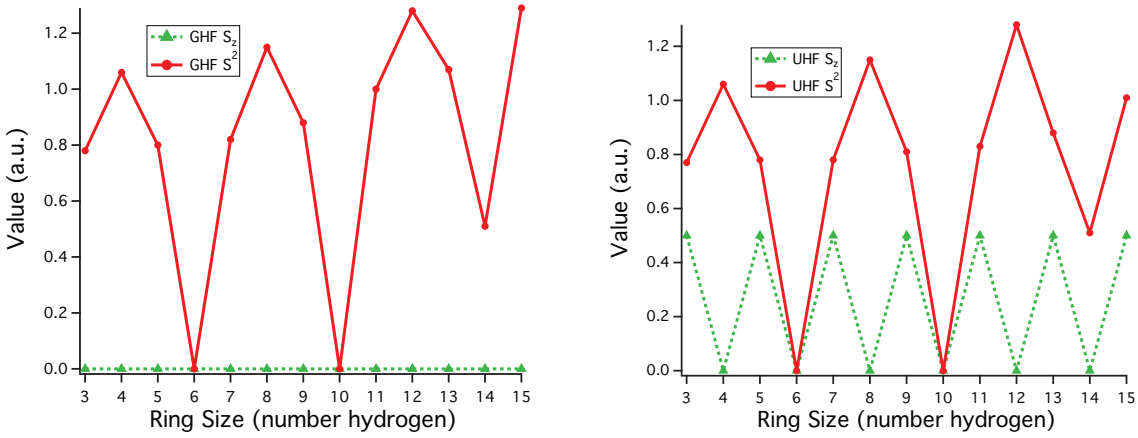

Figure 2.3: Expected values of $\hat{S}_z$ and $\hat{S}^2$ operators on GHF (left) and UHF (right) solutions according to ring size. For $n = 6$ and $n = 10$, the solutions converge to a solution on the RHF manifold. These solutions are aromatic, and have a diamagnetic ring current. The anti-aromatic solutions at $n = 4j$ (where j is an integer) show the greatest expected value $\hat{S}^2$, consistent with a paramagnetic ring current. For odd-membered rings, GHF, unlike UHF, has a zero expected value of $\hat{S}_z$, the result of net cancellation of individual spin magnetic moments which is only possible with non-collinear methods.

found several distinct but degenerate solutions for the H_3 and H_4 rings. These are illustrated in Figure 2.4. The distinct nature of each solutions is most easily seen in the orientation of the magnetization vectors on each atom. Fixing the laboratory reference frame to the top atom in each figure, we see several energetically equivalent magnetization orientations. For H_3, the atomic magnetizations may point in different directions, some in, some out, some even out of the plane defined by the molecule — all molecular expectation values do not change, but the densities do take on distinct solutions. For H_4 we could only find two degenerate solutions (again, assuming we fix the laboratory reference frame). They simply alternate spins pointing up and down in equivalent, but distinctly different ways.

This point is important for thinking about the broken-symmetry solutions. After all, we know that for a true singlet the net magnetic moment on each atom must go to zero. The true solution must lie in a superposition between these two solutions, which is a multireference

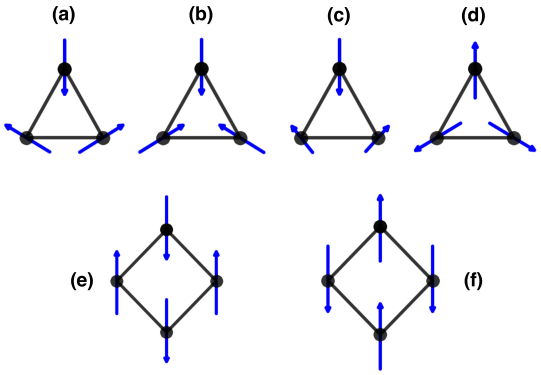

Figure 2.4: GHF magnetizations of several degenerate microstates for H_3 (a–d) and H_4 (e,f). The uppermost magnetization vector of each microstate is arbitrarily aligned to the "laboratory z-axis". For H_3, several microstates were found that break the collinearity characteristic to $\hat{S}_z$ symmetry invariance. For H_3, (a,b,d) lie in the plane of the page, however, (c) has magnetization vectors that go out of plane. For H_4, GHF and UHF give the same solution and the microstates are invariant to $\hat{S}_z$ symmetry. For this reason only two collinear microstates can be found.

problem. The atomic spin magnetic moments are not static, but dynamic. They fluctuate in a coherent state whose atomic spin moments cancel out to zero. This problem with the GHF solutions was recently identified by Scuseria, *et al.*[8,32] and remedied with the projected Hartree-Fock approach. Again, we must mention that this cannot be done at a single determinental level.

Despite this, complex GHF solutions provide a powerful method to explore the nature of geometric frustration in molecules. Many concepts in magnetic ordering originate in solid-state physics. Just as UHF allows one to take the concepts of (anti)ferromagnetism to the single-molecule domain, so does GHF take the solid-state concept of geometric frustration and apply it to the single-molecule domain. This is important for explorations into local and microscopic origins of exotic magnetic behavior.

As a final demonstration of the utility of the GHF stability equations and update scheme, we apply our methods to the neutral chromium trimer in an equilateral triangle

geometry. While this solution is known to have a non-collinear ground state (see, for example, references[9,23]), reports using unrestricted DFT predict that neutral Cr_3 has an extremely high spin ^{17}E ground state.[45] We can see how the GHF stability and update scheme connects these two solutions. The solution schematic is given in Figure 2.5. Following previous work by Sharma *et al.*[23] and Bulik *et al.*,[9] we create a D_{3h} Cr_3 trimer at a bond length of 2.89Å, close to the high spin ^{17}E ground-state UKS of Papas and Schaefer[45] which had an equilibrium bond length of 2.92Å. Using a LANL2DZ[46] basis we find that UHF theory predicts a high spin state as well, though with 18 unpaired electrons instead of 16. This spin state is shown on the left of Figure 2.5. Given this guess, GHF will converge to the collinear UHF solution. However, this GHF solution is a higher-order energy saddle point, as the subsequent GHF stability test shows four negative roots, and using the update scheme we generate a rotated spin guess a mere 0.5 kcal mol^{-1} ($\langle S^2 \rangle = 57.9$) lower in energy. This rotation breaks the collinearity of the UHF solution, and is enough to perturb the solution to converge to the non-collinear GHF state, which is 7 kcal mol^{-1} lower in energy than the UHF reference. Further tests show that this solution is a GHF local minimum. This same procedure will be important when studying induced non-collinear magnetism by surface-deposited transition metal nanostructures. Lounis,[47] has indicated that Cr and Mn are excellent candidates for non-collinear magnetic structures, but Fe and Ni will not. Clearly, there are many factors to consider in further theoretical study of such nanostructures, but GHF may play an important role in future work as we see the need to break $\hat{S}_z$ symmetry for energetically superior results.

Conclusions

Here we have implemented a complex generalized Hartree-Fock stability test and orbital update scheme in order to seek out the lowest local energetic minima possible within the Hartree-Fock model. We have applied this methodology to simple geometrically frustrated systems, where spin magnetic moments cannot favorably align within the collinear framework. The non-collinearity of the GHF solutions relaxes the symmetry constraints of the exact

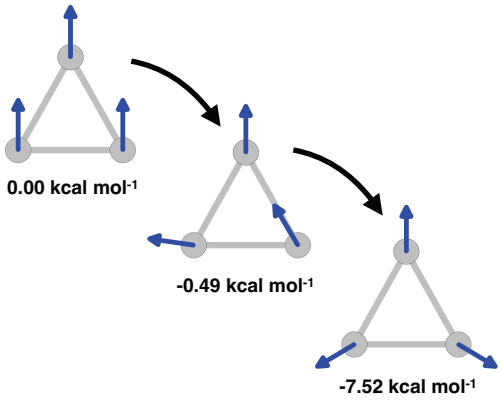

Figure 2.5: Connection between higher order GHF solutions in the neutral chromium trimer (LANL2DZ, D_{3h}, 2.89Å). There exists a high spin GHF solution (left), which also lies in the UHF manifold, that preserves collinearity. However, GHF stability tests indicate a lower solution exists, and the update scheme breaks the collinearity, slightly lowering the energy in the process (center). Subsequent iterations in the SCF bring this non-collinear rotated guess to the true GHF non-collinear minima (right).

Hamiltonian, allowing for spin magnetizations to align most favorably in three dimensions. However, despite the energetic advantages of relaxing symmetry constraints, we do so at the loss of good spin quantum numbers. The loss of good spin quantum numbers can be restored at the multideterminental level, however, it is important to keep in mind that in the true relativistic Dirac formalism, spin is no longer a good quantum number anyway. GHF is inherently a two-component spinor method, and in fact may be thought of as a non-relativistic approximation to two-component Dirac-Fock methods. GHF is critical to the proper description of non-collinear magnetism in transition metal structures, illustrated here for the case of Cr_3. GHF will be useful for future work involving complex and exotic magnetic systems.

Chapter 3

APPROXIMATE SINGLY EXCITED STATES FROM A TWO-COMPONENT HARTREE-FOCK REFERENCE

For many molecules, relaxing the spin symmetry constraint on the wave function results in the lowest-energy mean-field solution. The two-component Hartree-Fock (2cHF) method relaxes all spin symmetry constraints, and the wave function is no longer an eigenfunction of total spin, spin projection, or time-reversal symmetry. For ground-state energies, 2cHF is a superior mean-field method for describing spin-frustrated molecules. For excited states, the utility of 2cHF is uncertain. Here we implement the 2cHF extensions of two single-reference excited-state methods, the two-component configuration interaction singles (2cCIS) and time-dependent Hartree-Fock (TD2cHF). We compare the results to the analogous methods based on the unrestricted Hartree-Fock approximation, as well as the full configuration interaction for three small molecules with distinct 2cHF solutions, and discuss the nature of the 2cHF excited-state solutions. The work in this chapter was adapted with permission from Joshua J. Goings, Feizhi Ding, Ernest R. Davidson, and Xiaosong Li. Approximate singly excited states from a two-component Hartree-Fock reference. *J. Chem. Phys.*, 143(14):144106, 2015. Copyright 2015 American Institute of Physics.

Introduction

Spin is a good quantum number for many molecules, especially those containing light elements. As a result, standard self-consistent fields are constrained to be eigenfunctions of the spin operators. Often the spin symmetry constraint on mean-field solutions raises the energy. A lower variational energy may be obtained by abandoning the spin symmetry constraints on the mean-field wave function. For Hartree-Fock wave functions, relaxing the total spin (S^2) and

spin projection ($\hat{S}_z$) symmetry constraints result in the two-component Hartree-Fock (2cHF) method. Furthermore, relaxing the time-reversal symmetry constraint yields complex 2cHF solutions.[4] 2cHF is equal to the generalized Hartree-Fock method (GHF).[3–5,22,48] We will use the term "two-component Hartree-Fock", but readers should be aware that the field-free non-relativistic 2cHF is identical to GHF.

In practice, 2cHF means we allow the generalized molecular orbitals to consist of a (complex) linear combination of spin-up and spin-down components. Unlike UHF, 2cHF will no longer be an eigenfunction of $\hat{S}_z$. If one wishes to have a solution with good spin quantum numbers, it is possible to restore these symmetries through projected Hartree-Fock theory (PHF). The projection can be performed before or after the Hartree-Fock variational procedure. A "projection-after-variation" approach was explored by Löwdin in 1955.[49] Recently, a "variation-after-projection" approach was explored.[32] In either case, the PHF solution is no longer a single Slater determinant.

The advantage of using 2cHF is that it allows the lowest-energy mean-field solution to be obtained. One class of molecules where 2cHF outperforms UHF and RHF methods is found in spin frustrated systems. Spin frustrated systems are systems where multiple magnetic interactions cannot be simultaneously optimized.[47] For spin frustrated systems, the 2cHF solution will always be of lower energy than the more restrictive UHF solution.[4,9,22–26,28,29,48,50]

Despite the success of 2cHF for computing ground-state energies, little is known about the nature and quality of excited-state methods based on a 2cHF reference. Here we report an extension of the complex 2cHF equations to two approximate excited-state methods, the two-component configuration interaction singles (2cCIS) and two-component linear-response time-dependent Hartree-Fock (LR-TD2cHF). Though we are not the first to implement such methods — Yamaki, *et al.* has reported a real-valued 2cCIS and LR-TD2cHF,[48] and Kühn and Weigend[51] have implemented a two-component TDDFT — fundamental understanding of the 2cHF ground and excited states remains elusive. In order to better understand the nature of two-component solutions, we apply the formalism to three small systems with fundamentally two-component Hartree-Fock solutions, where exact solutions are known and

the system size permits a detailed orbital analysis.

Theory

While the expressions for LR-TDHF/RPA are well known,[52–54] we briefly outline the method, and highlight the changes in the extension of TDHF to a 2cHF reference. In the present work we adopt the notation that indices i, j, k, l refer to occupied orbitals and a, b, c, d refer to virtual orbitals. Indices p, q, r, s refer to any orbital.

The master equation in LR-TDHF method is given by

$$\begin{pmatrix} \mathbf{A} & \mathbf{B} \\ \mathbf{B}^* & \mathbf{A}^* \end{pmatrix} \begin{pmatrix} \mathbf{X} \\ \mathbf{Y} \end{pmatrix} = \omega \begin{pmatrix} \mathbf{I} & \mathbf{0} \\ \mathbf{0} & -\mathbf{I} \end{pmatrix} \begin{pmatrix} \mathbf{X} \\ \mathbf{Y} \end{pmatrix} \tag{3.1}$$

where

$$A_{ia,jb} = (\epsilon_a - \epsilon_i)\delta_{ia,jb} + \langle aj||ib\rangle, \qquad B_{ia,jb} = \langle ab||ij\rangle \tag{3.2}$$

Each block matrix is of the dimension of number occupied orbitals times the number of virtual orbitals, and ϵ_n refers to the n-th orbital energy. $\langle pq||rs\rangle$ are the antisymmetrized two-electron integrals. ω is the excitation energy out of the reference, and its transition is defined by the excitation and de-excitation components of the eigenvector, $\mathbf{X}$ and $\mathbf{Y}$, respectively.

2cHF is a more general formulation of the Hartree-Fock method, and other methods such as UHF and RHF can be thought of as 2cHF subject to certain symmetry constraints. For example, whereas in UHF each molecular orbital is of pure spin-up (α) or spin-down (β), 2cHF molecular orbitals are allowed to be a mixture of both spin-up and spin down such that

$$\phi_i(\mathbf{r}, \omega) = \phi_i^{\alpha}(\mathbf{r})\alpha(\omega) + \phi_i^{\beta}(\mathbf{r})\beta(\omega) \tag{3.3}$$

so the 2cHF molecular orbitals do not necessarily have pure spin-up or spin-down character (and are not eigenfunctions of $\hat{S}_z$). This forbids us from making any spin-blocked restrictions

on the LR-TD-2cHF equations which simplify their UHF and RHF counterparts. Furthermore, in the 2cHF equations, the orbitals are allowed to become complex. This means that for the LR-TD-2cHF matrix, $\mathbf{A} \neq \mathbf{A}^*$ and $\mathbf{B} \neq \mathbf{B}^*$. As a result, dimension-reducing techniques that can be applied to UHF and RHF cannot be directly used in the 2cHF case. Thus we must solve for the eigenvalues and eigenvectors of the non-Hermitian complex matrix in Eq. (3.1). We may choose to neglect the $\mathbf{B}$ matrices, which gives us the two-component configuration interaction singles (2cCIS) method, alternatively known as the two-component Tamm-Dancoff approximation (2cTDA).

Mathematically, we are not guaranteed to have real eigenvalues by solving Eq. (3.1) for a 2cHF reference. Yet as the eigenvalues carry the physical meaning of excitation energies, they will be real. The only time the eigenvalues may take imaginary values is if the underlying reference is not a local energetic minimum. In this case, a lower-energy solution to the 2cHF equations exists. However, the existence of real eigenvalues does not ensure that the 2cHF reference is at a local minimum.[8]

As in the symmetry-restricted Hartree-Fock methods, we may calculate oscillator strengths in addition to excitation energies. This is given by the dimensionless expression

$$f_n = \frac{2}{3}|\langle 0|\boldsymbol{r}|n\rangle|^2 \omega_n \tag{3.4}$$

which is the oscillator strength for transition from the ground state $|0\rangle$ to the n-th excited state $|n\rangle$. ω_n and $\boldsymbol{r}$, the excitation energy and total electronic position operator, are expressed in atomic units. In the above expression the transition moment (here given in the length gauge) is given by[52,53,55]

$$\langle 0|\boldsymbol{r}|n\rangle = \sum_{r=x,y,z} \sum_{i,a} [r^*_{ai} X_{ia} + r^*_{ia} Y_{ia}] \tag{3.5}$$

where r_{pq} are the electronic position integrals and X_{ia} and Y_{ia} are the elements of the TDHF transition eigenvector. The sum is taken over all electronic position integrals x, y, z. The

above expression is evaluated for the TD-2cHF equations using the normalization

$$|\mathbf{X}|^2 - |\mathbf{Y}|^2 = 1 \tag{3.6}$$

for the excitation energies.

Discussion

The two-component extension of CIS and TDHF (2cCIS and TD-2cHF) were implemented in the development version of Gaussian.[41] All solutions obtained were stability tested in their respective HF symmetry manifolds to ensure the lowest-energy reference was used for the excitation spectra.[3,10] The 2cHF excited-state methods were tested against closed- and open-shell structures with known RHF or UHF ground states, and the two-component excited-state methods reproduce the results from their symmetry restricted variants. However, when a system has a distinct 2cHF solution (one that does not lie on the RHF or UHF manifold), the computed absorption spectrum is different. To understand the nature of the 2c excited states, full configuration interaction (FCI) calculations were performed on the same systems using the FCI implementation in PSI4.[56,57]

Real 2cHF: BH Molecule

A simple system with a real 2cHF is the BH molecule with a 4-31G basis. The 2cHF solution is lower in energy than the UHF solution by 0.02 eV. Löwdin and Mayer[5] originally studied the 2cHF ground state in this molecule. Here we extend their analysis to the $^1\Pi$ excited states of BH with the 2cHF reference. The results are collected in Tab. 3.1. The FCI result shows the lowest excitations to the $^1\Pi$ states are doubly degenerate. UHF based methods (UCIS and TDUHF) break the $^1\Pi$ degeneracy as seen in Tab. 3.1, going from doubly degenerate states to non-degenerate energy levels of different oscillator strengths. Unlike UCIS or TDUHF, 2cCIS and TD2cHF leave the $^1\Pi$ state degenerate. To understand why, consider the UHF description of the valence orbitals. In the UHF picture, the 3σ orbitals mix in some λ'

contribution π_x character,

$$\phi^{\text{UHF}}_{\text{HOMO-1}} \approx 3\sigma(\beta) + \lambda'\pi_x(\beta) \tag{3.7}$$

$$\phi^{\text{UHF}}_{\text{HOMO}} \approx 3\sigma(\alpha) - \lambda'\pi_x(\alpha) \tag{3.8}$$

In the FCI, the exact ground state has significant contributions from the doubly occupied $\pi_{x,y}$ configurations, and this mixing in the UHF accounts for the π_x contribution (thereby missing the π_y contribution). Thus UHF breaks the degeneracy between π_x and π_y orbitals. This plays out in the TDUHF/UCIS description of the $^1\Pi$ states, which are essentially excitations from $3\sigma \rightarrow \pi_{x,y}$. Now consider the case in 2cHF. In 2cHF, the 3σ orbitals also mix in λ'' contribution from π_y, but of opposite spin, giving

$$\phi^{\text{2cHF}}_{\text{HOMO-1}} \approx 3\sigma(\beta) + \lambda''\pi_x(\beta) + \lambda''\pi_y(\alpha) \tag{3.9}$$

$$\phi^{\text{2cHF}}_{\text{HOMO}} \approx 3\sigma(\alpha) - \lambda''\pi_x(\alpha) + \lambda''\pi_y(\beta) \tag{3.10}$$

This mixing allows 2cHF to approximate both the FCI doubly occupied $\pi_{x,y}$ configurations, thereby lowering the energy relative to UHF. It also treats the π_x and π_y on equal footing, which restores the degeneracy of the $^1\Pi$ state.

Table 3.1: Lowest singlet excitation energies for neutral, singlet BH molecule in the 4-31G basis at 1.21Å bond length. The small oscillator strength arises from the fact that transition to $^1\Pi$ is of predominantly $p_z \rightarrow p_x$ character, which is forbidden.

BH, 4-31G, 1.21Å Excitation energy / eV (*Oscillator strength*)					
State	FCI	2cCIS	TD2cHF	UCIS	TDUHF
$^1\Pi$	3.17 (*0.03*)	3.24 (*0.03*)	3.14 (*0.03*)	3.17 (*0.03*)	3.10 (*0.03*)
	3.17 (*0.03*)	3.24 (*0.03*)	3.14 (*0.03*)	3.25 (*0.04*)	3.12 (*0.02*)

Complex 2cHF: Atomic Beryllium

Next, consider the neutral beryllium atom in a STO-6G basis. This is perhaps the simplest example of a system with a fundamentally complex 2cHF solution. Löwdin and Mayer also explored the 2cHF solutions of this system, though they were unable to investigate the complex solution. Because the 2cHF formalism implemented here may take complex-values, we obtained a lower energy solution than the real 2cHF solution considered by Löwdin and Mayer. Energetically, the difference is small. The complex 2cHF energy is 0.004 eV lower than the UHF energy and 0.001 eV lower than the real 2cHF energy. Here we consider ^{1}S $\rightarrow$^{1}P excitations to obtain insightful understanding of the characteristics of excited states from a 2cHF solution. In Tab. 3.2, the lowest-lying allowed excitations for full configuration interaction (FCI), UCIS, and 2cCIS are compared (and their LR-TDHF counterparts).

Table 3.2: Lowest singlet excitation energies for neutral, singlet Beryllium atom in the STO-6G basis. The oscillator strength is large and sums nearly to 1, as the transition is dominated by $2s \rightarrow 2p$, which is an allowed single electron transition. Note the large error of the TDHF/CIS methods compared to the FCI result, but close agreement among the approximate methods.

Be, STO-6G Excitation energy / eV (*Oscillator strength*)					
State	FCI	2cCIS	TD2cHF	UCIS	TDUHF
^{1}P	7.81 (*0.35*)	6.46 (*0.43*)	6.15 (*0.30*)	6.43 (*0.38*)	6.10 (*0.31*)
	7.81 (*0.35*)	6.46 (*0.43*)	6.15 (*0.30*)	6.47 (*0.47*)	6.10 (*0.31*)
	7.81 (*0.35*)	6.46 (*0.43*)	6.15 (*0.30*)	6.47 (*0.47*)	6.20 (*0.28*)

In FCI, the ^{1}P level is triply degenerate. In UCIS and TDUHF, the triple degeneracy of the ^{1}P states is broken into two levels with different oscillator strengths. These broken degeneracies are the result mixing of the $2p_z$ and $2s$ orbitals, which lowers the spherical symmetry to $D_{\infty h}$, and splits the triple spatial degeneracies in two (a single line and a pair of two). Now comparing to excited states from the 2cHF reference, we see a different pattern. Both TD2cHF and 2cCIS are able to obtain the correct energetic degeneracy of the ^{1}P term,

and all states in the ^{1}P term are associated with a same oscillator strength. For the Be HOMO, for example, we see a mixing roughly equating to

$$\phi_{\text{HOMO}}^{\text{Be,2cHF}} \approx (-0.89)2s(\beta)+(0.43)2s(\alpha)+(-0.15)2p_x(\beta)+(0.15)2p_y(\alpha)+(0.14i)2p_z(\alpha) \quad (3.11)$$

Like the BH molecule, the exact solution of the Be atom needs to mix in higher angular momentum configurations. Whereas BH needed only to mix in two configurations, the π_x and π_y, Be needs to mix in *three* configurations: $2p_x$, $2p_y$, and $2p_z$. 2cHF accommodates this by the extra degrees of freedom afforded by breaking spin symmetry as well as complex conjugation and time reversal symmetry. Previous studies of the 2cHF treatment of Be, which limited itself to only real 2cHF solutions, found a Be HOMO mixing[5] of

$$\phi_{\text{HOMO}}^{\text{Be,2cHF}} \approx (0.996)2s(\beta) + (-0.189)2p_y(\beta) + (0.189)2p_x(\alpha) \quad (3.12)$$

Notably, the $2p_z$ component is missing. Thus not only do TDUHF and UCIS have a nondegenerate ^{1}P, but, the real 2cHF ^{1}P states are also nondegenerate (though we do not show the results here). Only by treating all the $2p$ components equally — which is only possible in the single-determinant framework with complex 2cHF — can the ^{1}P degeneracy be restored. Furthermore, we see the multiconfigurational nature of 2cHF extends to the description of excited states. Despite this, there remains a large error between the approximate TDHF/CIS results and the FCI results. This is the result of neglecting electron correlation.

H_3 Trimer

The final system we consider is the neutral D_{3h} hydrogen trimer in the STO-3G basis, with a side length of 1Å. This model system is the simplest case of spin frustrated molecule, where the favored antiferromagnetic interactions between the three electrons cannot all be simultaneously optimized.[47] For such systems, 2cHF will always provide the lowest-energy mean-field solutions, regardless of basis. The minimal basis was chosen for this three-electron

system in order to keep the analysis simple; despite this consideration, we will see that even for this case analysis is difficult. Though the model H_3 has D_{3h} symmetry, we work in the C_{2v} point group. This is because D_{3h} is non-Abelian and cannot be represented by a single Slater determinant, which we use for our analysis. C_{2v} is a subgroup of D_{3h} and we can relate our results (where applicable — 2cHF breaks point group symmetry) in C_{2v} to D_{3h} through the appropriate correlation table.

A comparison of the ground and excited states of H_3 by the various methods is given in Tab. 3.3. The FCI results for H_3 show a quadruply degenerate ^{2}E ground state. UHF cannot obtain a degenerate D_{3h} ground state and instead breaks symmetry into a $^2A_1$ and $^2B_2$ ground state. The 2cHF ground state is 0.12 eV lower in energy than the UHF B_2 solution and 0.34 eV lower in energy than the UHF A_1 solution. For both UHF solutions, the first four states are low in energy. It appears UCIS is trying to capture the degeneracy of the true systems through four low lying non-equivalent solutions. Each solution can be rotated 120° to obtain a symmetry equivalent solution. In the case of 2cHF, any unitary rotation in spin space will give an equivalent solution. Regardless, all solutions give the same energies with equivalent excited states (and properties).

Interestingly, UCIS shows a negative excitation energy corresponding to a spin flip to a spatially degenerate orbital. This means that there is a UHF $\rightarrow$ 2cHF instability,[3,10] further evidence that the minimum-energy single Slater determinant lies in the 2cHF manifold. 2cCIS performs similarly, though it breaks point group symmetry entirely. It too has four low-lying states that correspond to the fourfold degeneracy of the FCI ground state. 2cCIS has no spin symmetry, so in Tab. 3.3 the states are listed in descending energetic order. The next state in the FCI is the $^4A_2$ state, which as a quartet is quadruply degenerate. UCIS and TDUHF are unable to capture the $M_s = -3/2$ state because the $\Delta M_s = 0, \pm 1$ constraint in the formalism. For 2cCIS and TD2cHF, this is not necessarily the case. As the constraint on M_s is relaxed in 2cHF, excited states in 2cCIS and TD2cHF are better able to maintain the degeneracy for this state in the FCI. That 2cCIS and TD2cHF can approximate the $M_s = -3/2$ is a testament to the fact that the expectation value of $\hat{S}_z$ for H_3 in the 2cHF picture is zero,

whereas $M_s = 1/2$ for UCIS.

To see this, observe that the 2cHF orbitals for minimal basis H_3 are

$$\phi_1 \approx 1a_1(\beta) \tag{3.13}$$

$$\phi_2 \approx 1a_1(\alpha) \tag{3.14}$$

$$\phi_3 \approx 2a_1(\alpha) + 1b_2(\beta) \tag{3.15}$$

$$\phi_4 \approx 2a_1(\alpha) - 1b_2(\beta) \tag{3.16}$$

$$\phi_5 \approx 2a_1(\beta) + 1b_2(\alpha) \tag{3.17}$$

$$\phi_6 \approx 2a_1(\beta) - 1b_2(\alpha) \tag{3.18}$$

We can see that 2cHF, despite breaking point group symmetry, gives a good approximation to the D_{3h} point group: two a_1 orbitals and four almost e' orbitals (that should be degenerate in principle, but are not in practice). Thus the ground state in 2cHF is

$$|\text{2cHF}\rangle \approx |1a_1(\beta)1a_1(\alpha)[2a_1(\alpha) + 1b_2(\beta)]\rangle \tag{3.19}$$

Which gives an almost ^{2}E ground state. If we took the expectation value of S_z on this state, it would return zero as the spin up and spin down portions cancel. This is observed in practice as 2cHF H_3 has a non-collinear magnetic orientation. Now consider a single excitation out of this 2cHF reference. If we consider, say the orbital swap $\phi_2 \rightarrow \phi_4$, we can get a component with the $M_s = -3/2$. This configuration is impossible to get from a single excitation out of a UHF ($M_s = 1/2$) reference.

Regarding the TD2cHF results, it is interesting to note the zero eigenvalues. This behavior was explored in detail by Cui, *et al.*[8] in connection with projected Hartree-Fock theory. Although the exact nature of the zero eigenvalues depends on the system at hand, for many systems with 2cHF solutions the zero eigenvalues originate from symmetry breaking, and the zero energy excitation is simply an excitation that changes the spin direction without changing the energy (see also the discussion in Reference 3). Here, in comparison to the FCI,

Table 3.3: Comparison of excited-state calculations for H_3 equilateral trimer, with side length of 1Å in a STO-3G minimal basis. The state designation on the right strictly holds for the FCI results. The 2cHF and UHF results were matched up to the corresponding FCI states, however, the comparison is not direct because CIS and TDHF for both 2cHF and UHF are unable to capture the fully multiconfigurational nature of higher FCI excited states. The lack of good spin quantum numbers in UHF and 2cHF prohibit characterization as proper spin states, though attempts were made to assign the correct M_s states for the UHF methods. Excited state methods based on 2cHF are listed in descending energetic order.

State			ΔE / eV						
				CIS			TDHF		
D_{3h}	C_{2v}	M_s	FCI	2cHF	UHF (A_1)	UHF (B_2)	2cHF	UHF (A_1)	UHF (B_2)
^2E	$^2A_1$	+1/2	0.00	0.00	0.00	2.27	0.00	0.00	2.10
	$^2A_1$	-1/2	0.00	0.47	0.00	-0.40	0.00	0.00	-0.40
	$^2B_2$	+1/2	0.00	0.47	0.54	0.00	0.00	1.53i	0.00
	$^2B_2$	-1/2	0.00	1.53	-0.19	0.75	0.00	2.25	0.00
$^4A_2$	$^4B_2$	+3/2	10.64	15.00	9.65	9.87	14.55	7.13	8.72
	$^4B_2$	+1/2	10.64	15.05	13.04	13.48	14.60	12.02	12.95
	$^4B_2$	-1/2	10.64	15.76	16.13	16.70	15.52	15.66	16.30
	$^4B_2$	-3/2	10.64	15.76	—	—	15.52	—	—
^2E	$^2A_1$	+1/2	19.01	21.52	20.11	20.77	21.36	20.11	20.24
	$^2A_1$	-1/2	19.01	21.52	20.11	20.24	21.36	20.11	20.63
	$^2B_2$	+1/2	19.01	—	21.13	21.40	—	20.56	21.06
	$^2B_2$	-1/2	19.01	—	—	—	—	—	—

the TD2cHF zeros point toward the quadruply degenerate ground state. Also of note is the pure imaginary eigenvalue in the TDUHF (A_1) results. This shows an underlying instability to the lower-energy B_2 UHF solution. The existence of imaginary roots in the TDHF/RPA equations as a result of an underlying instability is a well known phenomenon, and has also been addressed by Cui, *et al.*[8] (and references therein).

Conclusion

Here we implemented two single-reference excited-state methods based on the two-component Hartree-Fock method (2cCIS and TD-2cHF). We compare their performance to a UCIS,

TDUHF, and FCI description of the excited states. In situations where the 2cHF and UHF ground state is not dramatically different, for example in Be and BH, 2cHF and UHF compute roughly the same excitations and oscillator strengths. Qualitatively, however, excited-state methods based on 2cHF maintain the degeneracy of the systems better than UHF does. UHF tends to split peaks and states that should remain degenerate. For spin frustrated systems, like H_3, the situation becomes more complicated. Again, 2cHF tends to maintain any degeneracies found in the FCI. However, there is often a large difference in energy compared to the FCI results, which is the result of neglecting electron correlation.

Using 2cHF for excited states with the projected Hartree-Fock method would be an interesting next direction. Although PHF results in excitation energies that are no longer size intensive nor single-reference, it would be possible to restore the good quantum numbers that 2cHF abandons at mean field cost. The possible benefit of this approach is to project out the undesirable components of the excited determinants that contaminate the solutions. In other words, 2cHF brings the multireference character to the description of the excited states. Once the spin contaminants are eliminated, the resulting solution is a mean-field multi-reference description of excited states. Such work has been attempted,[58,59] though the extension to (complex) 2cHF remains to be seen.

Finally, 2cHF is a non-relativistic approximation to the relativistic two-component methods. Two-component methods in relativistic electronic structure theory, such as the Douglas-Kroll-Hess (DKH)[60–63] or Normalized Elimination of the Small Component (NESC),[64–68] have the same mathematical structure as 2cHF: they may take on a linear combination of spin-up and spin-down functions as well as complex values. The only difference between these relativistic methods and 2cHF is the Hamiltonian. For light elements, 2cHF and relativistic two-component methods may predict nearly the same phenomena. For H_3, for example, it is likely that 2cHF and two-component DKH would predict the same spectra. It would appear that some of the caveats discussed here are directly applicable to relativistic two-component methods. In particular, it may appear that these relativistic methods are able to handle complex magnetic phenomena at the single-reference level, when in reality a multi-reference

description is required. DKH, NESC, or even the four-component Dirac-Fock equations may be just as good (or bad) as 2cHF in the non-relativistic limit. However, it may be difficult to disentangle which effects are the result of new physics and which are the result of the failure of the underlying mean-field reference. For example, is an excited state no longer degenerate because of spin-orbit coupling, or because of a failure of the single two-component Slater determinant? This remains an open question. Careful discernment is required when properly describing the magnetic interactions and excited states of such complex magnetic molecules.

Chapter 4

REAL-TIME PROPAGATION OF THE EXACT TWO-COMPONENT TIME-DEPENDENT DENSITY FUNCTIONAL THEORY

We report the development of a real-time propagation method for solving the time-dependent relativistic exact two-component density functional theory equations (RT-X2C-TDDFT). The method is fundamentally non-perturbative and may be employed to study nonlinear-responses for heavy elements, which require a relativistic Hamiltonian. We apply the method to several Group 12 atoms as well as heavy-element hydrides, comparing with the extensive theoretical and experimental studies on this system, which demonstrates the correctness of our approach. Because the exact two-component Hamiltonian contains spin-orbit operators, the method is able to describe the non-zero transition moment of otherwise spin-forbidden processes in non-relativistic theory. Furthermore, the two-component approach is more cost effective than the full four-component approach, with similar accuracy. The RT-X2C-TDDFT will be useful in future studies of systems containing heavy elements interacting with strong external fields. The work in this chapter was reproduced with permission from Joshua J. Goings, Joseph M. Kasper, Franco Egidi, Shichao Sun, and Xiaosong Li. Real-time propagation of the exact two-component time-dependent density functional theory. *J. Chem. Phys.*, 145(10):104107, 2016.

Introduction

Relativistic effects are known to be important for the description of heavy elements. For example, the yellow color of gold and the fact that mercury is liquid at room temperature are both explained by including relativistic corrections to the non-relativistic Schrödinger

equation.[69–71] The proper starting point for the description of molecular relativistic effects is the Dirac-Hartree-Fock/Dirac-Kohn-Sham four-component Hamiltonian. However, because of its four-component nature, the Dirac-Hartree-Fock/Dirac-Kohn-Sham Hamiltonian quickly becomes an expensive Hamiltonian to use in realistic calculations involving heavy elements. Furthermore, there is additional work in the full four-component calculations in that the Dirac equation also contains negative-energy solutions corresponding to positronic solutions.[69,70] These are often of little interest to chemical applications. Therefore, much effort has been spent to decouple the four-component equations into two-component electronic and positronic equations, which retain the physical relativistic effects of the full four-component equations, but at reduced cost.[69,70]

One of the most promising two-component methods in recent times has been the introduction of the exact two-component transformation (X2C).[16–19,72–77] X2C approximately decouples the parent four-component Hamiltonian into a reduced-dimension electronic two-component Hamiltonian. For one-electron systems, X2C will recover the exact four-component eigenspectrum of the underlying four-component Dirac equation. Other two-component methods of note are the normalized elimination of the small component (NESC),[64–68] the Douglas-Kroll-Hess transformation,[60–63] and the zeroth-order-regular approximation (ZORA).[75,78–80] Relations between these methods have been detailed in Ref. 76.

Given the success of such relativistic Hamiltonians for ground-state properties, it is natural to consider the effectiveness of their extension to excited-state properties, such as optical absorption spectra. In particular, relativistic effects are necessary to qualitatively describe excited states split by spin-orbit and spin-spin interactions. Both four-component and two-component relativistic Hamiltonians have been successfully applied to the description of excited states using the linear-response (LR) formalism.[20,51,81–90] However, the linear-response formalism is fundamentally limited to system response of small, perturbative fields. If one desires to compute nonlinear-response properties and the response of systems containing heavy elements in strong fields, it may be necessary to employ a real-time propagation approach[11,91,92] to the time-dependent relativistic equations.

Recently, a real-time (RT) propagation approach for the four-component Dirac-Kohn-Sham equations was presented.[13] The method was able to describe the response to strong fields of systems within a fully relativistic theory, and was able to describe spin-forbidden transitions and other unique relativistic aspects of optical absorption spectra. Unfortunately, because of the underlying four-component Hamiltonian, the solution of the equations is rather expensive. Here, we present a real-time propagation approach utilizing the time-dependent two-component X2C Hamiltonian. The solution of these equations provides an economical approach to describing the response of systems containing heavy elements. We briefly describe the two-component transformation and our real-time propagation scheme for two-component Hamiltonians, based on our previous work propagating non-relativistic two-component equations.[1,11] We demonstrate the correctness of our approach by comparing with linear-response two-component time-dependent density functional theory (TDDFT), as well as the four-component RT-TDDFT results. Finally, we look forward to the potential of real-time time-dependent X2C for strong fields and spin-dependent dynamics.

Theory

Here we briefly outline the exact two-component transformation, using atomic units. We follow the notation of Peng, *et al.*, as our implementation closely follows the X2C implementation outlined in their paper.[19] Bold formatted $\mathbf{M}$ indicates matrices in two-component (2c) space, and for matrix representation of four-component operators we use the split notation for large (L) and small (S) components. In some cases, four-component (4c) matrices will be indicated by blackboard bold $\mathbb{M}$. Finally, sans-serif matrices M correspond to complex matrices in a basis set of spin-free functions. We refer interested readers to Ref. 19 for more details. The goal of X2C, as with most two-component methods, is to exactly decouple the large and small components of the four-component one-electron modified Dirac equation. X2C accomplishes this goal by exactly decoupling the one-electron Dirac equation represented in a restricted

kinetically balanced basis, given as

$$\begin{aligned}
&\begin{pmatrix} \mathbf{V} & \mathbf{T} \\ \mathbf{T} & (\frac{1}{4c^2}\mathbf{W} - \mathbf{T}) \end{pmatrix} \begin{pmatrix} \mathbf{C}_L^+ & \mathbf{C}_L^- \\ \mathbf{C}_S^+ & \mathbf{C}_S^- \end{pmatrix} \\
&= \begin{pmatrix} \mathbf{S} & \mathbf{0} \\ \mathbf{0} & \frac{1}{2c^2}\mathbf{T} \end{pmatrix} \begin{pmatrix} \mathbf{C}_L^+ & \mathbf{C}_L^- \\ \mathbf{C}_S^+ & \mathbf{C}_S^- \end{pmatrix} \begin{pmatrix} \epsilon^+ & \mathbf{0} \\ \mathbf{0} & \epsilon^- \end{pmatrix}
\end{aligned} \tag{4.1}$$

Here $\mathbf{V}$, $\mathbf{T}$, and $\mathbf{S}$ are the non-relativistic matrix representations of the one-electron potential energy operator ($\mathcal{V}$), the kinetic energy operator, and the overlap, respectively. $\mathbf{W}$, however, is the relativistic potential energy operator, represented as

$$W_{ij} = \langle \chi_i | \ \vec{\sigma} \cdot \vec{p} \ \mathcal{V} \ \vec{\sigma} \cdot \vec{p} \ | \chi_j \rangle \tag{4.2}$$

where $\vec{p}$ is the linear momentum vector and $\vec{\sigma}$ is the vector containing the Pauli spin operators. All the matrices are represented over two-component spinor functions, $\{\chi_i\}$. Finally, c is the speed of light and $\mathbf{C}$ and ϵ collect the wave function coefficients and orbital energies, respectively.

To decouple Eq. (4.1), we seek a unitary transformation $\mathbb{U}$ that block diagonalizes the 4c Dirac Hamiltonian into two two-component equations. The decoupled equations will correspond to positive- and negative-energy states, and we seek solutions only to the positive-energy solutions, which correspond to electronic solutions. Mathematically, we seek to find $\mathbb{U}$ such that

$$\tilde{\mathbf{H}} = \begin{pmatrix} \mathbf{U}^{LL,\dagger} & \mathbf{U}^{SL,\dagger} \end{pmatrix} \begin{pmatrix} \mathbf{V} & \mathbf{T} \\ \mathbf{T} & (\frac{1}{4c^2}\mathbf{W} - \mathbf{T}) \end{pmatrix} \begin{pmatrix} \mathbf{U}^{LL} \\ \mathbf{U}^{SL} \end{pmatrix} \tag{4.3}$$

is satisfied. In the X2C method, the matrix representation of $\mathbb{U}$ is given by

$$\mathbb{U} = \begin{pmatrix} \mathbf{U}^{LL} & \mathbf{U}^{LS} \\ \mathbf{U}^{SL} & \mathbf{U}^{SS} \end{pmatrix} = \begin{pmatrix} \frac{\mathbf{I}}{\sqrt{\mathbf{I}+\mathbf{X}'^{\dagger}\mathbf{X}'}} & -\mathbf{X}'^{\dagger}\frac{\mathbf{I}}{\sqrt{\mathbf{I}+\mathbf{X}'\mathbf{X}'^{\dagger}}} \\ \mathbf{X}'\frac{\mathbf{I}}{\sqrt{\mathbf{I}+\mathbf{X}'^{\dagger}\mathbf{X}'}} & \frac{\mathbf{I}}{\mathbf{I}+\mathbf{X}'\mathbf{X}'^{\dagger}} \end{pmatrix} \tag{4.4}$$

which only holds in an orthonormal basis, denoted by the primes. The X2C method extracts a matrix representation of $\mathbf{X}'$ by solving the one-electron modified Dirac Hamiltonian in an orthonormal basis.

$$\mathbb{H}' \begin{pmatrix} \mathbf{C}^{+}_{L'} \\ \mathbf{C}^{+}_{S'} \end{pmatrix} = \begin{pmatrix} \mathbf{C}^{+}_{L'} \\ \mathbf{C}^{+}_{S'} \end{pmatrix} \epsilon^{+} \tag{4.5}$$

From the solution of Eq. (4.5), the explicit matrix expression for $\mathbf{X}'$ can be obtained from the wave function coefficients

$$\mathbf{X}' = \mathbf{C}^{+}_{S'} \cdot \left(\mathbf{C}^{+}_{L'}\right)^{-1} \tag{4.6}$$

Plugging Eq. (4.6) into Eq. (4.4) and generating the X2C Hamiltonian via Eq. (4.3) defines our transformation from 4-component to 2-component in the X2C method.

The extension to many-electron systems corresponds to the same transformation in Eq. (4.3) but for the modified four-component Dirac-Hartree-Fock equation. In our implementation, we do not transform the matrix representation of the two-electron operator. This is equivalent to the Dirac-Coulomb approximation for the two-electron operator. We do, however, include an empirical correction in the one-electron terms to account for the screening due to the two-electron terms.[93] Furthermore, the two-electron interactions depend on the X2C density, which generates some relativistic dependence to the two-electron interaction.

$$\mathsf{F}^{\sigma\sigma'} = \mathsf{h}^{\sigma\sigma'} + \delta_{\sigma\sigma'}\mathsf{J}\left(\mathsf{P}^{\alpha\alpha} + \mathsf{P}^{\beta\beta}\right) - \theta\mathsf{K}\left(\mathsf{P}^{\sigma\sigma'}\right) - (1-\theta)\mathsf{V}_x^{\mathrm{DFT}}\left(\mathsf{P}^{\sigma\sigma'}\right) + \mathsf{V}_c^{\mathrm{DFT}}\left(\mathsf{P}^{\sigma\sigma'}\right) \tag{4.7}$$

Here h contains the transformed one-electron integrals, J contains the Coulomb integrals, and K contains the exchange integrals. σ denotes a spin-projection component, spin-up

(α) or spin-down (β). $\mathsf{V}_x^{\mathrm{DFT}}$ and $\mathsf{V}_c^{\mathrm{DFT}}$ are the DFT exchange and correlation functionals, respectively. θ denotes a mixing parameter that mixes in a certain amount of Hartree-Fock exchange. For pure DFT θ is zero and for pure Hartree-Fock $\theta = 1$. (For pure Hartree-Fock we omit $\mathsf{V}_c^{\mathrm{DFT}}$ as well.)

Density functionals commonly developed for quantum chemical calculations are only formulated for systems with a collinear density for which the spin magnetization is oriented along the z axis at every point in space. Common exchange-correlation kernels only depend on $\mathsf{P}^{\alpha\alpha}$ and $\mathsf{P}^{\beta\beta}$ therefore, in order to use such functionals to describe systems with a non-collinear spin magnetization, the functional dependence must be reformulated to account for the presence of a non-zero magnetization oriented along the x and y directions, as well as their gradients (in the case of GGA functionals) in Eq. (4.7). The non-collinear XC kernel for 4c methods has been explored by Liu, *et al.*[81,85,86,94] We employ a recently reported formalism[9,24,25,44] that defines a set of auxiliary variables, detailed in Ref. 25, that take all magnetization components into account. This form has the advantage of exerting a non-zero local torque acting on the magnetization, while yielding a vanishing total torque, as expected from the exact functional.[95]

To propagate the X2C equations in time, we must consider the time-dependent version of the X2C Hamiltonian.

$$i\frac{\partial}{\partial t}\begin{pmatrix} \mathsf{P}^{\alpha\alpha}(t) & \mathsf{P}^{\alpha\beta}(t) \\ \mathsf{P}^{\beta\alpha}(t) & \mathsf{P}^{\beta\beta}(t) \end{pmatrix} = \left[\begin{pmatrix} \mathsf{F}^{\alpha\alpha}(t) & \mathsf{F}^{\alpha\beta}(t) \\ \mathsf{F}^{\beta\alpha}(t) & \mathsf{F}^{\beta\beta}(t) \end{pmatrix}, \begin{pmatrix} \mathsf{P}^{\alpha\alpha}(t) & \mathsf{P}^{\alpha\beta}(t) \\ \mathsf{P}^{\beta\alpha}(t) & \mathsf{P}^{\beta\beta}(t) \end{pmatrix}\right] \tag{4.8}$$

We integrate Eq. (4.8) with a modified midpoint and unitary transformation (MMUT) algorithm.[91,96,97] In the MMUT method, the time-evolution operator is a unitary transformation matrix $\mathbf{Q}(t_n)$ that is constructed from the eigenvectors $\mathbf{C}(t_n)$ and eigenvalues $\epsilon(t_n)$ of the X2C Hamiltonian matrix at time t_n:

$$\mathbf{C}^{\dagger}(t_n) \cdot \mathbf{F}(t_n) \cdot \mathbf{C}(t_n) = \epsilon(t_n) \tag{4.9}$$

and

$$\begin{aligned}\mathbf{Q}(t_n) &= \exp\left[-i \cdot 2\Delta t \cdot \mathbf{F}(t_n)\right] \\ &= \mathbf{C}(t_n) \cdot \exp\left[-i \cdot 2\Delta t \cdot \epsilon(t_n)\right] \cdot \mathbf{C}^{\dagger}(t_n)\end{aligned} \tag{4.10}$$

where Δt is the time step. Then, the density matrix is propagated from time t_{n-1} to t_{n+1} using the time-evolution operator $\mathbf{Q}(t_n)$:

$$\mathbf{P}(t_{n+1}) = \mathbf{Q}(t_n) \cdot \mathbf{P}(t_{n-1}) \cdot \mathbf{Q}^{\dagger}(t_n) \tag{4.11}$$

The MMUT method accounts for linear changes in the density matrix during the time step because it computes the X2C Hamiltonian matrix at the midpoint. MMUT is a symplectic integration scheme which allows for a large step size, while simultaneously controlling for numerical noise and integration errors.[91]

To excite all dipole-allowed electronic transitions, it is necessary to perturb Eq. (4.7) with an electric field along each real-space coordinate (e.g. x, y, z). This modifies the X2C Hamiltonian matrix such that

$$\mathbf{F}_{\mathrm{E}}(t) = \mathbf{F}(t) + \sum_{q=x,y,z} \kappa(t)\langle r_q \rangle \tag{4.12}$$

where $\mathbf{F}_{\mathrm{E}}(t)$ is the time-dependent X2C Hamiltonian matrix containing the external electric field, $\kappa(t)$ is the field strength at time t, and $\langle r_q \rangle$ are the atomic-orbital based length-gauge dipole integrals along component q. The electric dipole operator matrix $\langle r_q \rangle$ used in the propagation is subject to the X2C picture-change transformation. In the electric-dipole approximation in the length gauge, the electric field does not couple different spin components.[11,98] As a result, the X2C transformation matrix is invariant with respect to an external electric field perturbation. Therefore, the same X2C transformation matrix is used to transform the electric dipole operator matrix that goes into Eq. (4.12).

Because time is discretized, the perturbation corresponds to a step function lineshape lasting for only the initial time-step of width Δt, e.g.

$$\kappa(t) = \begin{cases} \kappa_{\max}, & 0 \leq t < \Delta t, \\ 0, & \text{else} \end{cases} \tag{4.13}$$

in this case, the discrete Fourier transform of $\kappa(t)$ will simply be $\kappa_{\max}$. One important caveat for including the electric dipole field in the X2C equations is that the atomic orbital electric dipole integrals must also be transformed using the transformation matrix in Eq. (4.4). This corrects for the so-called "picture-change" error in two-component methods that originates from transforming the four-component picture to the two-component picture.[99]

Results and Discussion

The real-time propagation of the X2C Hamiltonian was implemented in a locally modified copy of the developer's version of the Gaussian electronic structure program.[100] All calculations were performed using the SVWN5[101,102] density functional with the Sapporo-DKH3-DZP-2012 gaussian basis set including diffuse-*sp* functions.[103] The density functional and basis set were chosen in order to be able to compare with existing relativistic response theory implementations, which will be discussed below. After a ground-state density optimization, each system was perturbed with an electric dipole delta pulse corresponding to a $\kappa_{\max}$ of 0.0001 au (0.00514 V$\cdot\mathring{A}^{-1}$) along each unique Cartesian axis. Each real-time calculation was propagated using a maximum time step of 0.0012 fs for at least 50 fs. Energy was conserved to at least 10^{-8} E_h. To accelerate the convergence of the Fourier transform, a Padé transformation scheme was utilized.[104] The electric dipole response was exponentially damped so as to give each peak a Lorentzian line shape with full-width half-max of 0.01 eV.

To obtain the optical absorption spectra, we take the Fourier transform of the time-dependent electric dipole moment $\mu(\omega)$ parallel to the polarization of the electric field perturbation κ. This corresponds to the frequency-dependent polarizability. The isotropic

dipole strength function $S(\omega)$ is proportional to the imaginary component of the trace of the frequency-dependent polarizability. That is to say,

$$S(\omega) \propto \sum_{\alpha=x,y,z} \mathrm{Tr}\left[\omega \cdot \mathrm{Im}\frac{\mu_\alpha(\omega)}{\kappa_\alpha}\right] \tag{4.14}$$

In order to test our implementation, we follow the pioneering four-component RT-TDDFT work of Repisky, *et al.*[13] and choose to study the excitation energies of three Group 12 atoms and two heavy-element hydrides. This allows us to compare not only with a four-component RT-TDDFT implementation, but also to compare with several four-component and two-component relativistic LR-TDDFT implementations.[51,81–84,90] Furthermore, there exist robust experimental data for these systems, which allows us to compare directly with experiment. For the heavy-element hydrides, TlH and AuH, experimental equilibrium geometries were used ($r_{Tl-H} = 1.8702$ Å, $r_{Au-H} = 1.52385$ Å) in accordance with previous investigations.[105,106]

We begin by investigating the Group 12 atoms, which have been throughly investigated both experimentally and theoretically. The states that we investigate correspond to s to p type transitions. Because our RT-TDDFT method can only detect electronically allowed transitions, the only reason we are able to detect the singlet-to-triplet transitions (to $^3\mathrm{P}_1$ states) is because the two-component X2C Hamiltonian includes spin-orbit couplings which allow the otherwise spin-forbidden transitions to become weakly allowed. The spectra are given in Fig. 4.1. For Zn (and to some extent Cd), the spin-forbidden transition appears almost non-existent. Despite this, the two-component X2C RT-TDDFT method can still observe a slight optical transition, which is observed experimentally. By the time we get to Hg, the singlet-to-triplet transition is relatively intense. A comparison of our results with both four-component RT-TDDFT and four- and two-component LR-TDDFT is given in Tab. 4.1. In general we find excellent agreement with both four- and two-component methods for RT-TDDFT and LR-TDDFT, as well as the experimental values obtained from Ref. 105. The relatively slight differences between methods likely corresponds to differences in the choice of basis set.

Finally, we compare our results for two diatomic heavy-element hydrides, TlH and AuH. These too have been the subject of much experimental and theoretical studies. Plots of the computed absorption spectrum are given in Figs. 4.2 and 4.3 and comparison of selected low energy states with existing theoretical methods are given in Tab. 4.2. For TlH, we examine the two lowest states, corresponding to $^3\Pi$ and $^1\Pi$ states. Our results for TlH agree very closely with the two-component ZORA with Slater-type functions obtained by Wang, *et al.*. We observe a non-zero transition moment to the $^3\Pi$ state, which is possible only because our two-component X2C Hamiltonian contains spin-orbit interactions to allow this otherwise spin-forbidden transition. We observe a similar behavior with AuH, and our results are only a few hundredths of an eV different from both four- and two- component results. We also note that our results, along with the other literature results, agree strongly with the experimental data, taken from Ref. 106.

Conclusion

Here we have implemented a real-time propagation method for solving the relativistic two-component time-dependent X2C equations within the context of density functional theory. We have compared our results for a variety of simple benchmark systems that have been thoroughly investigated by four- and two-component relativistic methods based on both real-time and linear-response approaches. Our results show very good agreement with previous studies. We show that the accuracy of our method is comparable to the full four-component relativistic equations, yet with reduced cost because we work within the two-component space. This is the clearest advantage over the previously reported real-time four-component TDDFT method. Because the real-time approach is fundamentally non-perturbative, this method is easily extended to study non-linear-responses and molecules in strong fields, which is not possible within the linear-response formalism. Additionally, because the two-component X2C includes spin-orbit operators, this method will be suitable for the description of otherwise spin-forbidden transitions as well as for the description of spin-orbit corrections to high-energy excited states, such as those found in X-ray spectroscopy.

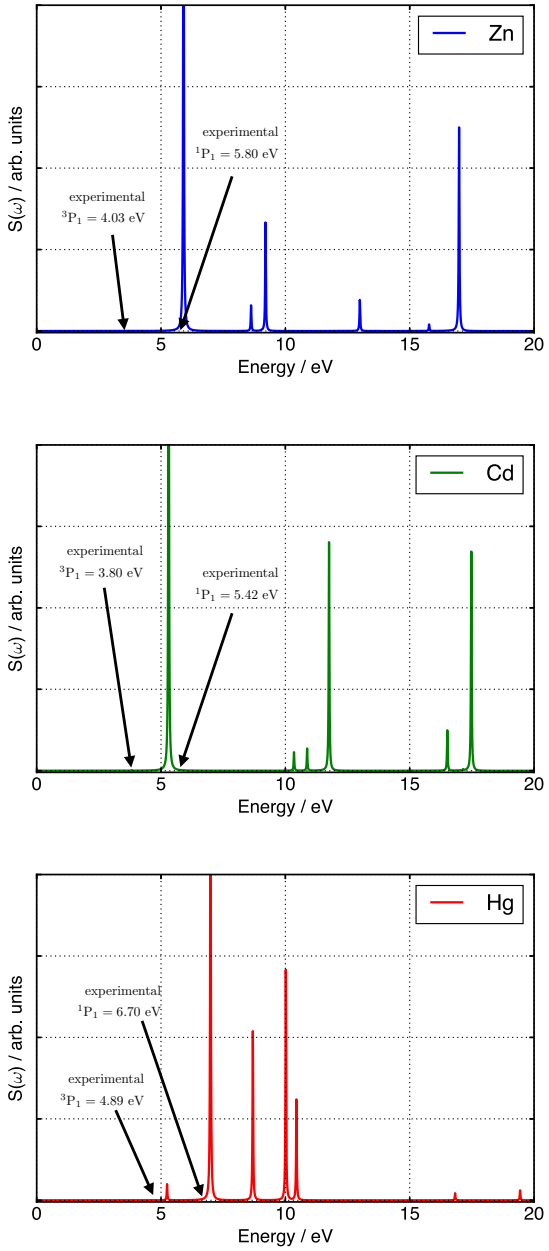

Figure 4.1: Computed optical absorption spectra of (a) Zn, (b) Cd, and (c) Hg using RT-X2C-TDDFT within the SVWN5/Sapporo-DKH3-2012 level of theory with diffuse-*sp* functions.

Table 4.1: Calculated $ns^2 \rightarrow ns^1np^1$ Excitation Energies of Group 12 Atoms ($n = 4 - 6$ for Zn, Cd, Hg)

		Excitation Energy (eV)							
		RT-TDDFT		LR-TDDFT					
atom	state	this work	Repisky[13]	Gao[81]/Li[90]	Bast[82]	Wang[83]	Nakata[84]	Kühn[51]	exp[105]
Zn	$^1P_1$	5.90	5.84	6.07/5.77	5.76	5.76	6.20	—	5.80
	$^3P_1$	4.30	4.30	4.40/4.35	4.35	4.35	4.41	—	4.03
Cd	$^1P_1$	5.31	5.44	5.50/5.47	5.34	5.35	5.74	5.47	5.42
	$^3P_1$	3.82	4.02	4.04/4.03	4.02	4.02	4.11	4.12	3.80
Hg	$^1P_1$	6.99	6.56	6.66/6.54	6.53	6.53	6.85	6.57	6.70
	$^3P_1$	5.24	5.06	5.12/5.10	5.08	5.09	5.26	5.12	4.89

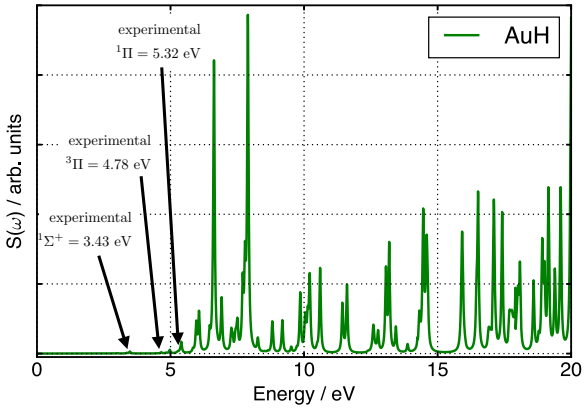

Figure 4.2: Computed optical absorption spectra of AuH using RT-X2C-TDDFT within the SVWN5/Sapporo-DKH3-2012 level of theory with diffuse-*sp* functions. The AuH bond length corresponds to an experimental equilibrium length of 1.52385 Å.

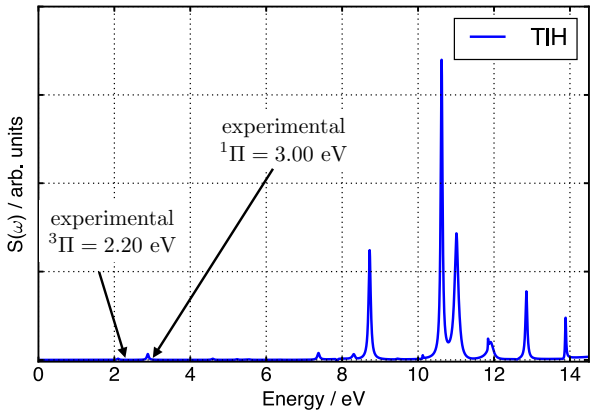

Figure 4.3: Computed optical absorption spectra of TlH using RT-X2C-TDDFT within the SVWN5/Sapporo-DKH3-2012 level of theory with diffuse-*sp* functions. The TlH bond length corresponds to an experimental equilibrium length of 1.8702 Å.

Table 4.2: Vertical Excitation Energies of Low-Lying Electronic States of TlH and AuH

		Excitation Energy (eV)					
		RT-TDDFT		LR-TDDFT			
molecule	state	this work	Repisky[13]	Wang[83]	Gao[81]	Kühn[51]	exp[106]
TlH	$^3\Pi$	2.10	2.07	2.08	—	2.09	2.20
	$^1\Pi$	2.88	2.96	2.88	—	2.64	3.00
AuH	$^1\Sigma^+$	3.48	3.31	3.42	3.39	—	3.43
	$^3\Pi$	4.65	4.52	4.70	4.66	—	4.78
	$^1\Pi$	4.98	5.21	5.01	4.96	—	5.32

Chapter 5

AN ATOMIC ORBITAL BASED REAL-TIME TIME-DEPENDENT DENSITY FUNCTIONAL THEORY FOR COMPUTING ELECTRONIC CIRCULAR DICHROISM BAND SPECTRA

One of the challenges of interpreting electronic circular dichroism (ECD) band spectra is that different states may have different rotatory strength signs, determined by their absolute configuration. If the states are closely spaced and opposite in sign, observed transitions may be washed out by nearby states, unlike absorption spectra where transitions are always positive additive. To accurately compute ECD bands, it is necessary to compute a large number of excited states, which may be prohibitively costly if one uses the linear-response time-dependent density functional (TDDFT) framework. Here we implement a real-time, atomic-orbital based TDDFT method for computing the entire ECD spectrum simultaneously. The method is advantageous for large systems with a high density of states. In contrast to previous implementations based on real-space grids, the method is variational, independent of nuclear orientation, and does not rely on pseudopotential approximations, making it suitable for computation of chiroptical properties well into the X-ray regime. The work in this chapter was adapted with permission from Joshua J. Goings and Xiaosong Li. An atomic orbital based real-time time-dependent density functional theory for computing electronic circular dichroism band spectra. *J. Chem. Phys.*, 144(23):234102, 2016.

Introduction

The phenomenon of chirality is of enormous importance to effective drug[107] and materials design,[108,109] as well as characterization of biological molecules[110] and even understanding

the origin of life as we know it.[111] One of the hallmarks of chiral molecules is that pairs of enantiomers show a differential absorption of left- and right-handed circularly polarized light.[112] The difference in the absorption spectra from left- and right-handed circularly polarized light leads to the circular dichroism (CD) spectrum. The underlying phenomenon of natural optical activity, that is, the system shows circular dichroism without the influence of external magnetic fields, is unique to chiral molecules. Thus electronic circular dichroism, ECD, (as well as vibrational circular dichroism, VCD) is a powerful tool for characterizing and determining absolute configurations of enantiomers.

From a theoretical perspective, there are several ways to compute the ECD spectrum of a chiral molecule. The most common methods are based on the response formalism.[113,114] The response theory approach toward computing circular dichroism has been applied to nearly all ab-initio methods, including coupled-cluster[115] and density functional theory.[116–119] Coupled cluster is usually more robust, though not without its challenges.[120] Linear-response time-dependent density functional theory (LR-TDDFT) has proven to be more economical, though certainly not perfect for any system. A detailed investigation of the linear-response second-order coupled-cluster (LR-CC2) method, linear-response time-dependent Hartree-Fock (LR-TDHF), and LR-TDDFT has been given by Diedrich and Grimme.[121]

To determine a CD spectrum in practice requires the computation of many states over a band. For large molecules with a high density of states, linear-response methods become cost prohibitive, as solving the full ECD spectrum in the LR-TDDFT framework formally scales as $\mathrm{O}(N^6)$. Several methods to avoid calculating a large number of excited states in LR-TDDFT have been proposed. In particular, the complex polarization propagator — or damped linear-response theory — method is one technique to computed an ECD spectrum without explicitly computing a large number of states.[122,123] Other approaches based on energy windowing may also be used to solve the linear-response theory in a given energy window.[124–126]

Alternatively, one way around this bottleneck is to solve the same time-dependent Hartree-Fock/Kohn-Sham equations explicitly in the time domain. More recently, TD-DFT methods

based within the real-time formalism (RT-TDDFT) have been presented for computing the ECD spectrum of molecules.[127,128] The real-time approach not only can provide similar information to the LR-TDDFT, but for extremely large systems will be the most cost-effective method. This point has been addressed recently in a comparison between the efficiency of LR-TDDFT and RT-TDDFT.[129] Thus RT-TDDFT can, in principle, enable ECD (and other excited-state properties) for larger biomolecules and chiral carbon nanotubes, where even the LR-TDDFT method cannot be applied.

Until this point, all RT-TDDFT methods for computing ECD have been grid-based instead of atomic orbital (AO) based.[130] While there are many advantages to the grid-based method, there are some pitfalls that make an AO-based method more desirable. Among these are the fact that grid-based methods are not variational and they depend on relative nuclear orientation with respect to the grid, leading to the so-called "egg-box" effect.[130] The AO-based approach resolves these problems, because AO-based TDDFT is well known to be a variational method, and AO-based methods have an atom-centered basis, which eliminates problems with nuclear origin dependence. This lays the groundwork for CD spectroscopies involving nuclear motion, for example VCD. Furthermore, AO-based methods can be applied to extremely-high-energy states, where grid-based methods must rely on pseudopotential approximations,[130] enabling computation of CD bands well into the X-ray region.

Here we present an AO-based RT-TDDFT implementation for computing the ECD spectrum of large chiral molecules. We compare our results to the LR-TDDFT formalism to show the consistency of the method for several molecules, discuss some of the problems that the method still retains, and then look to the future of AO-based RT-TDDFT methods for the simulation of CD spectra of large systems.

Theory

Solution of the RT-TDDFT equations

Here, we briefly outline the propagation of the time-dependent Hartree-Fock/Kohn-Sham equations. For a detailed account of the propagation, see References 91, 96 and 97. In the AO basis, the Fock/Kohn-Sham matrix can be written as

$$\mathbf{K} = \mathbf{h} + \mathbf{G}_{xe}[\mathbf{P}] + \alpha \cdot \mathbf{V}_{xc}[\mathbf{P}]. \tag{5.1}$$

where $\mathbf{h}$ is the core Hamiltonian matrix, $\mathbf{G}_{xe}$ is the density $\mathbf{P}$ dependent two-electron integral matrix, and $\mathbf{V}_{xc}$ is the density-dependent Kohn-Sham exchange correlation matrix. The scalar α controls the amount of the DFT exchange-correlation mixed into the Fock/Kohn-Sham matrix. For pure DFT $\alpha = 1$, whereas for pure Hartree-Fock, $\alpha = 0$. Hybrid functionals may take a fractional value of α between 0 and 1. In the orthonormal basis (here denoted by the primed notation), the TDHF/TDDFT equations are given by

$$i\frac{\partial \mathbf{P}'}{\partial t} = \left[\mathbf{K}', \mathbf{P}'\right]. \tag{5.2}$$

The time-dependent Eq. (5.2) are integrated with a modified midpoint and unitary transformation (MMUT) algorithm.[91,96,97] In the MMUT method, the time-evolution operator is a unitary transformation matrix $\mathbf{U}(t_n)$ that is constructed from the eigenvectors $\mathbf{C}(t_n)$ and eigenvalues $\boldsymbol{\epsilon}(t_n)$ of the Fock or Kohn-Sham matrix at time t_n:

$$\mathbf{C}^{\dagger}(t_n) \cdot \mathbf{F}(t_n) \cdot \mathbf{C}(t_n) = \boldsymbol{\epsilon}(t_n) \tag{5.3}$$

$$\begin{aligned}\mathbf{U}(t_n) &= \exp\left[-i \cdot 2\Delta t \cdot \mathbf{F}(t_n)\right] \\ &= \mathbf{C}(t_n) \cdot \exp\left[-i \cdot 2\Delta t \cdot \boldsymbol{\epsilon}(t_n)\right] \cdot \mathbf{C}^{\dagger}(t_n)\end{aligned} \tag{5.4}$$

where Δt is the time step. Then, the density matrix is propagated from time t_{n-1} to t_{n+1}

using the time-evolution operator $\mathbf{U}(t_n)$:

$$\mathbf{P}(t_{n+1}) = \mathbf{U}(t_n) \cdot \mathbf{P}(t_{n-1}) \cdot \mathbf{U}^{\dagger}(t_n) \tag{5.5}$$

The MMUT method accounts for linear changes in the density matrix during the time step because it computes the Fock or Kohn-Sham matrix at the midpoint. One of the advantages of the MMUT method is that a large step size can be taken, while simultaneously controlling for numerical noise and integration errors.[91]

To extract the circular dichroism spectra, it is necessary to perturb Eq. (5.1) with a delta-pulse electric field along each real-space coordinate (e.g. x, y, z). Following Diedrich and Grimme,[121] we use the length gauge for the electric-dipole operator. For large basis sets, both the length and the velocity gauge representation of the electric-dipole operator approach each other.[98] Despite the fact that the length gauge is origin dependent, it has been found that the length gauge is more robust because it is less sensitive to the quality of the wave function. This modifies the Fock/Kohn-Sham matrix such that

$$\mathbf{K}_{\mathrm{E}}(t) = \mathbf{K}(t) + \sum_{q=x,y,z} \kappa(t) \langle r_q \rangle \tag{5.6}$$

where $\mathbf{K}_{\mathrm{E}}(t)$ is the time-dependent Fock/Kohn-Sham matrix containing the external electric field, $\kappa(t)$ is the field strength at time t, and $\langle r_q \rangle$ are the atomic-orbital based length-gauge dipole integrals along component q. Because time is discretized, the perturbation corresponds to a step function lineshape lasting for only the initial time-step of width Δt, e.g.

$$\kappa(t) = \begin{cases} \kappa_{\max}, & 0 < t < \Delta t, \\ 0, & else \end{cases} \tag{5.7}$$

We will now show how perturbing chiral systems with a delta electric-field pulse and observing the time evolution of its magnetic dipole may be used to extract the CD spectrum.

CD spectrum from RT-TDDFT electron dynamics

We will follow closely the notation of Barron.[112] The quantity of interest for circular dichroism spectroscopy is the isotropic rotatory strength for the transition between states $|n\rangle$ and $|j\rangle$, defined as

$$R_{jn} \equiv \mathrm{Tr}\left[\mathrm{Im}\left(\langle n|\boldsymbol{\mu}|j\rangle\langle j|\boldsymbol{m}|n\rangle\right)\right]. \tag{5.8}$$

$\boldsymbol{\mu}$ is the electric-dipole operator

$$\boldsymbol{\mu} = \sum_k \boldsymbol{r}_k \tag{5.9}$$

with $\boldsymbol{r}_k$ being the position operator for the k-th electron. $\boldsymbol{m}$ is the magnetic dipole operator, defined as

$$\boldsymbol{m} = \frac{-i}{2c}\sum_k (\boldsymbol{r}\times\boldsymbol{\nabla})_k \tag{5.10}$$

with c being the speed of light. To extract the rotatory strength from the RT-TDDFT electronic dynamics, consider the time evolution of the induced magnetic dipole moment. Within the dipole approximation, this is the response of the magnetic dipole to a perturbing electric-dipole field.

$$m_\alpha(\omega) = G_{\beta\alpha}(E_\beta)_0 - \frac{1}{\omega}G'_{\beta\alpha}(\dot{E}_\beta)_0 \tag{5.11}$$

Greek indices α and β denote Cartesian coordinates, and the Einstein summation convention is used. E is the external applied electric field, and the tensors G and G' that multiply the real radiation field components are the real dynamic electric-dipole–magnetic-dipole optical activity tensors. $G_{\beta\alpha}$ is the real part of the electric-dipole–magnetic-dipole optical activity tensor

$$G_{\beta\alpha}(\omega) = 2\sum_{j\neq n}\frac{\omega_{jn}}{\omega_{jn}^2-\omega^2}\mathrm{Re}\left(\langle n|\mu_\beta|j\rangle\langle j|m_\alpha|n\rangle\right) \tag{5.12}$$

whereas $G'_{\beta\alpha}$ is the imaginary part of the electric-dipole–magnetic-dipole optical activity tensor

$$G'_{\beta\alpha}(\omega) = -2\sum_{j\neq n}\frac{\omega}{\omega_{jn}^2-\omega^2}\mathrm{Im}\left(\langle n|\mu_\beta|j\rangle\langle j|m_\alpha|n\rangle\right) \tag{5.13}$$

Because the real optical activity tensor $G_{\beta\alpha}$ is a time-odd, odd-parity tensor, it will only be supported for systems that exhibit a degenerate ground state, such as odd-electron systems (e.g. Kramers doublet). Furthermore, a magnetic field (time-odd operator) is required to observe any coherent phenomena since Kramers pairs generate equal and opposing contributions in its absence. It plays an important role in magnetochiral phenomena as well as odd-electron chiral systems with large spin-orbit coupling.[112] We do not consider such systems here, and so the time evolution of the magnetic dipole reduces to

$$m_\alpha(\omega) = -\frac{1}{\omega}G'_{\beta\alpha}(\dot{E}_\beta)_0. \tag{5.14}$$

If we consider one Cartesian component of Eq. (5.8),

$$R_{jn}^{\beta\alpha} = \mathrm{Im}\left(\langle n|\mu_\beta|j\rangle\langle j|m_\alpha|n\rangle\right) \tag{5.15}$$

we rewrite Eq. (5.13) as

$$G'_{\beta\alpha}(\omega) = -2\sum_{j\neq n}\frac{\omega}{\omega_{jn}^2-\omega^2}R_{jn}^{\beta\alpha} \tag{5.16}$$

Given the expressions in Eq. (5.16) and Eq. (5.14), we will now show how to extract R_{jn} from the propagation of the real-time TDDFT equations. For a perturbing electric field we consider a pulse in the form of a Dirac delta distribution at time zero,

$$(E_\beta)_0 = \kappa_\beta\delta(t) \tag{5.17}$$

with κ the magnitude of the electric field. In the frequency domain its time derivative becomes

$$\int_{-\infty}^{\infty} dt \left[\frac{\partial}{\partial t}\left(\kappa_\beta \delta(t)\right)_0\right] e^{-i\omega t} = -i\omega\kappa_\beta. \tag{5.18}$$

Plugging into Eq. (5.14) and rearranging for $G'_{\beta\alpha}$ we have

$$G'_{\beta\alpha}(\omega) = \frac{-im_\alpha(\omega)}{\kappa_\beta} \tag{5.19}$$

R_{jn} is formally extracted from the residue of the response function G' at a pole ω_{jn}. To extract R_{jn} from the propagation of the RT-TDDFT equations, we must incorporate lifetimes — or a finite energy width — to our expression for $G'_{\beta\alpha}$. This is done by changing to complex energies. We make the substitution

$$\omega_{jn} \to \tilde{\omega}_{jn} = \omega_{jn} - \frac{1}{2} i\Gamma_j \tag{5.20}$$

where Γ_j is the lifetime of the $j-$th excited state. Eventually, we will explore the infinite-lifetime limit ($\Gamma_j \to 0$), but for now $G'_{\beta\alpha}$ evaluates to

$$G'_{\beta\alpha}(\omega) = -2\sum_{j\neq n} \frac{\omega}{\omega_{jn}^2 - \omega^2 - i\omega\Gamma_j - \frac{1}{4}\Gamma_j^2} R_{jn}^{\beta\alpha} \tag{5.21}$$

Near resonance, the above is approximated by

$$G'_{\beta\alpha}(\omega) \approx -2\sum_{j\neq n} \frac{(\omega_{jn}^2 - \omega^2) + i\omega\Gamma_j}{(\omega_{jn}^2 - \omega^2)^2 + \omega^2\Gamma_j^2} R_{jn}^{\beta\alpha}. \tag{5.22}$$

The imaginary part of the above equation, which corresponds to an absorption lineshape, becomes

$$\mathrm{Im}\left(G'_{\beta\alpha}(\omega)\right) = -2\sum_{j\neq n} \frac{\omega^2\Gamma_j}{\left(\omega_{jn}^2 - \omega^2\right)^2 + \omega^2\Gamma_j^2} R_{jn}^{\beta\alpha}. \tag{5.23}$$

The real part describes the dispersive lineshape, and the two lineshapes are related to each other via the Kramers-Kronig relations. Knowledge of the absorptive lineshape at all frequencies allows one to have total knowledge of the dispersive lineshape at all frequencies and vice versa. Here we consider the absorptive lineshape components, because this directly relates to ECD. If we desired to compute optical rotatory dispersion, we could continue with the real component instead via the same RT-TDDFT dynamics.

Now we set Γ_j to zero. For $\omega \geq 0$,

$$\lim_{\Gamma_j \to 0} \mathrm{Im}\left(G'_{\beta\alpha}(\omega)\right) = \lim_{\Gamma_j \to 0} -2 \sum_{j \neq n} \frac{\omega^2 \Gamma_j}{\left(\omega_{jn}^2 - \omega^2\right)^2 + \omega^2 \Gamma_j^2} R_{jn}^{\beta\alpha} \tag{5.24}$$

$$= -\pi \sum_{j \neq n} \delta(\omega - \omega_{jn}) R_{jn}^{\beta\alpha} \tag{5.25}$$

Finally, using Eq. (5.19)

$$\mathrm{Im}(G'_{\beta\alpha}) = \mathrm{Im}\left(\frac{-i m_\alpha(\omega)}{\kappa_\beta}\right) \tag{5.26}$$

$$= -\mathrm{Re}\left(\frac{m_\alpha(\omega)}{\kappa_\beta}\right) \tag{5.27}$$

so equating Eq. (5.25) and Eq. (5.27) yields in the infinite-lifetime approximation

$$\sum_{j \neq n} \delta(\omega - \omega_{jn}) R_{jn}^{\beta\alpha} = \frac{1}{\pi} \mathrm{Re} \frac{m_\alpha(\omega)}{\kappa_\beta} \tag{5.28}$$

We see that for an isotropic system perturbed by a delta electric-field pulse, the Fourier transform of the time-dependent magnetic dipole response is related to the rotatory strength of a given electronic transition. Considering the magnetic dipole response to independent delta pulse perturbations along the x, y, and z axes yield a quantity proportional to Eq. (5.8)

$$R(\omega) = \sum_{j \neq n} \delta(\omega - \omega_{jn}) R_{jn} = \mathrm{Tr}\left[\frac{1}{\pi} \mathrm{Re} \frac{m_\alpha(\omega)}{\kappa_\beta}\right] \tag{5.29}$$

This is our working equation. Integration of the rotatory strength function $R(\omega)$ over the frequency range of an isolated transition will yield the rotatory strength for that transition.

Note that although Eq. (5.29) does not have explicit electric-dipole terms on the right hand side, κ has units of ea_0/E_h, or electric dipole per unit energy. Thus the units for Eq. (5.29) are

$$\frac{e^2\hbar a_0}{2m_e c E_h} = 8.66 \times 10^{-40} \text{erg esu cm G}^{-1}\text{eV}^{-1} \tag{5.30}$$

when reporting rotatory strength in the conventional cgs units and considering frequencies in eV.

Results and Discussion

All calculations were carried out using a locally-modified version of the Gaussian program[100] using the PBEPBE[131,132]/6-311++G** level[133–135] of theory. After a geometry optimization of each molecule, the time-dependent equations were propagated for at least 100 fs using at least a 0.0012 fs time step. In all cases, energy was conserved throughout the propagation to within 10^{-8} hartree. The initial state was prepared using delta pulses with field strength of 0.0001 $E_h(ea_0)$. The real-time TDDFT computed spectra were artificially damped with an exponential function, leading to a line-shape with a full-width half-max (FWHM) value of 0.1 eV.

To test our implementation, we considered the two chiral molecules in Figure 5.1, 2,3-(*S*,*S*)-dimethyloxirane (DMO) and α-1,3-(*R*,*R*)-pinene. The computed rotatory strength is given in Figure 5.2 for DMO and for pinene. From these spectra it is clear that in the weak-field limit, the RT implementation gives essentially identical information about the ECD band spectra as does LR-TDDFT. In both figures, we compute the first 100 LR-TDDFT excited states of each molecule. In contrast to LR-TDDFT, the RT-TDDFT method can compute the entire band spectra for each molecule simultaneously. This makes the RT spectra advantageous to the LR methods, as LR would require the diagonalization of a rather large linear-response Hessian. However, for a few roots, LR-TDDFT will still be the method of

choice.

Despite this, problems involving computing ECD spectra with DFT remain. ECD is highly sensitive to geometry, basis, and the chosen density functional. For example, we overestimate the experimental magnitude of the 2A state of DMO predicting a rotatory strength of -12.0 cgs whereas the experimental value[136] is observed at -0.1 cgs. This is in line with similar-quality results reported by Diedrich and Grimme[121] using LR-TDDFT with triple-zeta basis sets and assorted DFT functionals. Our implementation of the RT-TDDFT cannot fix any problems associated with the LR-TDDFT method, as the two predict the same excited-state properties in the weak-field limit. However, for cases where DFT is expected to perform well, the RT-TDDFT method should provide a competitive alternative to standard LR-TDDFT when computing ECD spectra for high density of states systems. We also note that our implementation, like LR-TDDFT, is not gauge origin invariant. To resolve these issues, it is necessary to utilize gauge-including atomic orbitals (GIAOs)[137] or use the electric dipole in the velocity gauge, though this method is far more sensitive to the underlying wave function, as pointed out by Diedrich and Grimme.[121] It has been pointed out that although a GIAO implementation is ideal, because accurate computation of excited states and properties already requires larger basis sets, the problems introduced by gauge origin dependencies are diminished for large basis calculations. Comparing small basis set results to experiment is already suspect, regardless of gauge origin issues.[138] Alternatively, the working equation Eq. (5.29) can, with minimal modification, employ the dipole-velocity gauge formalism, which is gauge-origin invariant. However, a detailed investigation of gauge origin issues in TD-DFT is not within the scope of this work.

Conclusion

Here we have implemented an atomic-orbital based real-time density functional theory for the computation of electronic circular dichroism spectra. Because practical computation of the ECD spectra requires a high number of states to be computed, for large chiral molecules with a high density of states the RT-TDDFT will become computationally superior to the standard

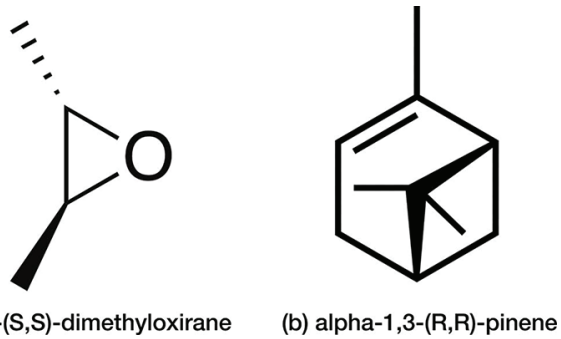

Figure 5.1: The chiral molecules considered in this study, (a) 2,3-(S,S)-dimethyloxirane (DMO) and, (b) α-1,3-(R,R)-pinene. They contain 166 and 332 basis functions, respectively.

linear-response TDDFT methods. Furthermore, because the method is atomic-orbital based, it is immune to several of the pitfalls that hinder the practical application of existing grid-based RT-TDDFT. We expect the AO-based RT-TDDFT will be advantageous for computing ECD spectra of large chiral molecules, such as biomolecules, with a high density of states.

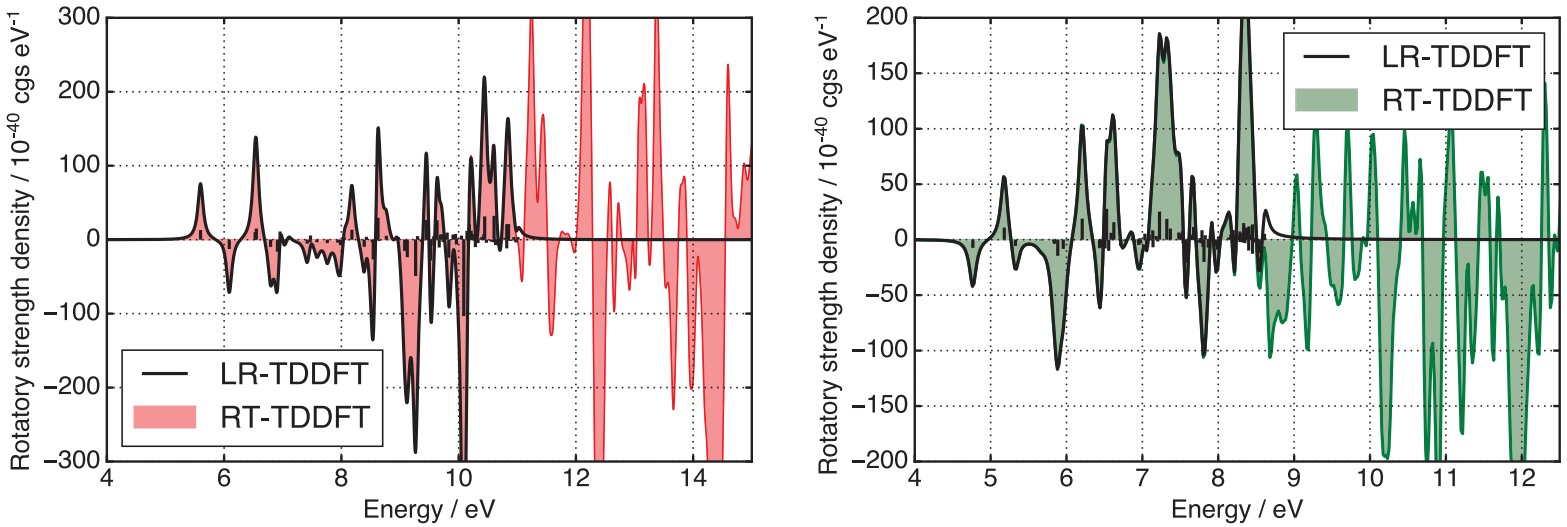

(a) 2,3-(S,S)-dimethyloxirane (DMO)

(b) α-1,3-(R,R)-pinene

Figure 5.2: Computed ECD spectrum of (a) 2,3-(S,S)-dimethyloxirane (DMO) and, (b) α-1,3-(R,R)-pinene at PBEPBE/6-311+G**. The vertical lines correspond to analogous LR-TDDFT results for the first 100 states. An artificial Lorentzian damping was applied to give the RT-TDDFT peaks a line width of 0.1 eV. Lorentzian functions were added to the LR-TDDFT stick spectra, and the RT-TDDFT and LR-TDDFT lineshapes exactly coincide. Thus in the weak-field limit, LR and RT-TDDFT methods give essentially the same results, though RT-TDDFT computes the whole ECD band spectrum.

Chapter 6

CAN QUANTIZED VIBRATIONAL EFFECTS BE OBTAINED FROM EHRENFEST MIXED QUANTUM-CLASSICAL DYNAMICS?

In this chapter, we explore the question of whether mean field, or "Ehrenfest" mixed quantum-classical dynamics is capable of capturing the quantized vibrational features in photo-absorption spectra that result from infrared- and Raman-active vibrational transitions. We show that vibrational and electronic absorption spectra can indeed be obtained together within a single Ehrenfest simulation. Furthermore, the electronic transitions show new sidebands that are absent in electronic dynamics simulations with fixed nuclei. Inspection of the electronic sidebands reveals that the spacing corresponds to vibrational frequencies of totally-symmetric vibrational modes of the ground electronic state. A simple derivation of the time-evolving dipole in the presence of external fields and vibrational motion show the origin of these features, demonstrating that mixed quantum-classical Ehrenfest dynamics is capable of producing infrared, Raman, and electronic absorption spectra from a single simulation. The work in this chapter is adapted with permission from Joshua J. Goings, David B. Lingerfelt, and Xiaosong Li. Can quantized vibrational effects be obtained from ehrenfest mixed quantum-classical dynamics? *J. Phys. Chem. Lett.*, 7:5193–5197, 2016.

Introduction

Real-time propagation of the time-dependent self-consistent field equations (RT-TDSCF) is routinely applied to computing various spectroscopic properties of molecular systems.[11,91,92,97,139–141] For example, RT-TDSCF has been applied to absorption spectroscopy,[92]

circular dichroism spectroscopy,[142] excited-state absorption,[143] as well as the computation of nonlinear optical properties.[144] Recently, it has even been extended to relativistic Hamiltonians in the four- and two-component methodologies.[1,11,13,14] Fundamentally, however, nuclei are stationary ("frozen") in the RT-TDSCF approach. Because many spectroscopically relevant processes occur on time scales orders of magnitude faster than vibrational motion, this is often a good approximation.

The *ab initio* Ehrenfest mixed quantum-classical dynamics method[1,96,145–152] extends the RT-TDSCF picture to include classical nuclear motion in a mean-field manner. The electronic motion is governed by the RT-TDSCF equations, which is fully quantum, and this in turn exerts forces on the classical nuclei which determines their dynamics along a potential energy surface. Because the governing electronic state in the Born-Oppenheimer picture is a *superposition* of electronic energy eigenstates, the electronic forces on the nuclei are considered to be an average mean-field potential — that is to say, the nuclei move according to the weighted average of several electronic states' energy gradients.

In RT-TDSCF, absorption spectra are routinely obtained by applying a weak perturbing field, and monitoring the time evolution of some given observable. For the case of absorption spectroscopy, the perturbing field is often a weak electric pulse. Elements of the frequency-dependent polarizability tensor, which determine the dipole-strength function and absorption lineshape, are extracted from the electronic dynamics via Fourier transformation of the time-dependent dipole. Such perturb-then-propagate protocols have been detailed elsewhere in this work, notably in Chapters 4 and 5, and we also refer interested readers to the relevant literature.[14,91,92,142,153,154]

One interesting question is whether or not extending the aforementioned protocol for absorption spectroscopy to Ehrenfest dynamics yields any new or useful information. In other words, if we perturb a slightly geometrically distorted molecule with a weak electric field, will propagating the nuclear positions classically according to the Ehrenfest potential be sufficient to capture vibrational transitions in the resultant absorption spectrum?

Currently, vibrationally resolved absorption spectra are most commonly produced by a

time-independent framework in which the electronic and vibrational energy eigenstates are found, and all transition moment integrals between them are evaluated.[149,155–158] However, the photo-absorption cross-section can also be evaluated from the time correlation functions of certain observables.[159] Time correlation function-based formalisms underlie the widely-applied dynamical theories of spectral line-shapes for chemical systems, which either demand knowledge of the vibrational dynamics of the system in each electronic state,[160,161] or assume that the relevant observables fluctuate randomly with a well-defined distribution.[162,163] However, these correlation function-based theories are couched in a perturbative treatment of the rate at which the system absorbs energy from the incident field, leading to expressions for the photo-absorption cross-section which depend solely on the field-free dynamics. That is, the absorption line-shape function carries no explicit dependence on the applied field, preventing any description of vibrational effects on important higher-order optical processes. A more general approach to the absorption lineshape is provided through the frequency-dependent molecular polarizability. Identifying the origins of resonances that contribute to its pole structure will help answer the question of which spectral features can be captured using the Ehrenfest approach.

Theory

Consider the time-dependent electric dipole $\boldsymbol{\mu}(t)$ of a system evolving under the influence of a weak electric field (e.g. linear-response) and undergoing motion along some normal mode coordinate R. In the case where R is stationary, the time-dependent dipole is given as

$$\boldsymbol{\mu}(t) = \boldsymbol{\mu}(0) + (\boldsymbol{\alpha} * \boldsymbol{E})(t) \tag{6.1}$$

where $\mu(0)$ is the dipole moment for the reference state (e.g. the ground state) at the (field-free) equilibrium geometry, $\boldsymbol{\alpha}(t)$ is the time-dependent polarizability and $\boldsymbol{E}(t)$ is the time-dependent external electric (dipole) field. In the above equation, $(\boldsymbol{\alpha} * \boldsymbol{E})(t)$ is the convolution of the time-dependent polarizability and the applied field. The Cartesian

components of time-dependent polarizability tensor can be written as a sum over electronic states

$$\alpha_{ij}(t) = \Theta(t) \sum_{n(\neq 0)} \langle 0|\hat{\mu}_i|n\rangle\langle n|\hat{\mu}_j|0\rangle \sin(\omega_{0n}t) \tag{6.2}$$

where $\Theta(t)$ is the Heaviside step function and ensures causality of the response. The system has electronic resonances at frequencies ω_{0n} with magnitudes governed by the absolute squared transition dipole, $|\langle 0|\hat{\mu}_i|n\rangle|^2$.

Assuming an impulse electric field is applied along Cartesian direction j with intensity E_j, the i component response of Eq. (6.1) can be rewritten as

$$\mu_i(t) = \mu_i(0) + \alpha_{ij}(t) \cdot E_j \tag{6.3}$$

If we expand Eq. (6.3) in terms of displacements of R about its equilibrium value, R_0, to first order we have

$$\mu_i(t) = \mu_i(0) + \alpha_{ij}(t) \cdot E_j + \frac{\partial \mu_i(0)}{\partial R}(R - R_0) + \frac{\partial \alpha_{ij}(t)}{\partial R} E_j (R - R_0) + \cdots \tag{6.4}$$

Here, R is parameterized by t, though we leave the explicit t dependence out for clarity. We can replace the $R - R_0 \rightarrow \Delta R \cos(\omega_N t)$ by making the observation that for small displacements from R_0, the normal-mode coordinate will evolve nearly harmonically with a maximum displacement ΔR. Making this substitution and moving $\boldsymbol{\mu}_0$ to the left gives

$$\mu_i(t) - \mu_i(0) = \Delta\mu_i(t) = \alpha_{ij}(t) \cdot E_j + \frac{\partial \mu_i(0)}{\partial R}[\Delta R \cdot \cos(\omega_N t)] + \frac{\partial \alpha_{ij}(t)}{\partial R} E_j [\Delta R \cdot \cos(\omega_N t)] + \cdots \tag{6.5}$$

Taking the Fourier transform of the above Eq. (6.5) and assuming positive frequencies,

we have

$$\begin{aligned}\Delta\mu_i(\omega) \propto E_j \cdot \sum_{n(\neq 0)} [\langle 0|\hat{\mu}_i|n\rangle\langle n|\hat{\mu}_j|0\rangle]\delta(\omega_{0n} - \omega) \\ + \Delta R \cdot \frac{\partial \mu_i(0)}{\partial R}\delta(\omega - \omega_N) \\ + \Delta R \cdot E_j \cdot \sum_{n(\neq 0)} \frac{\partial}{\partial R}[\langle 0|\hat{\mu}_i|n\rangle\langle n|\hat{\mu}_j|0\rangle]\delta(\omega_{0n} \pm \omega_N - \omega) + \cdots \end{aligned} \tag{6.6}$$

From this we can see that the first term corresponds to pure electronic transitions at the equilibrium geometry, which are routinely obtained in frozen-nuclei RT-TDSCF. The second term accounts for spectral features arising from the ground-state dipole moment changing with respect to vibration along a normal mode. These are the infrared (IR) allowed transitions corresponding to vibrational frequency ω_N, and are analogous to the treatment of IR spectra in classical molecular dynamics. Finally, the last term gives how the polarizability changes with respect to vibration along a normal mode. These are the so-called Herzberg-Teller terms in the vibronic theory of resonance Raman intensities, and account for the Raman-allowed transitions resulting from coupling between electron transitions and vibrational motion. Accordingly, they take a very similar form to the "B" term in Albrecht's seminal work on Raman intensities.[164–166] Unlike Raman spectroscopy, the Ehrenfest protocol is energy conserving, so it does not permit de-excitations, and the Raman transitions appear only as sidebands of the electronic transitions. Although we have neglected higher-order terms in the above derivation, it is easy to extend the above procedure to higher orders in ΔR and obtain classical combination and overtone bands. In the *ab initio* simulations, though, the response of the dipole moment to all orders in the vibrational displacements (i.e. beyond the Herzberg-Teller term) and impulsive field strength are captured explicitly, so contributions to the spectral lineshape arising from these higher order terms are resolved with no added complexity, in contrast to the time-independent approaches.

Methods

In order to illustrate the contributions of nuclear motion to the Ehrenfest description of electronic sidebands, we first consider two simple systems, H_2 and D_2 at the RT-TDHF/STO-3G level of theory. All calculations were performed using the development version of the Gaussian electronic structure software.[100] After distorting the geometry slightly (*vide infra*) we perturb with a weak delta electric field corresponding to a strength of 0.0001 $E_h/(ea_0)$ polarized along the bond axis (z-component). This field is sufficiently weak so as to keep the Ehrenfest potential effectively in the ground state, and we cannot find any evidence of strong state mixing in the dynamics, evidenced by ω_N remaining in the ground-state vibrational mode. The Ehrenfest equations of motion were integrated with electronic and nuclear time steps of 0.0012 fs and 0.0036 fs. These are relatively short time steps, chosen to ensure the smooth co-evolution of electrons and nuclei. Simulations were run for 50 fs and the z-component of the time-dependent dipole moment was Fourier transformed using the Padé approximant scheme[104] which gives high-resolution spectral data with relatively short simulation times. This Fourier transform is proportional to the dipole strength function for isotropic samples. Here we plot only the magnitude of the real component of the frequency-multiplied Fourier transform, which corresponds to absorptive line-shapes. The imaginary component has the same pole and intensity information, but the line-shape is dispersive. The two contain identical information and are related *via* the Kramers-Kronig relations.[112] Though the 50 fs simulation time may appear small, it is more than sufficient to capture vibrational effects when used with the Padé approximant Fourier transform scheme. We have investigated longer time behavior of the systems (out to 300 fs, data not shown) and cannot detect any noticeable change in the resulting absorption spectrum.

Results

For the minimal-basis RHF/STO-3G H_2 and D_2, the systems have one intense electronic transition at $\hbar\omega_{0n} = 26.21$ eV at an equilibrium bond length of 0.7122 Å. H_2 has one

vibrational mode $\hbar\omega_N = 0.69$ eV while D_2 has its $\hbar\omega_N = 0.48$ eV, which are related by a factor of $\sqrt{2}$ on account of the higher mass of deuterium. Starting with the nuclei at a slightly compressed initial bond length (0.7100 Å) for each system and then perturbing with the weak delta-like pulse, the electronic and vibrational dynamics were allowed to co-evolve within the *ab initio* Ehrenfest method.[91] The obtained optical absorption spectra are given in Fig. 6.1. Here, we can clearly see that both systems have a strong pure electronic absorption at 26.21 eV. However, over the course of the dynamics, the vibrational-frequency modulated electric dipole moment gives rise to very different line-shapes. From merely allowing the nuclear positions of these isotopologues to evolve classically, the vibrational nature of the sidebands is revealed through their spacings, which are related to each other by a factor of $\sqrt{2}$; a clear isotopic effect. Although not shown, there is no transition in the infrared region, which is to be expected as H_2 and D_2 have no ground-state dipole moment and direct photo-excitation of the stretch mode is not dipole-allowed. However, the stretch mode is Raman-active, so we observe the Raman sidebands around the electronic transition.

Next we explore the temperature dependence of the vibrationally-resolved spectra from the Ehrenfest-based approach. We again test minimal-basis H_2 at the RT-TDHF/STO-3G level of theory starting with stationary increasingly compressed initial bond lengths to increase the vibrational energy. This corresponds to an increase in ensemble temperature, which can be calculated using elementary Boltzmann statistics. The computed absorption spectra are given in Fig. 6.2. The change in ΔR of the bond, associated with an increase in temperature, clearly raises the intensity of the sidebands, as is expected via the ΔR dependence in Eq. (6.6).

Finally, we show a slightly more realistic system with a non-zero ground-state dipole moment, CO at RT-TDHF/6-31+G*, to illustrate how, in one shot, the Ehrenfest approach obtains both electronic excited-state information as well as ground state vibrational information. The bond length was compressed by 0.01 Å from the optimized ground-state geometry of 1.1133 Å to 1.1033 Å. The simulated spectrum is given in Fig. 6.3. We can see a fairly strong IR peak at 0.30 eV, which corresponds to the CO stretch obtained from an optimization and frequency calculation on the same system. Furthermore, we see the first overtone at

0.60 eV, with a far smaller intensity due to the $(\Delta R)^2$ dependence. Though the overtones appear similar to those from a quantum treatment of the nuclei, we could not find evidence of quantum anharmonic corrections to these peaks, so it appears these overtones are due to the classical treatment of the nuclei. If they were due to a quantum treatment of the nuclei, we would not expect the overtones to be integer multiples of the fundamental frequency, which is what we observe. All of the intense electronic transitions further up in energy display sidebands separated by the 0.30 eV vibrational energy. Because CO is of the point group $C_{\infty v}$, the CO stretch is both IR and Raman active.

Conclusion

Here we have shown that extending the traditional RT-TDSCF approach to computing absorption spectra to include vibrational motion in the mixed quantum-classical Ehrenfest approach does in fact encode the effects of vibrational transitions into the electronic absorption spectrum, evidenced through isotopic effects and dependence on geometric displacement. In contrast to classical MD simulations, here we have shown that the Ehrenfest mixed quantum-classical dynamics captures vibrational effects on electronic absorption spectra. In particular we see Raman sidebands corresponding to Herzberg-Teller terms which is a strictly quantum vibrational effect. This extends the utility of the Ehrenfest approximation to new classes of spectroscopic phenomena inaccessible to classical MD simulations, and opens up new avenues of interesting research with mixed quantum classical approaches.

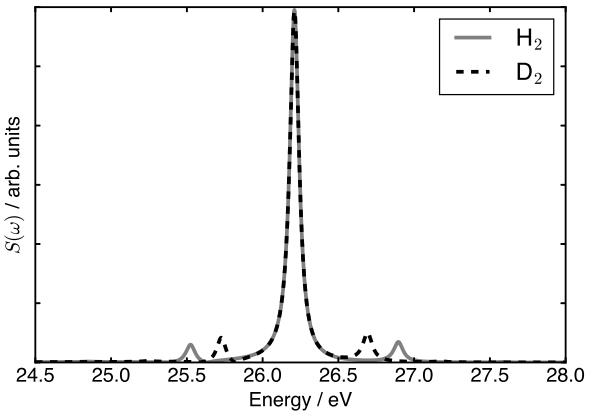

Figure 6.1: Computed optical absorption spectra of H_2 and D_2 using the Ehrenfest dynamics approach at the RT-TDHF/STO-3G level of theory. Each molecule was displaced from its equilibrium bond length of $R = 0.7122$ Å to a slightly shorter bond length of $R = 0.7100$ Å (maximum displacement of 0.0022 Å). Theoretically, D_2 sidebands should be $\sqrt{1/2}$ eV less than those of H_2, which is observed here. $\hbar\omega_N^{H_2} = 0.69$ eV and $\hbar\omega_N^{D_2} = 0.48$. Because displacement is small, the intensity of the central peak and sidebands is dominated by the first order terms. Thus, it is possible to see $\omega_e \pm 2\omega_N$ sidebands, though they are vanishingly small.

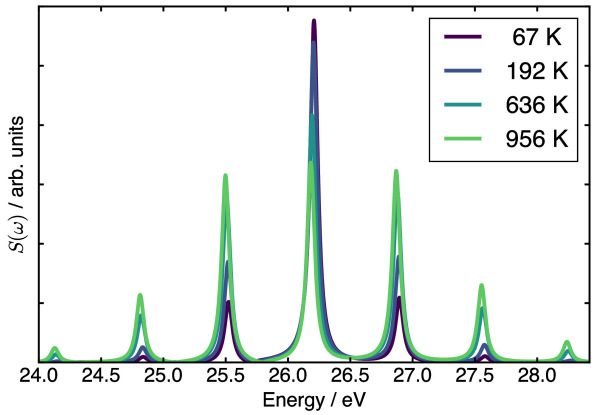

Figure 6.2: Computed optical absorption spectra of several stretched H_2 using the Ehrenfest dynamics approach at the RT-TDHF/STO-3G level of theory. Each molecule was displaced from its equilibrium bond length of $R = 0.7122$ Å to shorter bond lengths. Compression of the bond lengths corresponds to the addition of bond energy, which is reflected in temperature labels which are computed using Boltzmann statistics. Increasing temperature increases the intensity of the Raman sidebands, as we would expect from the ΔR dependence in the energy expression. Equivalently, this shows that higher ground vibrational states are more populated at higher temperature.

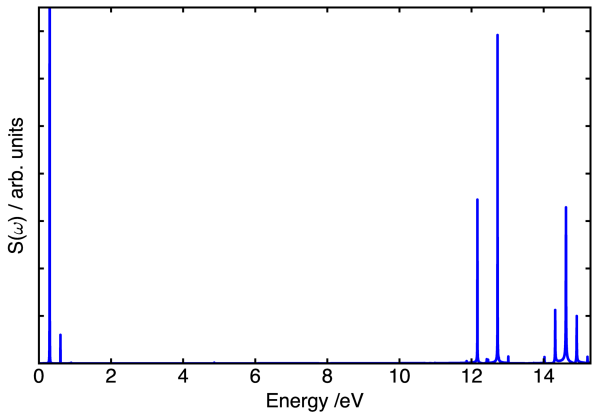

Figure 6.3: Computed optical absorption spectra of CO using the Ehrenfest dynamics approach at the RT-TDHF/6-31+G* level of theory. Here we perturb along the bond axis z so only z-allowed dipole transitions are shown. Furthermore, the bond is stretched from equilibrium by 0.01 Å. The CO stretch is visible at 0.30 eV, and a slight first overtone is visible at 0.60 eV. The higher-energy Raman transitions have sidebands separated by the ground-state CO stretch energy of 0.30 eV.

Chapter 7

ASSESSMENT OF LOW-SCALING APPROXIMATIONS TO THE EQUATION-OF-MOTION COUPLED-CLUSTER SINGLES AND DOUBLES EQUATIONS

Methods for fast and reliable computation of electronic excitation energies are in short supply, and little is known about their systematic performance. This work reports a comparison of several low-scaling approximations to the EOM–CCSD and LR–CCSD equations with other single-reference methods for computing the vertical electronic transition energies of eleven small organic molecules. The methods, including EOM–MPBT2 and its partitioned variant, are compared to several valence and Rydberg singlet states. We find that the EOM–MBPT2 method was rarely more than a tenth of an eV from EOM–CCSD calculated energies, yet demonstrates a performance gain of twenty-three percent. The partitioned equation-of-motion approach, P–EOM–MBPT2, which is an order of magnitude faster than EOM–CCSD, outperforms the CIS(D) and CC2 in the description of Rydberg states. CC2, on the other hand, excels at describing valence states where P–EOM–MBPT2 does not. The difference between the CC2 and P–EOM–MBPT2 can ultimately be traced back to how each method approximates EOM–CCSD and LR–CCSD. The results suggest that CC2 and P–EOM–MBPT2 are complementary: CC2 is best suited for the description of valence states while P–EOM–MBPT2 proves to be a superior $\mathcal{O}(N^5)$ method for the description of Rydberg states. The work in this chapter was adapted with permission from Joshua J. Goings, Marco Caricato, Michael J. Frisch, and Xiaosong Li. Assessment of low-scaling approximations to the equation-of-motion coupled-cluster singles and doubles equations. *J. Chem. Phys.*, 141(16):164116, 2014.

Introduction

Accurate and efficient methods for calculating excited-state energies are few and far between. On the one hand, linear-response time-dependent Hartree-Fock (LR–TDHF, also known as RPA) and time-dependent density functional theory (LR–TDDFT)[167–169] are fast methods for calculating excited-state energies, fast enough that they may be applied to large systems (> 1000 basis functions) routinely, yet are plagued by many problems that affect their accuracy. LR–TDDFT, for example, often underestimates excitation energies of charge-transfer states,[168] fails to describe excitations containing multi-electron character, and generally fails to describe the effects of dispersion. Attempts have been made to correct these features of LR–TDDFT,[170–172] often with some success, but it is clear that a reliable black-box method for calculating excitation energies must look beyond the HF/DFT regime.

Methods based on the highly successful coupled-cluster formalism (for two excellent reviews of coupled-cluster theory, see the review by Crawford and Schaefer[173] and the book by Shavitt and Bartlett[174]), on the other hand, can provide extremely accurate excitation energies for even the most difficult systems. The first application of coupled-cluster theory to electronic excited states was based on the response formalism, and is known as linear-response coupled-cluster (LR–CC).[175–179] This was followed by the equation-of-motion coupled-cluster formalism (EOM–CC),[180] as well as symmetry adapted cluster configuration interaction (SAC-CI).[181] Despite their formal differences, LR–CC and EOM–CC, when truncated at the same level of cluster operator, will give the same value for excitation energies, although they differ with respect to transition properties.[179] In particular, the EOM–CC formalism[182,183] has led to extremely accurate and robust descriptions of excited states, yet may be prohibitively costly. The equation-of-motion coupled-cluster singles and doubles (EOM–CCSD)[180,184] gives qualitatively and quantitatively accurate energies for most molecular systems, yet scales as $\mathcal{O}(N^6)$, making its application to large molecules difficult.

Methods that bridge the gap between the robust and highly accurate LR–CC and EOM–CC methods and the efficient but often-inaccurate LR–TDHF/LR–TDDFT are important

for the quantitative study of electronic excitations in large systems. Methods that have been proposed to balance cost and accuracy are the iterative-hybrid CC2,[185] the CIS(D) family of perturbative corrections to the configuration interaction singles method,[186] and perturbative approximations to the EOM–CCSD,[187,188] known as EOM–MBPT2. Most of these approximate methods can be formulated as $\mathcal{O}(N^5)$ methods, yet little is known about their systematic performance. Theoretically, CC2 and EOM–MBPT2 make very different assumptions regarding the relative importance of the coupled-cluster operators. CC2, originally developed within the response theory formalism, was designed to retain maximal flexibility with respect to orbital rotations, which are known to be important when computing molecular properties. However, CC2 does so at the cost of neglecting much dynamic electron correlation, by removing many of the doubles cluster operators. EOM–MBPT2, in contrast, has no flexibility with respect to orbital rotation, but seeks to maximize inclusion of dynamic correlation through the use of the MP2 cluster operator. The contrast between these approximations has strong implications when selecting a method for studying electronic excited states.

Here we investigate the implications of these approximations on a series of experimentally well-studied organic molecules. In particular, we find a striking difference between the methods in their ability to describe Rydberg and valence states. The results of our investigation provide critical information to aid in the choice of a cost-effective method for studying electronic excited states.

Theory

In the present work we adopt the notation that indices i, j, k, l refer to occupied orbitals, a, b, c, d refer to virtual orbitals, and p, q, r, s refer to any orbital. We also adopt Einstein summation, where the summation over common indices is implied. In coupled-cluster theory, the Schrödinger equation is parametrized by the exponential form of excitation operators $\hat{T}$, such that

$$\hat{H}e^{\hat{T}}|\Phi_0\rangle = Ee^{\hat{T}}|\Phi_0\rangle \tag{7.1}$$

The operator $\hat{T}$ is an excitation operator that has the effect of generating excited determinants from the reference state $|\Phi_0\rangle$. It takes the form

$$\hat{T} = \hat{T}_1 + \hat{T}_2 + \cdots = t_i^a a_a^\dagger a_i + t_{ij}^{ab} a_a^\dagger a_b^\dagger a_j a_i + \cdots \tag{7.2}$$

It is convenient to use the normal-ordered (relative to the Fermi vacuum) Hamiltonian $\hat{H}_N$, which is the Hamiltonian operator minus its reference expectation value

$$\hat{H}_N = f_{pq}\{a_p^\dagger a_q\} + \frac{1}{4}\langle pq||rs\rangle\{a_p^\dagger a_q^\dagger a_s a_r\} \tag{7.3}$$

or simply

$$\hat{H}_N = \hat{F}_N + \hat{V}_N \tag{7.4}$$

For the EOM–CCSD working equations, one must solve for the eigenvalues and eigenvectors of the following Hamiltonian matrix

$$\begin{bmatrix} \langle \Phi_i^a | \bar{H}_N | \Phi_k^c \rangle & \langle \Phi_i^a | \bar{H}_N | \Phi_{kl}^{cd} \rangle \\ \langle \Phi_{ij}^{ab} | \bar{H}_N | \Phi_k^c \rangle & \langle \Phi_{ij}^{ab} | \bar{H}_N | \Phi_{kl}^{cd} \rangle \end{bmatrix} \tag{7.5}$$

where $\bar{H}_N = e^{(-\hat{T}_1 - \hat{T}_2)} \hat{H}_N e^{(\hat{T}_1 + \hat{T}_2)}$, and $|\Phi_k^c\rangle, |\Phi_{kl}^{cd}\rangle$ are singly and doubly excited determinants, respectively. The eigenvalues of the Hamiltonian correspond to excitation energies out of the coupled-cluster ground state. Because of the similarity transformation, the matrix problem is non-Hermitian. The excited kets are generated by the linear operator $\hat{R}$, and the excited bras are generated by the linear operator $\hat{L}$.

$$\hat{R} = \hat{R}_1 + \hat{R}_2 + \cdots = r_i^a a_a^\dagger a_i + r_{ij}^{ab} a_a^\dagger a_b^\dagger a_j a_i + \cdots \tag{7.6}$$

$$\hat{L} = \hat{L}_1 + \hat{L}_2 + \cdots = l_a^i a_i^\dagger a_a + l_{ab}^{ij} a_i^\dagger a_j^\dagger a_b a_a + \cdots \tag{7.7}$$

Thus the EOM–CCSD Hamiltonian looks,[180] with respect to a suitable reference state $|\Phi_0\rangle$ and truncated to $\hat{R}_1$ and $\hat{R}_2$ (and likewise for $\hat{L}$):

$$\begin{bmatrix} \langle\Phi_0|\hat{L}_1\bar{H}_N\hat{R}_1|\Phi_0\rangle & \langle\Phi_0|\hat{L}_1\bar{H}_N\hat{R}_2|\Phi_0\rangle \\ \langle\Phi_0|\hat{L}_2\bar{H}_N\hat{R}_1|\Phi_0\rangle & \langle\Phi_0|\hat{L}_2\bar{H}_N\hat{R}_2|\Phi_0\rangle \end{bmatrix} \tag{7.8}$$

In general, $\hat{R}^\dagger \neq \hat{L}$ and vice versa, and a full solution to the EOM–CCSD equations requires solutions to both the $\hat{R}$ and $\hat{L}$ amplitudes. However, if only excitation energies are desired, one may solve for only $\hat{R}$ or $\hat{L}$ amplitudes. In the case of this work, we only concern ourselves with excitation energies, and solve for the $\hat{R}$ amplitudes only, which is to say we solve the connected right-hand side:

$$\left(\bar{H}_N\hat{R}\right)_c|\Phi_0\rangle = \omega\hat{R}|\Phi_0\rangle \tag{7.9}$$

where ω are the excitation energies. Therefore, the matrix equations we wish to solve are

$$\begin{bmatrix} \bar{H}_{SS} & \bar{H}_{SD} \\ \bar{H}_{DS} & \bar{H}_{DD} \end{bmatrix} \begin{bmatrix} R_1 \\ R_2 \end{bmatrix} = \omega \begin{bmatrix} R_1 \\ R_2 \end{bmatrix} \tag{7.10}$$

where $\bar{H}_{SS} = \langle\psi_i^a|\bar{H}_N|\psi_k^c\rangle$, that is to say the singles-singles block of the Hamiltonian matrix, and so on. The working equations may then be solved using non-Hermitian variants of the Davidson algorithm.[189–192]

When excitation energies are the subject of interest, the EOM–CC equation is equivalent to the Jacobian in the LR–CC formalism[178] for excitation energy calculations. The mathematical difference between LR and EOM formalisms arises when they are used to compute excitation properties, such as transition dipole and oscillator strengths. Jørgensen and co-workers have shown that the transition moment in LR–CC is size-intensive whereas EOM formalism is not,[179] although the difference in intensity between LR and EOM is very small for most computationally tractable systems.[193] In this work, we focus only on analyzing the performance of low-scaling alternatives to EOM–CCSD and LR–CCSD on excitation energies where these

two formalisms are equivalent.

EOM–MBPT2

One of the first approximations that can be made to the EOM–CCSD Hamiltonian is to utilize the perturbation expansion technique, and keep only the terms through second order (see Appendix D for derivations). As a result, $\hat{T}_1$ vanishes and only the first order $\hat{T}_2^{(1)}$ remains in the EOM equations,

$$\hat{T}_1 \rightarrow t_i^a = 0; \qquad \hat{T}_2^{(1)} \rightarrow t_{ij}^{ab(1)} = \frac{\langle ij||ab\rangle}{\epsilon_i + \epsilon_j - \epsilon_a - \epsilon_b} \tag{7.11}$$

This second-order perturbation approximation gives rise to the EOM–MBPT2 equation,

$$\begin{bmatrix} \bar{H}_{SS}^{(2)} & \bar{H}_{SD}^{(2)} \\ \bar{H}_{DS}^{(2)} & \bar{H}_{DD}^{(2)} \end{bmatrix} \begin{bmatrix} R_1 \\ R_2 \end{bmatrix} = \omega \begin{bmatrix} R_1 \\ R_2 \end{bmatrix} \tag{7.12}$$

nhere $\bar{H}_{SS}^{(2)}$ is the singles-singles block of the Hamiltonian through second order, and so on. A full derivation and the working equations are given in Appendix D. This approach was first derived by Stanton and Gauss,[187] and termed EOM–CCSD(2). Further work, and the development of the partitioned approach (detailed later) was derived by Gwaltney, Nooijen and Bartlett[188,194] and termed EOM–MBPT2. Both methods are equivalent. Because the EOM–MBPT2 Hamiltonian neglects contributions from the single-excitation cluster operators, as well as uses the MP2 double-excitation amplitudes, it can be understood as an excited-state calculation of roughly MP2 quality. The neglect of the $\hat{T}_1$ operators neglects orbital relaxation in response to the addition of electron correlation through the $\hat{T}_2$ operator. The EOM–MBPT2 Hamiltonian still contains terms that scale computationally as $\mathcal{O}(N^6)$, and there is no obvious benefit from the asymptotic scaling compared to a full EOM–CCSD calculation, however, the neglect of the numerous $\hat{T}_1$ terms greatly reduces the prefactor of the calculation. Furthermore, the $\hat{T}_2^{(1)}$ amplitudes are completely determined prior to

the excited-state calculation. In other words, no iterative ground-state calculation must be performed prior to solving the EOM equations, unlike the case for EOM–CCSD, where the CCSD ground-state wave function must be iteratively determined.

P–EOM–MBPT2

The problem with the second-order perturbative approach outlined above is primarily computational. Despite the advantage of not needing to perform a ground-state coupled-cluster calculation and reduction in terms computed, the leading order of scaling between EOM–CCSD and EOM–MBPT2 is identical with the latter having a smaller prefactor. Bartlett and coworkers[188,194] offered a solution around the scaling problem by using the so-called Löwdin partitioning approach.[195] The idea is to determine a perturbative series in $\hat{R}$ (or equivalently $\hat{L}$), in addition to the Rayleigh-Schrödinger perturbative approach to $\hat{T}$ above. The central idea is to partition the effective EOM–MBPT2 Hamiltonian into a principal space spanned by the single excitations ($\hat{R}_1$) and an orthogonal complement spanned by the double excitations ($\hat{R}_2$). A perturbative series is generated for the orthogonal complement. Truncation of this series, along with utilization of canonical orbitals, replaces the $\bar{H}_{DD}$ block with the diagonal

$$\bar{H}_{DD} \approx \bar{H}_{DD}^{(0)} = \epsilon_a + \epsilon_b - \epsilon_i - \epsilon_j \tag{7.13}$$

where ϵ_a is the orbital energy for the a-th orbital and so on. This is the zeroth-order effective Hamiltonian for the doubles-doubles block. The block matrix structure of the P–EOM–MBPT2 equations now has the form

$$\begin{bmatrix} \bar{H}_{SS}^{(2)} & \bar{H}_{SD}^{(2)} \\ \bar{H}_{DS}^{(2)} & \bar{H}_{DD}^{(0)} \end{bmatrix} \begin{bmatrix} R_1 \\ R_2 \end{bmatrix} = \omega \begin{bmatrix} R_1 \\ R_2 \end{bmatrix} \tag{7.14}$$

It turns out that all the iterative $\mathcal{O}(N^6)$ terms are contained in the doubles-doubles block for EOM–MBPT2, thus by replacing $\bar{H}_{DD}$ by its partitioned counterpart, P–EOM–MBPT2

becomes and iterative $\mathcal{O}(N^5)$ method. (The P–EOM–MBPT2 method does require the formation of some $\mathcal{O}(N^6)$ intermediates, but these must be formed once and is dwarfed by the later $\mathcal{O}(N^5)$ iterations.)

CIS(D)

The CIS(D) method can be seen as an approximation to P–EOM–MBPT2.[196] As pointed out by Head-Gordon,[197] the CIS(D) excited-state energy correction can be justified through a perturbation expansion of the excited-state CCSD equations, or what we refer to as the EOM–MBPT2 equations. This can be seen from considering the effective Hamiltonian

$$\begin{bmatrix} \bar{H}^{(2)}_{SS} & \bar{H}^{(1)}_{SD} \\ \bar{H}^{(1)}_{DS} & \bar{H}^{(0)}_{DD} \end{bmatrix} \begin{bmatrix} R_1 \\ R_2 \end{bmatrix} = \omega \begin{bmatrix} R_1 \\ R_2 \end{bmatrix} \tag{7.15}$$

Note that the off-diagonal blocks are approximated through first order. However, instead of solving the resulting matrix eigenvalue/eigenvector problem, the CIS(D) equations are formulated noniteratively by equating the R_1 amplitudes with the CIS amplitudes and then eliminating R_2. To see this, note that the effective Hamiltonian can be rewritten as two coupled equations

$$\bar{H}^{(2)}_{SS} R_1 + \bar{H}^{(1)}_{DS} R_2 = \omega R_1 \tag{7.16}$$

$$\bar{H}^{(1)}_{DS} R_1 + \bar{H}^{(0)}_{DD} R_2 = \omega R_2 \tag{7.17}$$

Rearranging the second equation to solve for R_2 ($\bar{H}^{(0)}_{DD}$ is diagonal, therefore invertible), and substituting this result into the first equation gives the CIS(D) electronic transition energy.

$$\omega_{CIS(D)} = \langle \psi_{CIS} | \bar{H}^{(2)}_N | \psi_{CIS} \rangle + \frac{\langle \psi_{CIS} | \bar{H}^{(1)}_N | \psi^{ab}_{ij} \rangle \langle \psi^{ab}_{ij} | \bar{H}^{(1)}_N | \psi_{CIS} \rangle}{\omega_{CIS} - (\epsilon_a + \epsilon_b - \epsilon_i - \epsilon_j)} \tag{7.18}$$

Thus CIS(D) can be thought of as a non-iterative $\mathcal{O}(N^5)$ approximation to P–EOM–MBPT2. CIS(D) retains the CIS exited state wave function, and can only correct for energy. Any transition properties, such as oscillator strength, will be identical to the CIS description.

CC2

The CC2 method for excited states, known as linear-response CC2 (LR–CC2),[185] is not based on the perturbative approaches in the other methods. CC2 was originally derived from standard response theory as a way of computing accurate molecular properties. To do so, it was noted that under an external perturbation the effective orbital rotation operators, $\hat{T}_1$, appear to zeroth order in the fluctuation potential and first order in the external perturbation.[198] Since $\hat{T}_2$ appears to second order in the energy and first order in the wave function, the singles, it was reasoned, must be more important for molecular properties. Thus no approximation to $\hat{T}_1$ is made in CC2.

Practically, CC2 is derived from the CC2 ground-state reference, which is a second-order approximation to CCSD in that the $\hat{T}_2$ operator is restricted to only connect to $\hat{F}$ when acted on by doubly excited bras. In other words, the CCSD equation to determine the $\hat{T}_2$ amplitudes changes from $\langle\psi_{ij}^{ab}|e^{-\hat{T}_1-\hat{T}_2}\hat{H}_N e^{\hat{T}_1+\hat{T}_2}|\psi_0\rangle = 0$ to $\langle\psi_{ij}^{ab}|e^{-\hat{T}_1}\hat{H}_N e^{\hat{T}_1} + e^{-\hat{T}_2}Fe^{\hat{T}_2}|\psi_0\rangle = 0$. Extending this idea to the linear-response formalism leads to the effective Jacobian block matrix for evaluating the excitation energies

$$\begin{bmatrix} \langle\psi_i^a|e^{-\hat{T}_1-\hat{T}_2}\hat{H}_N e^{\hat{T}_1+\hat{T}_2}|\psi_k^c\rangle & \langle\psi_i^a|e^{-\hat{T}_1-\hat{T}_2}\hat{H}_N e^{\hat{T}_1+\hat{T}_2}|\psi_{kl}^{cd}\rangle \\ \langle\psi_{ij}^{ab}|e^{-\hat{T}_1}\hat{H}_N e^{\hat{T}_1}|\psi_k^c\rangle & \langle\psi_{ij}^{ab}|e^{-\hat{T}_2}\hat{F}_N e^{\hat{T}_2}|\psi_{kl}^{cd}\rangle \end{bmatrix} \begin{bmatrix} R_1 \\ R_2 \end{bmatrix} = \omega \begin{bmatrix} R_1 \\ R_2 \end{bmatrix} \tag{7.19}$$

The solution scheme for the CC2 equations is similar to EOM–CCSD: a ground-state calculation is performed first to obtain optimized values for $\hat{T}_1$ and $\hat{T}_2$ amplitudes, followed by the iterative solution of the above effective Hamiltonian to solve for R (if only energies are desired). This is unlike the perturbative approaches, in which the $\hat{T}$ amplitudes are directly determined (and thus no ground-state calculation is required). As an approximation

to LR–CCSD, CC2 eliminates all of the highest-order scaling terms, thus making CC2 an $\mathcal{O}(N^5)$ method.

Results and Discussion

Both P–EOM–MBPT2 and CC2 are $\mathcal{O}(N^5)$ scaling wave function-based methods, although this computational scaling is obtained in a very different manner. Their parameter-free nature holds the potential for computing many-electron excited states with a well-balanced predictability. We test the quality of these low-scaling excited-state methods across a wide range of excitations (e.g. from valence to Rydberg excitations). After comparing each method's performance against experimental data, we rationalize our observations in light of the formal characteristics of each method. We hope this work will provide confidence and guidance to the utility of low-scaling approximations to LR–CCSD and EOM–CCSD methods.

As low-scaling wave function-based methods, P–EOM–MBPT2 and CC2 can be considered complementary excited-state methods to each other. Both methods have the same expression for the doubles-doubles block, but the rest of the blocks differ in their approximations. In particular, CC2 eliminates many of the connected $\hat{T}_2$ terms so that a majority of the terms depend on $\hat{T}_1$. In contrast, the P–EOM–MBPT2 methods eliminate all terms that have a contraction with $\hat{T}_1$, because $\hat{T}_1$ is zero, so that the majority of the terms are $\hat{T}_2$ dependent. In other words, one way to view the difference between CC2 and P–EOM–MBPT2 is that the former favors $\hat{T}_1$ (or is "$\hat{T}_1$ heavy") and the latter favors $\hat{T}_2$ ("$\hat{T}_2$ heavy"). The $\hat{T}_1$ operator has long been understood as accounting for orbital response to electron correlation and the $\hat{T}_2$ operators are understood as accounting for the dynamic (pairwise) electron correlation. Which contribution matters most to electronic excitation energies is an open question, and a comparison of CC2 with P–EOM–MBPT2 provides an excellent case study of the importance of each excitation operator. It should be noted that CC2 still retains some $\hat{T}_2$ contributions, as $\hat{T}_1$ depends on $\hat{T}_2$ (if $\hat{T}_2$ were zero, then $\hat{T}_1$ would necessarily be zero due to Brillouin theorem). However, CC2 eliminates all of the $\hat{T}_2$ terms in the doubly excited bra space, and

the effect of dynamic correlation in this space can only be incorporated indirectly through $\hat{T}_1$.

The EOM–MBPT2 and P–EOM–MBPT2 methods, along with CC2, have been implemented and tested in the development version of the Gaussian electronic structure theory suite.[199] The accuracy of these methods is tested against EOM–CCSD, LR–TDDFT/B3LYP, CIS(D), RPA, and CIS methods. The methods were tested using the Pople split-valence basis set 6-311(3+,3+)G**, where all atoms were augmented with three diffuse functions. This type of basis has been shown satisfactory for calculating excitation energies.[200–202] The molecules chosen for testing, given in Fig. 7.1, have been extensively studied in the gas phase, and reliable experimental data is available in the literature. 69 excited states in all were calculated and compared to experiment, and of the 69 states, 30 were considered valence states, and 39 are considered Rydberg states. In addition to experimental comparisons, direct comparisons between the low-scaling methods and EOM–CCSD were performed. Because each method can be seen as an approximation to EOM–CCSD, the CCSD excitation energies are a critical reference.

Due to the unreliability of experimental excited-state energies for triplets,[201] only comparisons to singlet excitations were studied. All excitation energies obtained are compared to experimental values, using the metric of mean absolute error to experiment (Mean AE), maximum absolute error to experiment (Maximum AE), and root mean square error to experiment (RMS). Geometries, which were optimized at the ground-state MP2/6-311+G** level of theory, were taken from the test set by Caricato, *et al.*[200] The values for LR–TDDFT/B3LYP, experimental values, and CIS/CIS(D)/RPA values are taken from those reported previously.[201]

While the assignment of excited states for the selected molecules has been detailed elsewhere,[201] and indeed the present work can be seen as an extension of Caricato, et al., we briefly explain our methodology here. Valence states may be identified by examining the dominant orbital contributions to the excitation. Rydberg states, which are more difficult to assign, were separated by irreducible representation, energy ordered, and then matched with experimental data. The results and assignments for each excitation are given in the Supporting Information. This methodology has also been applied successfully to the same molecules in

the work by Wiberg, et al.[202] Vibronic effects are not necessarily negligible, especially for the azabenzenes (in particular the symmetry forbidden $n \rightarrow \pi^*$). These transitions are broad and have low intensity, thus the experimental uncertainty is larger for these transitions. In spite of this, vibronic corrections are beyond the scope of this chapter and were not included. This will be the focus of later work.

Comparing first directly to EOM–CCSD in Tab. 7.1, we find that the EOM–MBPT2 approximation performs closely to EOM–CCSD with a mean absolute error of only 0.13 eV. However, because it has the same polynomial scaling cost, there is little practical advantage to its use. On the other hand, the $\mathcal{O}(N^5)$ P–EOM–MBPT2 gives EOM–CCSD quality results within 0.25 eV, followed by CIS(D) and CC2. In general, P–EOM–MBPT2 overestimates excitation energies relative to EOM–CCSD, whereas CC2 and CIS(D) underestimate excitation energies.

Of all the molecules tested in Fig. 7.1, EOM–CCSD provides excitation energies closest to those of experiment for all states considered in Tab. 7.4. It has a root-mean-square error (RMS) of 0.36 eV. EOM–MBPT2 generally has similar performance to EOM–CCSD, which suggests the relative importance of including the double-excitation subspace when calculating excited-state energies. Methods that do not include a double-excitation subspace, namely CIS and RPA, have a much poorer description of experimental excitations, with an RMS around 1.25 eV. The partitioned approach, P–EOM–MBPT2 contains much double-excitation character, though much less than EOM–CCSD or EOM–MBPT2, on account of the severe restrictions on the doubles-doubles block. LR–TDDFT/B3LYP performs modestly, with an RMS of 0.84 eV, which is far better than simple wave function-based methods like RPA and CIS. CIS(D) has performance similar to P–EOM–MBPT2 in general. CC2 performs quite well for all states, with an accuracy lying between the EOM–MBPT2 and P–EOM–MBPT2 methods.

It is perhaps more revealing, however, to note the differences in the estimation of valence states versus Rydberg states. It should be noted that all states considered are well under the CCSD ionization potential and therefore may be classified as valence or Rydberg. In

the direct comparisons to EOM–CCSD valence energies in Tab. 7.2, we find that CC2 gives EOM–CCSD quality results to 0.3 eV, versus P–EOM–MBPT2, which has errors of nearly 0.5 eV. Of all the $\mathcal{O}(N^5)$ methods, CIS(D) reproduces CCSD-quality results the best. For Rydberg states, the performance of the methods compared to EOM–CCSD is more stark. Both the EOM–MBPT2 and P–EOM–MBPT2 reproduce EOM–CCSD quality results to 0.07 eV, compared to CC2 and CIS(D), which reproduce the CCSD excitation energies to almost 0.5 eV. We suggest that this result stems from the necessity of including $\hat{T}_2$ amplitudes in the doubly excited manifolds of the effective Hamiltonian, which only the (P–)EOM–MBPT2 methods include compared to CIS(D) and CC2. This hypothesis will be discussed later.

Similar conclusions regarding the performance of the methods tested are reached when comparing to experimental data. For the valence states considered (Tab. 7.5), the wave function-based methods perform poorly compared to the Rydberg states (Tab. 7.6). Perhaps more surprisingly is how well B3LYP performs, with an RMS of 0.26 eV, compared to EOM–CCSD which has an RMS twice that at 0.52 eV. However, this may simply be the result of fortuitous cancellation of errors in B3LYP, especially in light of the varied performance of similar hybrid functionals on the same test set.[201] We also note that B3LYP was parameterized to perform well for organic molecules like many of the small molecules tested here. EOM–MBPT2 and P–EOM–MBPT2 perform much worse than EOM–CCSD or CC2 – consistently overestimating the valence state energies – and we suggest that much of the failure for valence states can be traced back to the total neglect of $\hat{T}_1$ amplitudes.

The single-excitation cluster operator has long been understood as an orbital rotation operator, which mixes virtual and occupied orbitals to account for orbital relaxation. Valence states are highly sensitive to the effects of orbital rotation and relaxation. The Thouless theorem[34] says that the effect of the $e^{\hat{T}_1}$ operator is to transform any single determinant into any other single determinant. It is well known that minimization of the energy of a single Slater determinant with respect to the rotation parameters (or t_i^a amplitudes), determines the stability conditions of the Hartree-Fock equations known as Brillouin's condition.[34] The Thouless theorem explains why CCSD and higher methods are so insensitive to reference

choice; optimal reference is generated through the $\hat{T}_1$ operator. Because the perturbative approximations considered neglect the effects of orbital rotation, we should expect them to perform much worse for valence states. CC2, which does account for orbital rotation and relaxation, performs quite well for the valence states, which is consistent with this hypothesis. In fact, for the valence states considered CC2 outperformed EOM–CCSD. We wish to note two benchmarking studies of coupled-cluster excited-state methods, the first by Schreiber, *et al.*,[203] and the recent extension by Kánnár and Szalay.[204] These studies — which only consider valence states — find that in comparison to CC3 and CASPT2 references, CCSD overestimates valence state energies, whereas the mean deviation for CC2 is near zero. Our results are in agreement with these findings.

Despite the success of CC2 in describing valence states, it is not nearly as robust in describing Rydberg states. Rydberg states are much more diffuse and less sensitive to orbital rotations. The heavy inclusion of the $e^{\hat{T}_2}$ operator in the perturbative EOM methods accounts for the correlation necessary to describe excitations into the excited states, and indeed this is not the first time this has been pointed out.[188] CC2 appears to underestimate Rydberg transition with a negative mean signed error. The perturbative EOM methods tested, along with EOM–CCSD, have RMS errors lower than 0.2 eV — three times less than the nearest-performing method, CIS(D) and CC2. Out of the 39 Rydberg states considered, the P–EOM–MBPT2 was more accurate than CC2 by a factor of three. Perhaps even more interesting was that the difference in RMS error between EOM–CCSD and P–EOM–MBPT2 was only 0.06 eV.

While EOM–CCSD is generally the most accurate method considered here, its scaling as $\mathcal{O}(N^6)$ rules it out for use with larger molecular systems. The experimental scaling for the methods tested was demonstrated in Fig. 7.2, and the results tabulated in Tab. 7.7. Because the calculations are iterative, the timing is relative to one average iteration. All EOM methods converge within one iteration of each other. As is seen, only the P–EOM–MBPT2 method is able to achieve the theoretical reduction of $\mathcal{O}(N^6)$ to $\mathcal{O}(N^5)$, making it a computationally cheaper method which scales along other methods such as CIS(D) and CC2.

While EOM–MBPT2 retains the same formal scaling as EOM–CCSD, it does benefit from the reduction of terms which corresponds to a reduced prefactor. Compared to EOM–CCSD, EOM–MBPT2 was found to be 23% cheaper.

Conclusion

We have implemented two perturbative approximations to EOM–CCSD, along with CC2, and tested them against a test set of 11 molecules for a total of 69 excited states, all of which have been studied extensively in the gas phase. The methods were also directly compared to EOM–CCSD. The accuracy and timing of the methods was determined, and it was found that the P–EOM–MBPT2 method outperforms both EOM–CCSD and EOM–MBPT2 in terms of computational cost, lowering the formal scaling from $\mathcal{O}(N^6)$ to $\mathcal{O}(N^5)$. For the $\mathcal{O}(N^5)$ methods considered, CC2 performs best in describing valence states compared to both EOM–CCSD and experiments, which is attributable to the flexibility it retains with respect to orbital relaxation. However, it does not perform nearly as well as P–EOM–MBPT2 in the description of Rydberg states, which better accounts for dynamic correlation. Thus on account of their respective approximation, CC2 is the best $\mathcal{O}(N^5)$ method for describing valence states, whereas P–EOM–MBPT2 is the best $\mathcal{O}(N^5)$ method for describing Rydberg states. Together, P–EOM–MBPT2 and CC2 form a complementary pair of low-scaling algorithms that offers predictive power of wave function-based excited-state methods.

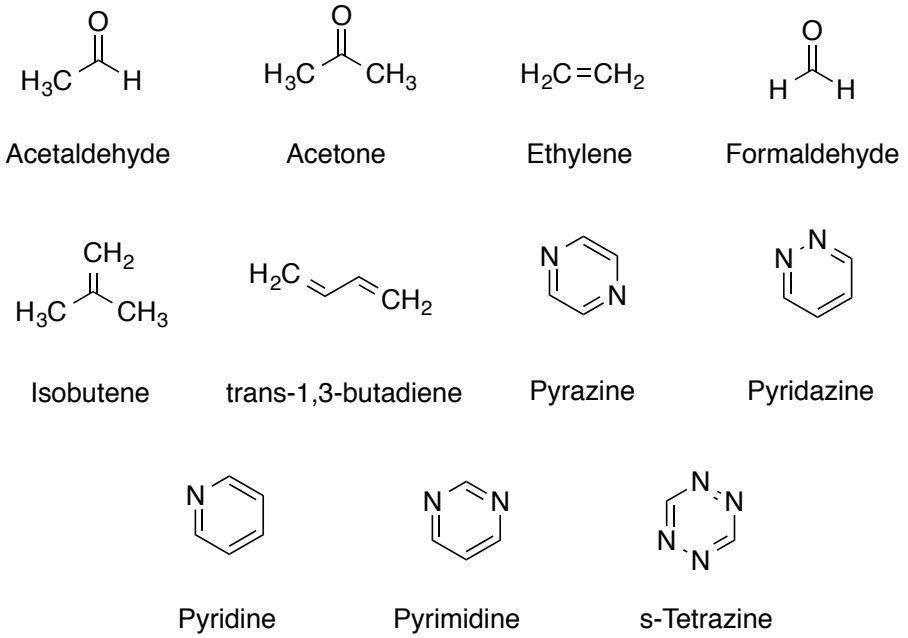

Figure 7.1: Molecules used to test the accuracy of excited-state methods. All molecules were optimized at the MP2/6-311+G** level of theory.

Table 7.1: Mean absolute error (Mean AE), error root mean square (RMS), maximum absolute error (Max AE), and mean signed error (MSE) compared to EOM–CCSD for the first state and all the states of all the molecules (eV), 69 states total.

	All molecules, compared to EOM–CCSD							
	First state				All states			
	Mean AE	RMS	Max AE	MSE	Mean AE	RMS	Max AE	MSE
EOM–MBPT2	0.14	0.16	0.33	0.04	0.13	0.20	1.19	-0.01
P–EOM–MBPT2	0.39	0.43	0.66	0.39	0.25	0.35	0.78	0.21
CC2	0.16	0.17	0.25	-0.12	0.40	0.52	1.69	-0.39
CIS(D)	0.08	0.09	0.14	0.00	0.34	0.45	1.16	-0.24
B3LYP	0.44	0.51	0.85	-0.44	0.78	0.87	1.59	-0.76
RPA	0.52	0.57	1.04	0.39	0.92	1.11	2.61	0.69
CIS	0.62	0.70	1.19	0.55	0.96	1.16	2.65	0.80

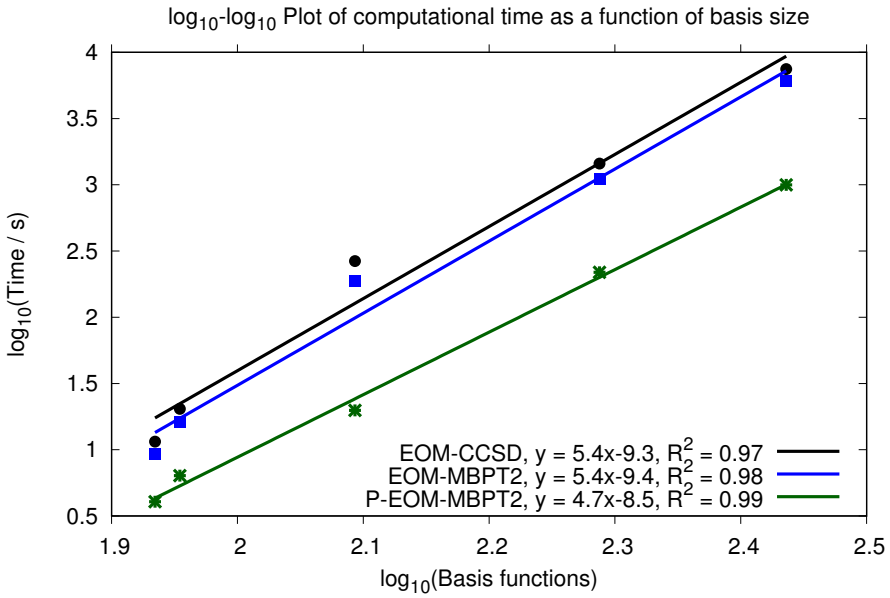

Figure 7.2: Plot of $\log_{10}$(Time), where time was measured in seconds, versus $\log_{10}$(Number basis functions). EOM–CCSD and EOM–MBPT2 have an experimental scaling of $\mathcal{O}(N^{5.4})$, while P–EOM–MBPT2 has an experimental scaling of $\mathcal{O}(N^{4.7})$, nearly an order of magnitude less, as expected.

Table 7.2: Mean absolute error (Mean AE), error root mean square (RMS), maximum absolute error (Max AE), and mean signed error (MSE) compared to EOM–CCSD for all the valence states of all the molecules (eV), 30 states total.

All molecules, compared to EOM–CCSD, valence states only				
	Mean AE	RMS	Max AE	MSE
EOM–MBPT2	0.20	0.29	1.19	0.04
P–EOM–MBPT2	0.48	0.51	0.78	0.41
CC2	0.30	0.47	1.69	-0.27
CIS(D)	0.18	0.29	1.16	0.02
B3LYP	0.47	0.51	0.85	-0.41
RPA	0.89	1.02	2.61	0.61
CIS	0.96	1.10	2.65	0.82

Table 7.3: Mean absolute error (Mean AE), error root mean square (RMS), maximum absolute error (Max AE), and mean signed error (MSE) compared to EOM–CCSD for all the Rydberg states of all the molecules (eV), 39 states total.

All molecules, compared to EOM-CCSD, Rydberg states only				
	Mean AE	RMS	Max AE	MSE
EOM–MBPT2	0.07	0.08	0.25	-0.04
P–EOM–MBPT2	0.07	0.11	0.42	0.05
CC2	0.48	0.55	0.82	-0.48
CIS(D)	0.46	0.54	0.95	-0.44
B3LYP	1.02	1.07	1.59	-1.02
RPA	0.94	1.17	1.85	0.75
CIS	0.96	1.21	1.86	0.79

Table 7.4: Mean absolute error (Mean AE), error root mean square (RMS), maximum absolute error (Max AE), and mean signed error (MSE) compared to experiment for the first state and all the states of all the molecules (eV), 69 states total.

	All molecules, compared to experiment							
	First state				All states			
	Mean AE	RMS	Max AE	MSE	Mean AE	RMS	Max AE	MSE
EOM–CCSD	0.35	0.44	0.82	0.35	0.27	0.36	1.02	0.20
EOM–MBPT2	0.43	0.54	0.96	0.39	0.30	0.43	1.12	0.20
P–EOM–MBPT2	0.74	0.83	1.32	0.74	0.47	0.65	1.40	0.41
CC2	0.23	0.29	0.60	0.23	0.44	0.53	1.26	-0.19
CIS(D)	0.35	0.45	0.78	0.35	0.49	0.61	1.83	-0.04
B3LYP	0.22	0.29	0.55	-0.09	0.67	0.84	1.82	-0.56
RPA	0.75	0.93	1.86	0.74	1.01	1.26	3.63	0.90
CIS	0.90	1.08	2.01	0.90	1.07	1.34	3.67	1.01

Table 7.5: Mean absolute error (Mean AE), error root mean square (RMS), maximum absolute error (Max AE), and mean signed error (MSE) compared to experiment for all the valence states of all the molecules (eV), 30 states total.

All molecules, compared to experiment, valence states only				
	Mean AE	RMS	Max AE	MSE
EOM–CCSD	0.47	0.52	1.02	0.47
EOM–MBPT2	0.56	0.63	1.12	0.51
P–EOM–MBPT2	0.89	0.96	1.40	0.88
CC2	0.36	0.42	1.00	0.20
CIS(D)	0.50	0.59	1.83	0.49
B3LYP	0.20	0.26	0.59	0.06
RPA	1.19	1.44	3.63	1.08
CIS	1.29	1.55	3.67	1.29

Table 7.6: Mean absolute error (Mean AE), error root mean square (RMS), maximum absolute error (Max AE), and mean signed error (MSE) compared to experiment for all the Rydberg states of all the molecules (eV), 39 states total.

All molecules, compared to experiment, Rydberg states only				
	Mean AE	RMS	Max AE	MSE
EOM–CCSD	0.11	0.14	0.45	0.00
EOM–MBPT2	0.10	0.14	0.34	-0.05
P–EOM–MBPT2	0.15	0.20	0.55	0.05
CC2	0.50	0.61	1.26	-0.49
CIS(D)	0.49	0.62	1.32	-0.44
B3LYP	1.03	1.09	1.82	-1.03
RPA	0.88	1.11	1.89	0.75
CIS	0.91	1.15	1.94	0.79

Table 7.7: Scaling of EOM–MBPT2 and P–EOM–MBPT2 compared to EOM–CCSD. EOM–MBPT2 has the same scaling as EOM–CCSD, $\mathcal{O}(N^6)$, but with a 23% smaller prefactor. P–EOM–MBPT2 scales an order of magnitude less than the other methods, and its prefactor cannot be compared to EOM–CCSD because the prefactors compare different scaling terms.

	Scaling		Scaling rel. to EOM–CCSD		
	Exp.	Pred.	Exp.	Pred.	Relative Prefactor
EOM–CCSD	5.44	6.00	1.00	1.00	1.00
EOM–MBPT2	5.44	6.00	1.00	1.00	0.77
P–EOM–MBPT2	4.72	5.00	0.87	0.83	N/A

BIBLIOGRAPHY

[1] Feizhi Ding, Joshua J. Goings, Hongbin Liu, David B. Lingerfelt, and Xiaosong Li. Ab initio two-component Ehrenfest dynamics. *J. Chem. Phys.*, 143:114105, 2015.

[2] Per-Olov Löwdin. Discussion on the Hartree-Fock approximation. *Rev. Mod. Phys.*, 35:496–501, 1963.

[3] Rolf Seeger and John A. Pople. Self-consistent molecular orbital methods. XVIII. constraints and stability in Hartree-Fock theory. *J. Chem. Phys.*, 66:3045–3050, 1977.

[4] H. Fukutome. Unrestricted Hartree–Fock theory and its applications to molecules and chemical reactions. *Int. J. Quant. Chem.*, 20(5):955–1065, 1981.

[5] Per-Olov Lödwin and István Mayer. Some studies of the general Hartree-Fock method. *Adv. Quantum Chem.*, 24:79–114, 1992.

[6] Sharon Hammes-Schiffer and Hans C. Andersen. The advantages of the general Hartree-Fock method for future computer simulation of materials. *J. Chem. Phys.*, 99(3):1901–1913, 1993.

[7] Philip Warren Anderson. *Basic Notions of Condensed Matter Physics*. Benjamin-Cummings, 1984.

[8] Yao Cui, Ireneusz W Bulik, Carlos A Jiménez-Hoyos, Thomas M Henderson, and Gustavo E Scuseria. Proper and improper zero energy modes in Hartree-Fock theory and their relevance for symmetry breaking and restoration. *J. Chem. Phys.*, 139(15):154107, 2013.

[9] Ireneusz W. Bulik, Giovanni Scalmani, Michael J. Frisch, and Gustavo E. Scuseria. Noncollinear density functional theory having proper invariance and local torque properties. *Phys. Rev. B*, 87:035117, 2013.

[10] Joshua J Goings, Feizhi Ding, Michael J Frisch, and Xiaosong Li. Stability of the Complex Generalized Hartree-Fock Equations. *J. Chem. Phys.*, 142(15):154109, 2015.

[11] Feizhi Ding, Joshua J. Goings, Michael J. Frisch, and Xiaosong Li. Ab initio non-relativistic spin dynamics. *J. Chem. Phys.*, 141(21):214111, 2014.

[12] Juan E Peralta, Oded Hod, and Gustavo E Scuseria. Magnetization dynamics from time-dependent noncollinear spin density functional theory calculations. *J. Chem. Theor. Comput.*, 11(8):3661–3668, 2015.

[13] Michal Repisky, Lukas Konecny, Marius Kadek, Stanislav Komorovsky, Olga L Malkin, Vladimir G Malkin, and Kenneth Ruud. Excitation energies from real-time propagation of the four-component Dirac–Kohn–Sham equation. *J. Chem. Theor. Comput.*, 11(3):980–991, 2015.

[14] Joshua J. Goings, Joseph M. Kasper, Franco Egidi, Shichao Sun, and Xiaosong Li. Real time propagation of the exact two component time-dependent density functional theory. *J. Chem. Phys.*, 145(10):104107, 2016.

[15] Lukas Konecny, Marius Kadek, Stanislav Komorovsky, Olga L Malkina, Kenneth Ruud, and Michal Repisky. Acceleration of relativistic electron dynamics by means of X2C transformation: Application to the calculation of nonlinear optical properties. *J. Chem. Theor. Comput.*, 12(12):5823–5833, 2016.

[16] Werner Kutzelnigg and Wenjian Liu. Quasirelativistic theory equivalent to fully relativistic theory. *J. Chem. Phys.*, 123:241102, 2005.

[17] Miroslaŵ Ilias and Trond Saue. An infinite-order relativistic Hamiltonian by a simple one-step transformation. *J. Chem. Phys.*, 126:064102, 2007.

[18] Wenjian Liu. Ideas of relativistic quantum chemistry. *Mol. Phys.*, 108:1679–1706, 2010.

[19] Daoling Peng, Nils Middendorf, Florian Weigend, and Markus Reiher. An efficient implementation of two-component relativistic exact-decoupling methods for large molecules. *J. Chem. Phys.*, 138:184105, 2013.

[20] Franco Egidi, Joshua J. Goings, Michael J. Frisch, and Xiaosong Li. Direct atomic-orbital-based relativistic two-component linear response method for calculating excited-state fine structures. *J. Chem. Theor. Comput.*, 12(8):3711–3718, 2016.

[21] Stefano Sanvito. Molecular spintronics. *Chem. Soc. Rev.*, 40(6):3336–3355, 2011.

[22] J. L. Stuber and J. Paldus. *Symmetry Breaking in the Independent Particle Model*, pages 67–139. Kluwer Academic Publishers, 2003.

[23] S. Sharma, J.K. Dewhurst, C. Ambrosch-Draxl, S. Kurth, N. Helbig, S. Pittalis, S. Shallcross, L. Nordström, and E.K.U. Gross. First-principles approach to noncollinear magnetism: Towards spin dynamics. *Phys. Rev. Lett.*, 98(19):196405, 2007.

[24] Juan E. Peralta, Gustavo E. Scuseria, and Michael J. Frisch. Noncollinear magnetism in density functional calculations. *Phys. Rev. B*, 75:125119, 2007.

[25] Giovanni Scalmani and Michael J. Frisch. A new approach to noncollinear spin density functional theory beyond the local density approximation. *J. Chem. Theor. Comput.*, 8:2193–2196, 2012.

[26] S. Yamanaka, D. Yamaki, Y. Shigeta, H. Nagao, and K. Yamaguchi. Noncollinear spin density functional theory for spin-frustrated and spin-degenerate systems. *Int. J. Quant. Chem.*, 84:670–676, 2001.

[27] Johannes Schimpl, Helena M. Petrilli, and Peter E. Blöchl. Nitrogen binding to the femo-cofactor of nitrogenase. *J. Am. Chem. Soc.*, 125:15772–15778, 2003.

[28] Sijie Luo, Ivan Rivalta, Victor Batista, and Donald G. Truhlar. Noncollinear spins provide a self-consistent treatment of the low-spin state of a biomimetic oxomanganese synthetic trimer inspired by the oxygen evolving complex of photosystem ii. *J. Phys. Chem. Lett.*, 2:2629–2633, 2011.

[29] Sijie Luo and Donald G. Truhlar. Noncollinear spin states for density functional calculations of open-shell and multi-configurational systems: Dissociation of mno and nio and barrier heights of o3, beh2, and h4. *J. Chem. Theor. Comput.*, 9:5349–5355, 2013.

[30] Jean-Paul Blaizot and Georges Ripka. *Quantum Theory of Finite Systems*, volume 3. Mit Press Cambridge, 1986.

[31] Gustavo E Scuseria, Carlos A Jiménez-Hoyos, Thomas M Henderson, Kousik Samanta, and Jason K Ellis. Projected quasiparticle theory for molecular electronic structure. *J. Chem. Phys.*, 135(12):124108, 2011.

[32] Carlos A Jiménez-Hoyos, Thomas M Henderson, Takashi Tsuchimochi, and Gustavo E Scuseria. Projected Hartree–Fock theory. *J. Chem. Phys.*, 136(16):164109, 2012.

[33] J Čížek and J Paldus. Stability conditions for the solutions of the Hartree-Fock equations for atomic and molecular systems. application to the pi-electron model of cyclic polyenes. *J. Chem. Phys.*, 47(10):3976–3985, 1967.

[34] D J Thouless. Stability conditions and nuclear rotations in the Hartree-Fock theory. *Nucl. Phys. A*, 21:225–232, 1960.

[35] James S Wright and Gino A DiLabio. Structure and stability of hydrogen rings. *J. Phys. Chem.*, 96(26):10793–10799, 1992.

[36] Haijun Jiao, Paul von Ragué Schleyer, and Mikhail N Glukhovtsev. Are the D_{mh} symmetric H_x^q rings with 4n+2 σ-electrons and hydrogen clusters aromatic? *J. Phys. Chem.*, 100(30):12299–12304, 1996.

[37] John H Black. The abundance and excitation of interstellar H_3^+. *Philos. T. Roy. Soc. A.*, 358(1774):2515–2521, 2000.

[38] Eric Herbst. The astrochemistry of H_3^+. *Philos. T. Roy. Soc. A.*, 358(1774):2523–2534, 2000.

[39] I Dabrowski and G Herzberg. The electronic emission spectrum of triatomic hydrogen. I. parallel bands of H_3 and D_3 near 5600 and 6025 å. *Can. J. Phys.*, 58(8):1238–1249, 1980.

[40] Xinxing Zhang, Gaoxiang Liu, Gerd Gerd Gantefoer, Kit Hansell Bowen, Jr, and Anastassia N Alexandrova. $PtZnH_5^-$, a σ-aromatic cluster. *J. Phys. Chem. Lett.*, 5(9):1596–1601, 2014.

[41] M. J. Frisch, G. W. Trucks, H. B. Schlegel, G. E. Scuseria, M. A. Robb, J. R. Cheeseman, G. Scalmani, V. Barone, B. Mennucci, G. A. Petersson, H. Nakatsuji, M. Caricato, X. Li, H. P. Hratchian, A. F. Izmaylov, J. Bloino, G. Zheng, J. L. Sonnenberg, W. Liang, M. Hada, M. Ehara, K. Toyota, R. Fukuda, J. Hasegawa, M. Ishida, T. Nakajima, Y. Honda, O. Kitao, H. Nakai, T. Vreven, Jr. J. A. Montgomery, J. E. Peralta, F. Ogliaro, M. Bearpark, J. J. Heyd, E. Brothers, K. N. Kudin, V. N. Staroverov, T. Keith, R. Kobayashi, J. Normand, K. Raghavachari, A. Rendell, J. C. Burant, S. S. Iyengar, J. Tomasi, M. Cossi, N. Rega, J. M. Millam, M. Klene, J. E. Knox, J. B. Cross, V. Bakken, C. Adamo, J. Jaramillo, R. Gomperts, R. E. Stratmann, O. Yazyev, A. J. Austin, R. Cammi, C. Pomelli, J. W. Ochterski, R. L. Martin, K. Morokuma, V. G. Zakrzewski, G. A. Voth, P. Salvador, J. J. Dannenberg, S. Dapprich, P. V. Parandekar, N. J. Mayhall, A. D. Daniels, Ö. Farkas, J. B. Foresman, J. V. Ortiz, J. Cioslowski, and D. J. Fox. Gaussian Development Version Revision H.36. Gaussian Inc., Wallingford CT 2014.

[42] Thom H Dunning Jr. Gaussian basis sets for use in correlated molecular calculations. I. the atoms boron through neon and hydrogen. *J. Chem. Phys.*, 90(2):1007–1023, 1989.

[43] F. L. Hirshfeld. Bonded-atom fragments for describing molecular charge densities. *Theor. Chem. Acc.*, 44:129, 1977.

[44] Christoph van Wüllen. Spin densities in two-component relativistic density functional calculations: Noncollinear versus collinear approach. *J. Comput. Chem.*, 23:779–785, 2002.

[45] Brian N Papas and Henry F Schaefer III. Homonuclear transition-metal trimers. *J. Chem. Phys.*, 123(7):074321, 2005.

[46] Willard R Wadt and P Jeffrey Hay. Ab initio effective core potentials for molecular calculations. potentials for main group elements Na to Bi. *J. Chem. Phys.*, 82(1):284–298, 1985.

[47] Samir Lounis. Non-collinear magnetism induced by frustration in transition-metal nanostructures deposited on surfaces. *J. Phys.–Condens. Mat.*, 26(27):273201, 2014.

[48] D. Yamaki, Y. Shigeta, S. Yamanaka, H. Nagao, and K. Yamaguchi. MP2, Tamm-Dancoff, and RPA methods based on the generalized HF solution. *Int. J. Quant. Chem.*, 80:701–707, 2000.

[49] Per-Olov Löwdin. Quantum theory of many-particle systems. III. extension of the Hartree-Fock scheme to include degenerate systems and correlation effects. *Phys. Rev.*, 97(6):1509, 1955.

[50] Xuefei Xu, Ke R. Yang, and Donald G. Truhlar. Testing noncollinear spin-flip, collinear spin-flip, and conventional time-dependent density functional theory for predicting electronic excitation energies of closed-shell atoms. *J. Chem. Theor. Comput.*, 10:2070–2084, 2014.

[51] Michael Kün and Florian Weigend. Implementation of two-component time-dependent density functional theory in TURBOMOLE. *J. Chem. Theor. Comput.*, 9:5341–5348, 2013.

[52] AD McLachlan and MA Ball. Time-dependent Hartree-Fock theory for molecules. *Rev. Mod. Phys.*, 36(3):844, 1964.

[53] Robert A Harris. Oscillator strengths and rotational strengths in Hartree–Fock theory. *J. Chem. Phys.*, 50(9):3947–3951, 1969.

[54] A. Dreuw and M. Head-Gordon. Single-reference ab initio methods for the calculation of excited states of large molecules. *Chem. Rev.*, 105:4009–4037, 2005.

[55] DL Yeager, MAC Nascimento, and V McKoy. Some applications of excited-state-excited-state transition densities. *Phys. Rev. A*, 11(4):1168, 1975.

[56] Justin M Turney, Andrew C Simmonett, Robert M Parrish, Edward G Hohenstein, Francesco A Evangelista, Justin T Fermann, Benjamin J Mintz, Lori A Burns, Jeremiah J Wilke, Micah L Abrams, et al. Psi4: An open-source ab initio electronic structure program. *WIREs Comput. Mol. Sci.*, 2(4):556–565, 2012.

[57] C David Sherrill and Henry F Schaefer. The configuration interaction method: Advances in highly correlated approaches. *Adv. Quantum Chem.*, 34:143–269, 1999.

[58] Carlos A Jiménez-Hoyos, R Rodríguez-Guzmán, and Gustavo E Scuseria. Excited electronic states from a variational approach based on symmetry-projected Hartree–Fock configurations. *J. Chem. Phys.*, 139(22):224110, 2013.

[59] Takashi Tsuchimochi and Troy Van Voorhis. Time-dependent projected Hartree-Fock. *J. Chem. Phys.*, 142(12):124103, 2015.

[60] Marvin Douglas and Norman M. Kroll. Quantum electrodynamical corrections to the fine structure of helium. *Ann. Phys.*, 82:89–155, 1974.

[61] Bernd A. Hess. Applicability of the no-pair equation with free-particle projection operators to atomic and molecular structure calculations. *Phys. Rev. A*, 32:756–763, 1985.

[62] Bernd A. Hess. Relativistic electronic-structure calculations employing a two-component no-pair formalism with external-field projection operators. *Phys. Rev. A*, 33:3742–3748, 1986.

[63] Reinhard Samzow, Bernd A. Hess, and Georg Jansen. The two-electron terms of the nopair Hamiltonian. *J. Chem. Phys.*, 96:1227–1231, 1992.

[64] Kenneth G. Dyall. Interfacing relativistic and nonrelativistic methods. I. Normalized elimination of the small component in the modified Dirac equation. *J. Chem. Phys.*, 106:9618–9626, 1997.

[65] Kenneth G. Dyall. Interfacing relativistic and nonrelativistic methods. II. investigation of a low-order approximation. *J. Chem. Phys.*, 109:4201–4208, 1998.

[66] Kenneth G. Dyall and Thomas Enevoldsen. Interfacing relativistic and nonrelativistic methods. III. Atomic 4-spinor expansions and integral approximations. *J. Chem. Phys.*, 111:10000–10007, 1999.

[67] Kenneth G. Dyall. Interfacing relativistic and nonrelativistic methods. II. One- and two-electron scalar approximations. *J. Chem. Phys.*, 115:9136–9143, 2001.

[68] Michael Filatov and Dieter Cremer. A new quasi-relativistic approach for density functional theory based on the normalized elimination of the small component. *Chem. Phys. Lett.*, 351:259–266, 2002.

[69] K. G. Dyall and K. Faegri Jr. *Introduction to Relativistic Quantum Chemistry*. Oxford University Press, 2007.

[70] Markus Reiher and Alexander Wolf. *Relativistic Quantum Chemistry*. Wiley-VCH, second edition, 2015.

[71] Pekka Pyykkö. Relativistic effects in chemistry: More common than you thought. *Annu. Rev. Phys. Chem.*, 63:45–64, 2012.

[72] Wenjian Liu and Daoling Peng. Infinite-order quasirelativistic density functional method based on the exact matrix quasirelativistic theory. *J. Chem. Phys.*, 125:044102, 2006.

[73] Wenjian Liu and Daoling Peng. Exact two-component Hamiltonians revisited. *J. Chem. Phys.*, 131:031104, 2009.

[74] Daoling Peng, Wenjian Liu, Yunlong Xiao, and Lan Cheng. Making four- and two-component relativistic density functional methods fully equivalent based on the idea of from atoms to molecule. *J. Chem. Phys.*, 127:104106, 2007.

[75] Trond Saue. Relativistic Hamiltonians for chemistry: A primer. *Comp. Phys. Comm.*, 12:3077–3094, 2011.

[76] Wenjian Liu. Advances in relativistic molecular quantum mechanics. *Phys. Rep.*, 537:59–89, 2014.

[77] Wenjian Liu. The big picture of relativistic molecular quantum mechanics. *Nat. Sci. Rev.*, 3(2):204–221, 2016.

[78] E. van Lenthe, E. J. Baerends, and J. G. Snijders. Relativistic regular two-component Hamiltonians. *J. Chem. Phys.*, 99:4597–4610, 1993.

[79] E. van Lenthe, E. J. Baerends, and J. G. Snijders. Relativistic total energy using regular approximations. *J. Chem. Phys.*, 101:9783–9792, 1994.

[80] Christoph van Wülien. Molecular density functional calculations in the regular relativistic approximation: Method, application to coinage metal diatomics, hydrides, fluorides and chlorides, and comparison with first-order relativistic calculations. *J. Chem. Phys.*, 109:392–399, 1998.

[81] Jun Gao, Wenli Zou, Wenjian Liu, Yunlong Xiao, Daoling Peng, Bo Song, and Chengbu Liu. Time-dependent four-component relativistic density-functional theory for excitation energies. II. The exchange-correlation kernel. *J. Chem. Phys.*, 123:054102, 2005.

[82] Radovan Bast, Hans J. Aa. Jensen, and Trond Saue. Relativistic adiabatic time-dependent density functional theory using hybrid functionals and noncollinear spin magnetization. *Int. J. Quant. Chem.*, 109:2091–2112, 2009.

[83] Fan Wang, Tom Ziegler, Erik van Lenthe, Stan van Gisbergen, and Evert J. Baerends. The calculation of excitation energies based on the relativistic two-component zeroth-order regular approximation and time-dependent density-functional with full use of symmetry. *J. Chem. Phys.*, 122:204103, 2005.

[84] Ayako Nakata, Takao Tsuneda, and Kimihiko Hirao. Spin-orbit relativistic long-range corrected time-dependent density functional theory for investigating spin-forbidden transitions in photochemical reactions. *J. Chem. Phys.*, 135(22):224106, 2011.

[85] Jun Gao, , Wenjian Liu, Bo Song, and Chengbu Liu. Time-dependent four-component relativistic density functional theory for excitation energies. *J. Chem. Phys.*, 121:6658–6666, 2004.

[86] Daoling Peng, Wenli Zou, and Wenjian Liu. Time-dependent quasirelativistic density-functional theory based on the zeroth-order regular approximation. *J. Chem. Phys.*, 123:144101, 2005.

[87] Wenhua Xu, Jianyi Ma, Daoling Pen, Wenli Zou, Wenjian Liu, and Volker Staemmler. Excited states of ReO_4^-: A comprehensive time-dependent relativistic density functional theory study. *Chem. Phys.*, 356:219–228, 2009.

[88] Wenhua Xu, Yong Zhang, and Wenjian Liu. Time-dependent relativistic density functional study of Yb and YbO. *Sci. China Ser. B Chem.*, 52:1945–1953, 2009.

[89] Yong Zhang, Wenhua Xu, Qiming Sun, Wenli Zou, and Wenjian Liu. Excited states of OsO_4: A comprehensive time-dependent relativistic density functional theory study. *J. Comput. Chem.*, 31:532–551, 2010.

[90] Zhendong Li, Bingbing Suo, Yong Zhang, Yunlong Xiao, and Wenjian Liu. Combining spin-adapted open-shell TD-DFT with spin–orbit coupling. *Mol. Phys.*, 111(24):3741–3755, 2013.

[91] Xiaosong Li, Stanley M. Smith, Alexei N. Markevitch, Dmitri A. Romanov, Robert J. Levis, and H. Bernhard Schlegel. A time-dependent Hartree-Fock approach for studying

the electronic optical response of molecules in intense fields. *Phys. Chem. Chem. Phys.*, 7:233–239, 2005.

[92] Kenneth Lopata and Niranjan Govind. Modeling fast electron dynamics with real-time time-dependent density functional theory: Application to small molecules and chromophores. *J. Chem. Theor. Comput.*, 7(5):1344–1355, 2011.

[93] J. C. Boettger. Approximate two-electron spin-orbit coupling term for density-functional-theory DFT calculations using the Douglas-Kroll-Hess transformation. *Phys. Rev. B*, 62:7809–7815, 2000.

[94] Fan Wang and Wenjian Liu. Comparison of different polarization schemes in open-shell relativistic density functional calculations. *J. Chin. Chem. Soc.*, 50:597–606, 2003.

[95] K. Capelle, G. Vignale, and B.L. Györffy. Spin currents and spin dynamics in time-dependent density functional theory. *Phys. Rev. Lett.*, 87:206403, 2001.

[96] Christine M. Isborn, Xiaosong Li, and John C. Tully. TDDFT Ehrenfest dynamics: Collisions between atomic oxygen and graphite clusters. *J. Chem. Phys.*, 126:134307, 2007.

[97] Wenkel Liang, Craig T. Chapman, and Xiaosong Li. Efficient first-principles electronic dynamics. *J. Chem. Phys.*, 134(18):184102, 2011.

[98] Feizhi Ding, Wenkel Liang, Craig T. Chapman, Christine M. Isborn, and Xiaosong Li. On the gauge invariance of nonperturbative electronic dynamics using the time-dependent Hartree-Fock and time-dependent Kohn-Sham. *J. Chem. Phys.*, 135(16):164101, 2011.

[99] Alexander Wolf and Markus Reiher. Exact decoupling of the Dirac hamiltonian. III. molecular properties. *J. Chem. Phys.*, 121:064102, 2004.

[100] M. J. Frisch, G. W. Trucks, H. B. Schlegel, G. E. Scuseria, M. A. Robb, J. R. Cheeseman, G. Scalmani, V. Barone, B. Mennucci, G. A. Petersson, H. Nakatsuji, M. Caricato, X. Li, H. P. Hratchian, J. Bloino, B. G. Janesko, A. F. Izmaylov, A. Marenich, F. Lipparini, G. Zheng, J. L. Sonnenberg, W. Liang, M. Hada, M. Ehara, K. Toyota, R. Fukuda, J. Hasegawa, M. Ishida, T. Nakajima, Y. Honda, O. Kitao, H. Nakai, T. Vreven, K. Throssell, J. A. Montgomery Jr., J. E. Peralta, F. Ogliaro, M. Bearpark, J. J. Heyd, E. Brothers, K. N. Kudin, V. N. Staroverov, T. Keith, R. Kobayashi, J. Normand, K. Raghavachari, A. Rendell, J. C. Burant, S. S. Iyengar, J. Tomasi, M. Cossi, N. Rega, J. M. Millam, M. Klene, J. E. Knox, J. B. Cross, V. Bakken, C. Adamo, J. Jaramillo, R. Gomperts, R. E. Stratmann, O. Yazyev, A. J. Austin, R. Cammi, C. Pomelli, J. W. Ochterski, R. L. Martin, K. Morokuma, V. G. Zakrzewski,

G. A. Voth, P. Salvador, J. J. Dannenberg, S. Dapprich, P. V. Parandekar, N. J. Mayhall, A. D. Daniels, O. Farkas, J. B. Foresman, J. V. Ortiz, J. Cioslowski, , and D. J. Fox. Gaussian Development Version Revision I.04. Gaussian Inc., Wallingford CT 2016.

[101] John C Slater. A simplification of the Hartree-Fock method. *Phys. Rev.*, 81(3):385, 1951.

[102] SH Vosko, Ll Wilk, and M Nusair. Accurate spin-dependent electron liquid correlation energies for local spin density calculations: a critical analysis. *Can. J. Phys.*, 58(8):1200–1211, 1980.

[103] Takeshi Noro, Masahiro Sekiya, and Toshikatsu Koga. Segmented contracted basis sets for atoms H through Xe: Sapporo-(DK)-nZP sets (n = D, T, Q). *Theor. Chem. Acc.*, 131:1124, 2012.

[104] Adam Bruner, Daniel LaMaster, and Kenneth Lopata. Accelerated broadband spectra using transition dipole decomposition and Padé approximants. *J. Chem. Theor. Comput.*, 12(8):3741–3750, 2016.

[105] JE Sansonetti and WC Martin. Handbook of basic atomic spectroscopic data. *J. Phys. Chem. Ref. Data*, 34(4):1559–2259, 2005.

[106] KP Huber and G Herzberg. *Constants of Diatomic Molecules*. Springer, New York, 1979.

[107] Roger J Crossley. *Chirality and Biological Activity of Drugs.* , volume 7. CRC Press, 1995.

[108] Ron Naaman and David H Waldeck. Spintronics and chirality: Spin selectivity in electron transport through chiral molecules. *Annu. Rev. Phys. Chem.*, 66:263–281, 2015.

[109] RA Jishi, MS Dresselhaus, and G Dresselhaus. Symmetry properties of chiral carbon nanotubes. *Phys. Rev. B*, 47(24):16671, 1993.

[110] Stephen R Martin and Maria J Schilstra. Circular dichroism and its application to the study of biomolecules. *Meth. Chem. Biol.*, 84:263–293, 2008.

[111] Martin Quack. How important is parity violation for molecular and biomolecular chirality? *Angew. Chem. Int. Ed.*, 41(24):4618–4630, 2002.

[112] Laurence D Barron. *Molecular Light Scattering and Optical Activity.* Cambridge University Press, 2004.

[113] T Daniel Crawford. Ab initio calculation of molecular chiroptical properties. *Theor. Chem. Acc.*, 115(4):227–245, 2006.

[114] Trygve Helgaker, Sonia Coriani, Poul Jørgensen, Kasper Kristensen, Jeppe Olsen, and Kenneth Ruud. Recent advances in wave function-based methods of molecular-property calculations. *Chem. Rev.*, 112(1):543–631, 2012.

[115] T Daniel Crawford. High-accuracy quantum chemistry and chiroptical properties. *Comprehensive Chiroptical Spectroscopy: Instrumentation, Methodologies, and Theoretical Simulations, Volume 1*, pages 675–697, 2012.

[116] PJ Stephens, FJ Devlin, JR Cheeseman, MJ Frisch, O Bortolini, and P Besse. Determination of absolute configuration using ab initio calculation of optical rotation. *Chirality*, 15(S1):S57–S64, 2003.

[117] PJ Stephens, FJ Devlin, JR Cheeseman, MJ Frisch, and C Rosini. Determination of absolute configuration using optical rotation calculated using density functional theory. *Org. Lett.*, 4(26):4595–4598, 2002.

[118] Filipp Furche, Reinhart Ahlrichs, Claudia Wachsmann, Edwin Weber, Adam Sobanski, Fritz Vögtle, and Stefan Grimme. Circular dichroism of helicenes investigated by time-dependent density functional theory. *J. Am. Chem. Soc.*, 122(8):1717–1724, 2000.

[119] Stefan Grimme, Jörg Harren, Adam Sobanski, and Fritz Vögtle. Structure/chiroptics relationships of planar chiral and helical molecules. *Eur. J. Org. Chem.*, 1998(8):1491–1509, 1998.

[120] Mary C Tam, Nicholas J Russ, and T Daniel Crawford. Coupled cluster calculations of optical rotatory dispersion of (s)-methyloxirane. *J. Chem. Phys.*, 121(8):3550–3557, 2004.

[121] Christian Diedrich and Stefan Grimme. Systematic investigation of modern quantum chemical methods to predict electronic circular dichroism spectra. *J. Phys. Chem. A*, 107(14):2524–2539, 2003.

[122] Patrick Norman, David M Bishop, Hans Jørgen Aa. Jensen, and Jens Oddershede. Near-resonant absorption in the time-dependent self-consistent field and multiconfigurational self-consistent field approximations. *J. Chem. Phys.*, 115(22):10323–10334, 2001.

[123] Auayporn Jiemchooroj and Patrick Norman. Electronic circular dichroism spectra from the complex polarization propagator. *J. Chem. Phys.*, 126(13):134102, 2007.

[124] Wenkel Liang, Sean A. Fischer, Michael J. Frisch, and Xiaosong Li. Energy-specific linear response TDHF/TDDFT for calculating high-energy excited states. *J. Chem. Theor. Comput.*, 7(11):3540–3547, 2011.

[125] Patrick J. Lestrange, Phu D. Nguyen, and Xiaosong Li. Calibration of energy-specific TDDFT for modeling K-edge XAS spectra of light elements. *J. Chem. Theor. Comput.*, 11:2994–2999, 2015.

[126] Bo Peng, Patrick J Lestrange, Joshua J Goings, Marco Caricato, and Xiaosong Li. Energy-specific equation-of-motion coupled-cluster methods for high-energy excited states: Application to K-edge X-ray absorption spectroscopy. *J. Chem. Theor. Comput.*, 11(9):4146–4153, 2015.

[127] K Yabana and GF Bertsch. Application of the time-dependent local density approximation to optical activity. *Phys. Rev. A*, 60(2):1271, 1999.

[128] Daniele Varsano, Leonardo A Espinosa-Leal, Xavier Andrade, Miguel AL Marques, Rosa Di Felice, and Angel Rubio. Towards a gauge invariant method for molecular chiroptical properties in TDDFT. *Phys. Chem. Chem. Phys.*, 11(22):4481–4489, 2009.

[129] Samat Tussupbayev, Niranjan Govind, Kenneth Lopata, and Christopher J Cramer. Comparison of real-time and linear-response time-dependent density functional theories for molecular chromophores ranging from sparse to high densities of states. *J. Chem. Theor. Comput.*, 11(3):1102–1109, 2015.

[130] Xavier Andrade, David Strubbe, Umberto De Giovannini, Ask Hjorth Larsen, Micael JT Oliveira, Joseba Alberdi-Rodriguez, Alejandro Varas, Iris Theophilou, Nicole Helbig, Matthieu J Verstraete, et al. Real-space grids and the Octopus code as tools for the development of new simulation approaches for electronic systems. *Phys. Chem. Chem. Phys.*, pages 31371–31396, 2015.

[131] J. P. Perdew, K. Burke, and M. Ernzerhof. Generalized gradient approximation made simple. *Phys. Rev. Lett.*, 77:3865–3868, 1996.

[132] John P Perdew, Kieron Burke, and Matthias Ernzerhof. Errata: Generalized gradient approximation made simple. *Phys. Rev. Lett.*, 78:1396, 1997.

[133] Praveen C Hariharan and John A Pople. The influence of polarization functions on molecular orbital hydrogenation energies. *Theor. Chem. Acc.*, 28(3):213–222, 1973.

[134] RBJS Krishnan, J Stephen Binkley, Rolf Seeger, and John A Pople. Self-consistent molecular orbital methods. XX. A basis set for correlated wave functions. *J. Chem. Phys.*, 72(1):650–654, 1980.

[135] Timothy Clark, Jayaraman Chandrasekhar, Günther W Spitznagel, and Paul Von Ragué Schleyer. Efficient diffuse function-augmented basis sets for anion calculations. III. the 3-21+G basis set for first-row elements, Li–F. *J. Comput. Chem.*, 4(3):294–301, 1983.

[136] A Breest, P Ochmann, F Pulm, KH Gödderz, M Carnell, and J Hormes. Experimental circular dichroism and VUV spectra of substituted oxiranes and thiiranes. *Mol. Phys.*, 82(3):539–551, 1994.

[137] Keld L Bak, Aage E Hansen, Kenneth Ruud, Trygve Helgaker, Jeppe Olsen, and Poul Jørgensen. Ab initio calculation of electronic circular dichroism fortrans-cyclooctene using london atomic orbitals. *Theor. Chem. Acc.*, 90(5-6):441–458, 1995.

[138] Jochen Autschbach, Tom Ziegler, Stan JA van Gisbergen, and Evert Jan Baerends. Chiroptical properties from time-dependent density functional theory. I. Circular dichroism spectra of organic molecules. *J. Chem. Phys.*, 116(16):6930–6940, 2002.

[139] K. Yabana and G. F. Bertsch. Time-dependent local-density approximation in real time. *Phys. Rev. B*, 54:4484, 1996.

[140] Feizhi Ding, Emilie B. Guidez, Christine M. Aikens, and Xiaosong Li. Quantum coherent plasmon in silver nanowires: A real-time TDDFT study. *J. Chem. Phys.*, 140(24):244705, 2014.

[141] Bo Peng, David B Lingerfelt, Feizhi Ding, Christine M Aikens, and Xiaosong Li. Real-Time TDDFT Studies of Exciton Decay And Transfer in Silver Nanowire Arrays. *J. Phys. Chem. C*, 119(11):6421–6427, 2015.

[142] Joshua J. Goings and Xiaosong Li. An atomic orbital based real-time time-dependent density functional theory for computing electronic circular dichroism band spectra. *J. Chem. Phys.*, 144(23):234102, 2016.

[143] Sean A Fischer, Christopher J Cramer, and Niranjan Govind. Excited state absorption from real-time time-dependent density functional theory. *J. Chem. Theor. Comput.*, 11(9):4294–4303, 2015.

[144] Feizhi Ding, Benjamin E. Van Kuiken, Bruce E. Eichinger, and Xiaosong Li. An efficient method for calculating dynamical hyperpolarizabilities using real-time time-dependent density functional theory. *J. Chem. Phys.*, 138:064104, 2013.

[145] D. A. Micha. A self-consistent eikonal treatment of electronic-transitions in molecular collisions. *J. Chem. Phys.*, 78:7138–7145, 1983.

[146] J. C. Tully. Mixed quantum-classical dynamics. *Faraday Discuss.*, 110:407–419, 1998.

[147] Pengfei Huo and David F. Coker. Consistent schemes for non-adiabatic dynamics derived from partial linearized density matrix propagation. *J. Chem. Phys.*, 137(22), 2012.

[148] Christopher Stopera, Buddhadev Maiti, Thomas V. Grimes, Patrick M. McLaurin, and Jorge A. Morales. Dynamics of H^+ + CO at ELab = 30 eV. *J. Chem. Phys.*, 136(5), 2012.

[149] Franco Egidi, Julien Bloino, Chiara Cappelli, and Vincenzo Barone. A robust and effective time-independent route to the calculation of resonance raman spectra of large molecules in condensed phases with the inclusion of duschinsky, herzberg–teller, anharmonic, and environmental effects. *J. Chem. Theor. Comput.*, 10(1):346–363, 2014.

[150] S. I. Sawada, A. Nitzan, and H. Metiu. Mean-trajectory approximation for charge-transfer and energy-transfer processes at surfaces. *Phys. Rev. B*, 32:851, 1985.

[151] Xiaosong Li, John C. Tully, H. Bernhard Schlegel, and Michael J. Frisch. Ab initio Ehrenfest dynamics. *J. Chem. Phys.*, 123(8):084106, 2005.

[152] Fan Wang, Chi Yung Yam, Li Hong Hu, and Guan Hua Chen. Time-dependent density functional theory based Ehrenfest dynamics. *J. Chem. Phys.*, 135:044126, 2011.

[153] H. Bernhard Schlegel, Stanley M. Smith, and Xiaosong Li. Electronic optical response of molecules in intense fields: Comparison of TD-HF, TD-CIS, and TD-CIS(D) approaches. *J. Chem. Phys.*, 126(24):244110, 2007.

[154] Christine M. Isborn and Xiaosong Li. Singlet-triplet transitions in real-time time-dependent Hartree-Fock/density functional theory. *J. Chem. Theor. Comput.*, 5(9):2415–2419, 2009.

[155] J. Franck and E. G. Dymond. Elementary processes of photochemical reactions. *T. Faraday Soc.*, 21:536–542, 1926.

[156] Edward Condon. A theory of intensity distribution in band systems. *Phys. Rev.*, 28:1182–1201, Dec 1926.

[157] H. Sponer and E. Teller. Electronic spectra of polyatomic molecules. *Rev. Mod. Phys.*, 13:75–170, Apr 1941.

[158] Vincenzo Barone. The virtual multifrequency spectrometer: A new paradigm for spectroscopy. *WIREs Comput. Mol. Sci.*, 6(2):86–110, 2016.

[159] R.G. Gordon. Correlation functions for molecular motion. In *Adv. Magn. Reson.*, volume 3 of *Advances in Magnetic and Optical Resonance*, pages 1 – 42. Academic Press, 1968.

[160] Eric J. Heller. The semiclassical way to molecular spectroscopy. *Acc. Chem. Res.*, 14(12):368–375, 1981.

[161] G.C. Schatz and M.A. Ratner. *Quantum Mechanics in Chemistry*, pages 201–208. Dover Books on Chemistry. Dover Publications, 1993.

[162] J. G. Saven and J. L. Skinner. A molecular theory of the line shape: Inhomogeneous and homogeneous electronic spectra of dilute chromophores in nonpolar fluids. *J. Chem. Phys.*, 99(6):4391–4402, 1993.

[163] Ryogo Kubo. *A Stochastic Theory of Line Shape*, pages 101–127. John Wiley & Sons, Inc., 1969.

[164] J. Tang and A. C. Albrecht. Studies in raman intensity theory. *J. Chem. Phys.*, 49(3):1144–1154, 1968.

[165] Andreas C. Albrecht. On the theory of raman intensities. *J. Chem. Phys.*, 34(5):1476–1484, 1961.

[166] H. Szymanski. *Raman Spectroscopy: Theory and Practice*. Springer US, 1967.

[167] E. Runge and E. K. U. Gross. Density-functional theory for time-dependent systems. *Phys. Rev. Lett.*, 52(12):9971–1000, 1984.

[168] Mark E Casida. *Time-dependent Density Functional Response Theory For Molecules.*, volume 1. World Scientific: Singapore, 1995.

[169] Andreas Dreuw and Martin Head-Gordon. Single-reference ab initio methods for the calculation of excited states of large molecules. *Chem. Rev.*, 105(11):4009–4037, 2005.

[170] Jürgen Plötner, David J Tozer, and Andreas Dreuw. Dependence of excited state potential energy surfaces on the spatial overlap of the Kohn-Sham orbitals and the amount of nonlocal Hartree-Fock exchange in time-dependent density functional theory. *J. Chem. Theor. Comput.*, 6(8):2315–2324, 2010.

[171] Mark E Casida. Propagator corrections to adiabatic time-dependent density-functional theory linear response theory. *J. Chem. Phys.*, 122:054111, 2005.

[172] Oleg A Vydrov and Troy Van Voorhis. Nonlocal van der Waals density functional: The simpler the better. *J. Chem. Phys.*, 133:244103, 2010.

[173] T Daniel Crawford and HF Schaefer. An introduction to coupled cluster theory for computational chemists. *Rev. Comput. Chem.*, 14:33–136, 2000.

[174] Isaiah Shavitt and Rodney J Bartlett. *Many-body Methods in Chemistry and Physics: MBPT and Coupled-cluster Theory*. Cambridge University Press, 2009.

[175] Hendrik J Monkhorst. Calculation of properties with the coupled-cluster method. *Int. J. Quant. Chem.*, 12(S11):421–432, 1977.

[176] Esper Dalgaard and Hendrik J Monkhorst. Some aspects of the time-dependent coupled-cluster approach to dynamic response functions. *Phys. Rev. A*, 28(3):1217, 1983.

[177] Henrik Koch and Poul Jörgensen. Coupled cluster response functions. *J. Chem. Phys.*, 93:3333, 1990.

[178] Henrik Koch, Hans Jørgen Aa. Jensen, Poul Jørgensen, Trygve Helgaker, et al. Excitation energies from the coupled cluster singles and doubles linear response function (CCSDLR). applications to Be, CH+, CO, and H2O. *J. Chem. Phys.*, 93(5):3345–3350, 1990.

[179] Henrik Koch, Rika Kobayashi, Alfredo Sanchez de Merás, and Poul Jørgensen. Calculation of size-intensive transition moments from the coupled cluster singles and doubles linear response function. *J. Chem. Phys.*, 100(6):4393–4400, 1994.

[180] John F Stanton and Rodney J Bartlett. The equation of motion coupled-cluster method. A systematic biorthogonal approach to molecular excitation energies, transition probabilities, and excited state properties. *J. Chem. Phys.*, 98:7029, 1993.

[181] H Nakatsuji, K Ohta, and K Hirao. Cluster expansion of the wave function. electron correlations in the ground state, valence and rydberg excited states, ionized states, and electron attached states of formaldehyde by SAC and SAC-CI theories. *J. Chem. Phys.*, 75:2952, 1981.

[182] K Emrich. An extension of the coupled cluster formalism to excited states: II. Approximations and tests. *Nucl. Phys. A*, 351(3):397–438, 1981.

[183] Hideo Sekino and Rodney J Bartlett. A linear response, coupled-cluster theory for excitation energy. *Int. J. Quant. Chem.*, 26(S18):255–265, 1984.

[184] Donald C Comeau and Rodney J Barlett. The equation-of-motion coupled-cluster method. applications to open-and closed-shell reference states. *Chem. Phys. Lett.*, 207(4):414–423, 1993.

[185] Ove Christiansen, Henrik Koch, and Poul Jörgensen. The second-order approximate coupled cluster singles and doubles model CC2. *Chem. Phys. Lett.*, 243(5):409–418, 1995.

[186] Martin Head-Gordon, Manabu Oumi, and David Maurice. Quasidegenerate second-order perturbation corrections to single-excitation configuration interaction. *Mol. Phys.*, 96(4):593–602, 1999.

[187] John F Stanton and Jürgen Gauss. Perturbative treatment of the similarity transformed Hamiltonian in equation-of-motion coupled-cluster approximations. *J. Chem. Phys.*, 103:1064, 1995.

[188] Steven R Gwaltney, Marcel Nooijen, and Rodney J Bartlett. Simplified methods for equation-of-motion coupled-cluster excited state calculations. *Chem. Phys. Lett.*, 248(3):189–198, 1996.

[189] Ernest R Davidson. The iterative calculation of a few of the lowest eigenvalues and corresponding eigenvectors of large real-symmetric matrices. *J. Comput. Phys.*, 17(1):87–94, 1975.

[190] K Hirao and H Nakatsuji. A generalization of the Davidson's method to large nonsymmetric eigenvalue problems. *J. Comput. Phys.*, 45(2):246–254, 1982.

[191] Marco Caricato, Gary W Trucks, and Michael J Frisch. A comparison of three variants of the generalized Davidson algorithm for the partial diagonalization of large non-Hermitian matrices. *J. Chem. Theor. Comput.*, 6(7):1966–1970, 2010.

[192] Sten Rettrup. An iterative method for calculating several of the extreme eigensolutions of large real non-symmetric matrices. *J. Comput. Phys.*, 45(1):100–107, 1982.

[193] M Caricato, G. W. Trucks, and M. J. Frisch. On the difference between the transition properties calculated with linear-response and equation-of- motion-CCSD approaches. *J. Chem. Phys.*, 131:174104, 2009.

[194] Steven R Gwaltney and Rodney J Bartlett. Gradients for the partitioned equation-of-motion coupled-cluster method. *J. Chem. Phys.*, 110(1):62–71, 1999.

[195] Per-Olov Löwdin. Studies in perturbation theory: Part I. an elementary iteration-variation procedure for solving the Schrödinger equation by partitioning technique. *J. Mol. Struct.*, 10(1):12–33, 1963.

[196] So Hirata, Peng-Dong Fan, Toru Shiozaki, and Yasuteru Shigeta. *Single-Reference Methods for Excited States In Molecules and Polymers*, pages 15–64. Springer, 2008.

[197] Martin Head-Gordon, Rudolph J Rico, Manabu Oumi, and Timothy J Lee. A doubles correction to electronic excited states from configuration interaction in the space of single substitutions. *Chem. Phys. Lett.*, 219(1):21–29, 1994.

[198] Henrik Koch, Ove Christiansen, Poul Jørgensen, Alfredo M Sanchez de Merás, and Trygve Helgaker. The CC3 model: An iterative coupled cluster approach including connected triples. *J. Chem. Phys.*, 106(5):1808–1818, 1997.

[199] M. J. Frisch, G. W. Trucks, H. B. Schlegel, G. E. Scuseria, M. A. Robb, J. R. Cheeseman, G. Scalmani, V. Barone, B. Mennucci, G. A. Petersson, H. Nakatsuji, M. Caricato, X. Li, H. P. Hratchian, A. F. Izmaylov, J. Bloino, G. Zheng, J. L. Sonnenberg, W. Liang, M. Hada, M. Ehara, K. Toyota, R. Fukuda, J. Hasegawa, M. Ishida, T. Nakajima, Y. Honda, O. Kitao, H. Nakai, T. Vreven, Jr. J. A. Montgomery, J. E. Peralta, F. Ogliaro, M. Bearpark, J. J. Heyd, E. Brothers, K. N. Kudin, V. N. Staroverov, T. Keith, R. Kobayashi, J. Normand, K. Raghavachari, A. Rendell, J. C. Burant, S. S. Iyengar, J. Tomasi, M. Cossi, N. Rega, J. M. Millam, M. Klene, J. E. Knox, J. B. Cross, V. Bakken, C. Adamo, J. Jaramillo, R. Gomperts, R. E. Stratmann, O. Yazyev, A. J. Austin, R. Cammi, C. Pomelli, J. W. Ochterski, R. L. Martin, K. Morokuma, V. G. Zakrzewski, G. A. Voth, P. Salvador, J. J. Dannenberg, S. Dapprich, P. V. Parandekar, N. J. Mayhall, A. D. Daniels, Ö. Farkas, J. B. Foresman, J. V. Ortiz, J. Cioslowski, and D. J. Fox. Gaussian Development Version Revision H.21. Gaussian Inc., Wallingford CT 2012.

[200] Marco Caricato, Gary W Trucks, Michael J Frisch, and Kenneth B Wiberg. Oscillator strength: How does TDDFT compare to EOM-CCSD? *J. Chem. Theor. Comput.*, 7(2):456–466, 2010.

[201] Marco Caricato, Gary W Trucks, Michael J Frisch, and Kenneth B Wiberg. Electronic transition energies: A study of the performance of a large range of single reference density functional and wave function methods on valence and Rydberg states compared to experiment. *J. Chem. Theor. Comput.*, 6(2):370–383, 2010.

[202] Kenneth B Wiberg, Anselmo E de Oliveira, and Gary Trucks. A comparison of the electronic transition energies for ethene, isobutene, formaldehyde, and acetone calculated using RPA, TDDFT, and EOM-CCSD. effect of basis sets. *J. Phys. Chem. A*, 106(16):4192–4199, 2002.

[203] Marko Schreiber, Mario R Silva-Junior, Stephan PA Sauer, and Walter Thiel. Benchmarks for electronically excited states: CASPT2, CC2, CCSD, and CC3. *J. Chem. Phys.*, 128(13):134110, 2008.

[204] Dániel Kánnár and Péter G Szalay. Benchmarking coupled cluster methods on valence singlet excited states. *J. Chem. Theor. Comput.*, 10(9):3757–3765, 2014.

[205] Attila Szabo and Neil S. Ostlund. *Modern Quantum Chemistry: Introduction to Advanced Electronic Structure Theory*. Dover Publications, Mineola, N.Y., 1996.

[206] R. McWeeny. *Methods of Molecular Quantum Mechanics*. Academic, New York, 1989.

[207] Wulf Rossmann. *Lie groups: an introduction through linear groups*, volume 5. Oxford University Press, 2002.

Appendix A

BRIEF OUTLINE OF (GENERALIZED) HARTREE-FOCK THEORY

In the Hartree-Fock approximation, the goal is to minimize the energy of the molecular electronic Hamiltonian (*vide infra*) within the frozen-nuclei (or Born-Oppenheimer) approximation, where the wave function is approximated by a single Slater determinant.[205] In other words, if we represent the N-electron wave function as a single Slater determinant ψ composed of N spin orbitals, $\{\psi_k(\mathbf{x})\}$

$$\psi = \frac{1}{\sqrt{N!}} \begin{vmatrix} \psi_1(\mathbf{x}_1) & \psi_2(\mathbf{x}_1) & \dots & \psi_N(\mathbf{x}_1) \\ \psi_1(\mathbf{x}_2) & \psi_2(\mathbf{x}_2) & \dots & \psi_N(\mathbf{x}_2) \\ \vdots & \vdots & \ddots & \vdots \\ \psi_1(\mathbf{x}_N) & \psi_2(\mathbf{x}_N) & \dots & \psi_N(\mathbf{x}_N) \end{vmatrix} \tag{A.1}$$

where the variable $\mathbf{x}$ includes both the spatial coordinate $\mathbf{r}$ and the discrete spin coordinate m_s for one electron. In generalized Hartree-Fock (GHF), and in order to allow for non-collinearity, we express the spin orbitals as a two-component spinor,

$$\psi_k(\mathbf{x}) = \begin{pmatrix} \phi_k^{\alpha}(\mathbf{r}) \\ \phi_k^{\beta}(\mathbf{r}) \end{pmatrix} \tag{A.2}$$

where the spatial functions $\{\phi_k^{\alpha}(\mathbf{r})\}$, $\{\phi_k^{\beta}(\mathbf{r})\}$ are expanded in terms of a common set of real atomic orbital (AO) basis functions $\{\chi_\mu(\mathbf{r})\}$ with coefficients $C_{\mu k}^{\tau}$ where τ denotes the spin

coordinate

$$\phi_k^{\alpha}(\mathbf{r}) = \sum_{\mu} C_{\mu k}^{\alpha} \chi_{\mu}(\mathbf{r}) \tag{A.3}$$

$$\phi_k^{\beta}(\mathbf{r}) = \sum_{\mu} C_{\mu k}^{\beta} \chi_{\mu}(\mathbf{r}) \tag{A.4}$$

Regardless of the representation of the wave function, the molecular electronic Hamiltonian has the same definition (in atomic units)

$$\hat{H} = -\sum_i \frac{1}{2}\nabla_i^2 - \sum_{i,A} \frac{Z_A}{r_{iA}} + \sum_{i>j} \frac{1}{r_{ij}} + \sum_{B>A} \frac{Z_A Z_B}{R_{AB}} \tag{A.5}$$

where i, j and A, B indicate indices of electrons and nuclei, respectively. The first term is the sum of the kinetic energies of the electrons, the second accounts for the interaction between an electron and a nuclei of charge Z_A separated by r_{iA}, the third is analogous to the second and accounts for repulsion between two electrons. The fourth term accounts for repulsion between nuclei. Note that nuclear kinetic energy is set to zero, as we work within the Born-Oppenheimer approximation.

Given Eq. (A.1) and Eq. (A.5), HF theory seeks to minimize the energy of

$$E = \int d\mathbf{x}\, \psi^*(\mathbf{x})\, \hat{H}\, \psi(\mathbf{x}) = \langle \psi | \hat{H} | \psi \rangle \tag{A.6}$$

Given any single Slater determinant ψ, we can obtain a new single Slater determinant ψ' by performing a rotation among the basis coefficients,

$$\psi' = \exp(\boldsymbol{\kappa})\psi \tag{A.7}$$

where $\boldsymbol{\kappa}$ is a single excitation operator, that is,

$$\boldsymbol{\kappa} = \sum_{i,a} \kappa_i^a a_a^\dagger a_i \tag{A.8}$$

and the indexes i and a index over occupied and virtual orbitals, respectively. Thus $a_a^\dagger a_i$ is a single excitation operator in the second quantized notation.[205] Furthermore $\boldsymbol{\kappa}$ is anti-Hermitian, that is to say $\boldsymbol{\kappa}^\dagger = -\boldsymbol{\kappa}$, and, to be a rotation, $\exp(\boldsymbol{\kappa})$ is unitary. For a given basis, any single Slater determinant can be generated from any other single Slater determinant through a rotation by some given $\exp(\boldsymbol{\kappa})$. In Appendix C we will show that $\boldsymbol{\kappa}$ is only defined over the space of single excitations.

In Chapter 2 we showed that the the first variation of the energy of a single Slater determinant with respect to orbital rotation coefficients κ_i^a yields the condition that

$$\frac{\partial E}{\partial \kappa_i^a} = \begin{pmatrix} \langle \psi_i^a | \hat{H} | \psi_0 \rangle \\ \langle \psi_0 | \hat{H} | \psi_i^a \rangle \end{pmatrix} = \begin{pmatrix} F_{ai} \\ F_{ia} \end{pmatrix} = \begin{pmatrix} 0 \\ 0 \end{pmatrix} \tag{A.9}$$

which must equal zero if the energy functional is minimized. Here ψ_0 is our reference determinant (e.g. ψ_0 equals the ψ which minimizes E in Eq. (A.6)) , and ψ_i^a is our reference with the occupation of orbital i replaced with the occupation of virtual orbital a, e.g. a single orbital excitation of the reference Slater determinant. Thus $\langle \psi_0 | H | \psi_i^a \rangle \equiv F_{ia} = 0$, along with its conjugate transpose. From the Slater-Condon rules[205] we can identify F_{pq} (p and q are general orbital indices) as

$$F_{pq} \equiv \langle p|h|q\rangle + \sum_i^N \langle pi||qj\rangle \tag{A.10}$$

which is the so-called Fock operator. Here we have used the shorthand notation that

$$\langle p|h|q\rangle = \int d\mathbf{x_1}\, \phi_p^*(\mathbf{x}_1) \left(-\frac{1}{2}\nabla_1^2 - \sum_A \frac{Z_A}{r_{1A}} \right) \phi_q(\mathbf{x}_1) \tag{A.11}$$

and

$$\langle pi||qi\rangle = \langle pi|qi\rangle - \langle pi|iq\rangle \tag{A.12}$$

with the general

$$\langle ij|kl\rangle = \big(ik|jl\big) = \int\int d\mathbf{x}_1 d\mathbf{x}_2\, \phi_i^*(\mathbf{x}_1)\phi_j^*(\mathbf{x}_2)\mathbf{r}_{12}^{-1}\phi_k(\mathbf{x}_1)\phi_l(\mathbf{x}_2) \tag{A.13}$$

where the sum in Eq. (A.10) is over N occupied orbitals indexed by i. Since by Eq. (A.9) we must have $F_{ia} = F_{ai} = 0$, it follows that it is sufficient to find the basis for $\mathbf{F}$ in which $\mathbf{F}$ is diagonal. This leads to the so-called Hartree-Fock eigenvalue equation

$$\mathbf{FC} = \mathbf{CE} \tag{A.14}$$

where $\mathbf{C}$ is the matrix of orbital coefficients that diagonalize $\mathbf{F}$ (the eigenvectors) with corresponding eigenvalues collected in the diagonal $\mathbf{E}$. These eigenvalues are often interpreted as orbital energies, which is to say they are the mean-field energies of single electrons in the approximate N-electron wave function. Because $\mathbf{F}$ depends on the values of $\mathbf{C}$ (Eq. (A.10)), a single diagonalization is not sufficient to find the global minimum. We reform $\mathbf{F}$ after each diagonalization in Eq. (A.14), and iterate until energy stops changing. This is the condition of self-consistency, where self-consistent field methods get their name. In most practical cases we do not represent our trial wave function in an orthonormal basis, so that $\mathbf{C}^\dagger\mathbf{C} \neq \mathbf{I}$. However, we can incorporate a new metric — the overlap, or normalization, of our basis functions — as a matrix $\mathbf{S}$ which yields the Roothaan-Hall equations

$$\mathbf{FC} = \mathbf{SCE} \tag{A.15}$$

satisfying the orthonormality constraint that

$$\mathbf{C}^\dagger\mathbf{SC} = \mathbf{I} \tag{A.16}$$

with $S_{pq} = \langle\phi_p|\phi_q\rangle$. The previous discussion has made no assumption on the form of the basis functions. If we are to work within the generalized Hartree-Fock approximation (for

a pedagogical overview see Reference 206), where we enforce the spin symmetry (or lack thereof) according to Eq. (A.2), then the matrix form of the density operator

$$P_{\mu\nu}^{\sigma\tau} = \sum_{i}^{N} C_{\mu i}^{\sigma} \cdot C_{\nu i}^{\tau *} \tag{A.17}$$

has the spin-blocked structure, where σ and τ are used as spin variables ($\sigma \in \{\alpha, \beta\}; \tau \in \{\alpha, \beta\}$),

$$\mathbf{P} = \begin{pmatrix} \mathbf{P}^{\alpha\alpha} & \mathbf{P}^{\alpha\beta} \\ \mathbf{P}^{\beta\alpha} & \mathbf{P}^{\beta\beta} \end{pmatrix} \tag{A.18}$$

And similarly the Fock matrix

$$\mathbf{F} = \begin{pmatrix} \mathbf{F}^{\alpha\alpha} & \mathbf{F}^{\alpha\beta} \\ \mathbf{F}^{\beta\alpha} & \mathbf{F}^{\beta\beta} \end{pmatrix} \tag{A.19}$$

where each spin block $\mathbf{F}^{\sigma\tau}$ is given by

$$\mathbf{F}^{\sigma\tau} = \mathbf{h}^{\sigma\tau} + \delta_{\sigma\tau} \left[\mathbf{J}^{\alpha\alpha} + \mathbf{J}^{\beta\beta} \right] - \mathbf{K}^{\sigma\tau} \tag{A.20}$$

where $\mathbf{h}^{\sigma\tau}$ is the one-electron Hamiltonian matrix and $\mathbf{J}^{\sigma\tau}$ and $\mathbf{K}^{\sigma\tau}$ are Coulomb and exchange matrices, respectively, obtained by replacing $\phi_k(\mathbf{x})$ from Eq. (A.2) with its basis set expansion

in terms of real AO basis functions in Eq. (A.3), so that

$$
\begin{aligned}
J^{\sigma\sigma}_{\mu\nu} \equiv \langle\mu|\hat{J}^{\sigma\sigma}|\nu\rangle &= \sum_{j}^{N} \int d\mathbf{r}_1 d\mathbf{r}_2 \chi^*_\mu(\mathbf{r}_1)\phi^{\sigma *}_j(\mathbf{r}_2)\mathbf{r}_{12}^{-1}\phi^{\sigma}_j(\mathbf{r}_2)\chi_\nu(\mathbf{r}_1) \\
&= \sum_{j}^{N}\sum_{\lambda\kappa} C^{\sigma}_{\lambda j}\cdot C^{\sigma *}_{\kappa j} \int d\mathbf{r}_1 d\mathbf{r}_2 \chi^*_\mu(\mathbf{r}_1)\chi^*_\kappa(\mathbf{r}_2)\mathbf{r}_{12}^{-1}\chi_\lambda(\mathbf{r}2)\chi_\nu(\mathbf{r}_1) \\
&= \sum_{\lambda\kappa} P^{\sigma\sigma}_{\lambda\kappa}\cdot\big(\mu\nu|\kappa\lambda\big) \qquad \text{(A.21)} \\
K^{\sigma\tau}_{\mu\nu} \equiv \langle\mu|\hat{K}^{\sigma\tau}|\nu\rangle &= \sum_{j}^{N} \int d\mathbf{r}_1 d\mathbf{r}_2 \chi^*_\mu(\mathbf{r}_1)\phi^{\tau *}_j(\mathbf{r}_2)\mathbf{r}_{12}^{-1}\chi_\nu(\mathbf{r}_2)\phi^{\sigma}_j(\mathbf{r}_1) \\
&= \sum_{j}^{N}\sum_{\lambda\kappa} C^{\sigma}_{\lambda j}\cdot C^{\tau *}_{\kappa j} \int d\mathbf{r}_1 d\mathbf{r}_2 \chi^*_\mu(\mathbf{r}_1)\chi^*_\kappa(\mathbf{r}_2)\mathbf{r}_{12}^{-1}\chi_\nu(\mathbf{r}_2)\chi_\lambda(\mathbf{r}_1) \\
&= \sum_{\lambda\kappa} P^{\sigma\tau}_{\lambda\kappa}\cdot\big(\mu\lambda|\kappa\nu\big) \qquad \text{(A.22)}
\end{aligned}
$$

Appendix B

BROKEN SYMMETRIES IN THE HARTREE-FOCK MODEL

We want to classify broken-symmetry wave functions[4,22] by investigating how they transform under the action of the invariance operators $\hat{g}$ constituting the symmetry group $\mathcal{G}$ of the non-relativistic electronic Hamiltonian $\hat{H}$, i.e.

$$[\hat{g}, \hat{H}] = 0, \qquad (\forall \hat{g} \in \mathcal{G}) \tag{B.1}$$

which is equivalent to

$$\hat{g}\hat{H}\hat{g}^{-1} = \hat{H}, \qquad (\forall \hat{g} \in \mathcal{G}). \tag{B.2}$$

This means $\hat{H}$ is invariant to transformation by $\hat{g}$, whatever $\hat{g}$ may be. In general, when $|\psi\rangle$ is an eigenstate of $\hat{H}$, then $\hat{g}$ and $\hat{H}$ share a common eigenbasis.

Now, exact eigenstates of $\hat{H}$ can be chosen to be simultaneous eigenstates of the various symmetries in $\mathcal{G}$. In contrast, for approximate variational wave functions (e.g. Hartree-Fock) the symmetry requirements represent additional constraints. Löwdin's "symmetry dilemma".[2] To state this dilemma again, we know the exact solution (lowest-energy solution) will have certain symmetries, but if we include these symmetries in our approximate, variational Hamiltonian, we can only raise the energy and not lower it. This means we can get closer to the exact solution by removing physical constraints, which is problematic. This is troublesome, but not a huge deal in practice. It is crucial to recognize that this problem arises only because we use an approximate independent-particle Hamiltonian.

There are several ways to break the single-determinant Hartree-Fock model into its various broken-symmetry subgroups. However this is done, the ultimate goal is to determine is the form of the operators $\hat{A}$ that are invariant with respect to similarity transformations by

various subgroups $\mathcal{H} \subset \mathcal{G}$, i.e.

$$\hat{h}\hat{A}\hat{h}^{-1} = \hat{A}, \qquad (\forall \hat{h} \in \mathcal{H} \subset \mathcal{G}) \tag{B.3}$$

For ease of analysis, we put $\hat{A}$ into a finite basis and treat this problem with the tools of linear algebra. The basis for our independent-particle model will be the spinor basis,

$$|\alpha\rangle = \begin{pmatrix} 1 \\ 0 \end{pmatrix}, \qquad |\beta\rangle = \begin{pmatrix} 0 \\ 1 \end{pmatrix}, \qquad \text{and} \quad |\alpha\rangle\langle\alpha| = |\beta\rangle\langle\beta| = \mathbf{I}_2 \tag{B.4}$$

so any arbitrary spin function can be written

$$|p\rangle = p_1|\alpha\rangle + p_2|\beta\rangle = \begin{pmatrix} p_1 \\ p_2 \end{pmatrix} \tag{B.5}$$

We will only worry about one-body operators $\hat{A}$, which include the Fock operator as well as the unitary parameterization of the single determinant (see the Thouless representation in Appendix C). Putting $\hat{A}$ into a spinor basis gives us

$$\hat{A} = |i\sigma_1\rangle\langle i\sigma_1|\hat{A}|j\sigma_2\rangle\langle j\sigma_2| = A_{i\sigma_1,j\sigma_2}|i\sigma_1\rangle\langle j\sigma_2| = \begin{pmatrix} \mathbf{A}_{\alpha\alpha} & \mathbf{A}_{\alpha\beta} \\ \mathbf{A}_{\beta\alpha} & \mathbf{A}_{\beta\beta} \end{pmatrix} \tag{B.6}$$

with

$$(A_{\sigma_1\sigma_2})_{ij} \in \mathbb{C} \quad \text{and} \quad \sigma_1, \sigma_2 \in \alpha, \beta \tag{B.7}$$

Or, rewritten in second quantized notation

$$\hat{A} = \sum_{ij} \sum_{\sigma_1,\sigma_2} A_{i\sigma_1,j\sigma_2} a^\dagger_{i\sigma_1} a_{j\sigma_2} = \sum_{ij} \sum_{\sigma_1,\sigma_2} A_{i\sigma_1,j\sigma_2} \hat{E}^{i\sigma_1}_{j\sigma_2} \tag{B.8}$$

The transformation properties of $\hat{A}$ under symmetry operations can be determined by

examining the transformation of the $U(2n)$ generators $\hat{E}^{i\sigma_1}_{j\sigma_2}$, but it is simpler to consider the transformations of the 2×2 (block) matrix $\mathbf{A}$, e.g.

$$\hat{h} \begin{pmatrix} \mathbf{A}_{\alpha\alpha} & \mathbf{A}_{\alpha\beta} \\ \mathbf{A}_{\beta\alpha} & \mathbf{A}_{\beta\beta} \end{pmatrix} \hat{h}^{-1} = \begin{pmatrix} \mathbf{A}_{\alpha\alpha} & \mathbf{A}_{\alpha\beta} \\ \mathbf{A}_{\beta\alpha} & \mathbf{A}_{\beta\beta} \end{pmatrix} \tag{B.9}$$

Thus, we are looking for the constraints on $\mathbf{A}$ that make the above equation true, for any given symmetry operation.

The general invariance group of the spin-free electronic Hamiltonian involves the spin rotation group SU(2) and the time reversal group $\mathcal{T}$, i.e. SU(2) $\otimes\mathcal{T}$. SU(2) can be given in terms of spin operators,

$$\mathrm{SU}(2) = \{U_R(\vec{n}, \theta) = \exp(i\theta \sum_{a=1}^{3} \hat{S}_a \hat{n}_a); \vec{n} = (n_1, n_2, n_3); \vec{n} \in \mathbb{R}^3; ||\vec{n}|| = 1, \theta \in (-2\pi, 2\pi]\} \tag{B.10}$$

this amounts to performing rotations in spin space. The time reversal group is given as

$$\mathcal{T} = \{\pm\hat{1}, \pm\hat{\Theta}\} \tag{B.11}$$

In general,

$$\hat{\Theta} = \hat{U}_R(\vec{e}_2, -\pi)\hat{K} = \exp(-i\pi\hat{S}_2)\hat{K} \tag{B.12}$$

$$\hat{\Theta}^{-1} = -\hat{\Theta} = \exp(i\pi\hat{S}_2)\hat{K} \tag{B.13}$$

where $\hat{K}$ is the complex conjugation operator. Time reversal changes the direction of motion, be it linear momentum or angular momentum. It is an antiunitary operator (it must be, in fact) that consists of the Pauli matrix operator (unitary) and the complex conjugation operator (antiunitary), to be antiunitary overall. It affects electrons by flipping their spin and then taking the complex conjugate. Finally, we observe that since SU(2) is a double cover, if we rotate in spin space by 2π, we flip the sign of the wave function. If we rotate by another

2π, we get the original state back. This is characteristic of the fermionic nature of electrons.

Let us now consider the unitary transformations of the form $U = \exp(i\hat{B})$ where $\hat{B} = \hat{B}^\dagger$, acting on some operator $\hat{A}$.This is valid for any unitary transformation that depends on a continuous parameter (which we have absorbed into $\hat{B}$). We insist

$$\hat{A} = \hat{U}\hat{A}\hat{U}^{-1} = e^{(-i\hat{B})}\hat{A}e^{(i\hat{B})} \tag{B.14}$$

Now, by the Baker-Campbell-Hausdorff transformation,[207] we can rewrite the right hand side as

$$e^{(-i\hat{B})}\hat{A}e^{(i\hat{B})} = \hat{A} + \left[\hat{A}, i\hat{B}\right] + \frac{1}{2!}\left[\left[\hat{A}, i\hat{B}\right], i\hat{B}\right] + \cdots \tag{B.15}$$

Since by definition $\hat{A} = e^{(-i\hat{B})}\hat{A}e^{(i\hat{B})}$ it suffices to show that the constraints on $\hat{A}$ introduced by the symmetry operation are satisfied when $\left[\hat{A}, i\hat{B}\right] = 0$.

This means that we can look at how the 2×2 matrix $\mathbf{A}$ transforms under the Pauli spin matrices which define the SU(2) spin rotation as well as the time-reversal operation (in the time-reversal case, we can use the BCH expansion of the unitary part $\hat{S}_y$ and then absorb the complex conjugation into the commutator expression). We can show how RHF, UHF, and GHF are all the result of different symmetry combinations (or lack thereof). From here on, we drop the hats on the operators for clarity.

To begin we consider how many different types of symmetry subgroups we can have. From the form of the spin rotation and time-reversal groups we can obtain the following subgroups:

1. $\mathcal{E}$. No symmetry, e.g. invariant to generator $\mathbf{I}$.

2. $\mathcal{T}$. Time-reveral symmetry, e.g. invariant to generator Θ.

3. $\mathcal{K}$. Complex-conjugation symmetry, e.g. invariant to generator K.

4. $\mathcal{A}$. Symmetric to axial spin rotations, e.g. invariant to generator S_z.

5. $\mathcal{A} \otimes \mathcal{K}$. Symmetric to axial spin rotations and complex-conjugation, e.g. invariant to generators S_z and K.

6. $\mathcal{A} \otimes \mathcal{T}$. Symmetric to axial spin rotations and time-reversal symmetry, e.g. invariant to generators S_z and Θ.

7. SU(2). Symmetric to all spin rotations, e.g. invariant to generators S_x, S_y, and S_z.

8. SU(2) $\otimes \mathcal{T}$. Symmetric all spin rotations and time-reversal, e.g. invariant to generators S_x, S_y, S_z, and Θ.

This exhausts all possible combinations. Now we can examine each group case by case, using the (2×2) complex Fock matrix as our primary object of manipulation, i.e.

$$\begin{pmatrix} \mathbf{F}_{\alpha\alpha} & \mathbf{F}_{\alpha\beta} \\ \mathbf{F}_{\beta\alpha} & \mathbf{F}_{\beta\beta} \end{pmatrix} \tag{B.16}$$

Where we solve, for each symmetry (or group of symmetries),

$$\mathbf{h} \begin{pmatrix} \mathbf{F}_{\alpha\alpha} & \mathbf{F}_{\alpha\beta} \\ \mathbf{F}_{\beta\alpha} & \mathbf{F}_{\beta\beta} \end{pmatrix} \mathbf{h}^{-1} = \begin{pmatrix} \mathbf{F}_{\alpha\alpha} & \mathbf{F}_{\alpha\beta} \\ \mathbf{F}_{\beta\alpha} & \mathbf{F}_{\beta\beta} \end{pmatrix} \tag{B.17}$$

where $\mathbf{h}$ is the generator of the symmetry.

$\mathcal{E}$. No symmetry.

In this case, our transformation on $\mathbf{F}$ is rather simple. It looks like

$$\mathbf{I} \begin{pmatrix} \mathbf{F}_{\alpha\alpha} & \mathbf{F}_{\alpha\beta} \\ \mathbf{F}_{\beta\alpha} & \mathbf{F}_{\beta\beta} \end{pmatrix} \mathbf{I}^{-1} = \begin{pmatrix} \mathbf{F}_{\alpha\alpha} & \mathbf{F}_{\alpha\beta} \\ \mathbf{F}_{\beta\alpha} & \mathbf{F}_{\beta\beta} \end{pmatrix} \tag{B.18}$$

So we get no constraints. We can mix spin, as well as take on complex values. This is the structure of the complex generalized Hartree-Fock (GHF) Fock matrix.

$\mathcal{K}$. Complex conjugation symmetry.

If the only symmetry that holds is complex conjugation, our transformation looks like

$$K \begin{pmatrix} \mathbf{F}_{\alpha\alpha} & \mathbf{F}_{\alpha\beta} \\ \mathbf{F}_{\beta\alpha} & \mathbf{F}_{\beta\beta} \end{pmatrix} K = \begin{pmatrix} \mathbf{F}^*_{\alpha\alpha} & \mathbf{F}^*_{\alpha\beta} \\ \mathbf{F}^*_{\beta\alpha} & \mathbf{F}^*_{\beta\beta} \end{pmatrix} \tag{B.19}$$

Note that K is its own inverse. It also only acts to either the left or the right. The asterisk indicates complex conjugation (not an adjoint). The constraint we get here is that the values of the Fock matrix have to be identical on complex conjugation. Since this can only happen if the values are real, we get the real GHF Fock equations.

$\mathcal{T}$. Time reversal symmetry.

Now we start to get slightly more complicated. Using the Pauli matrix

$$\sigma_2 = \begin{pmatrix} 0 & -i \\ i & 0 \end{pmatrix} \tag{B.20}$$

to represent the unitary S_2 operation, we obtain

$$-i \begin{pmatrix} 0 & -i \\ i & 0 \end{pmatrix} K \begin{pmatrix} \mathbf{F}_{\alpha\alpha} & \mathbf{F}_{\alpha\beta} \\ \mathbf{F}_{\beta\alpha} & \mathbf{F}_{\beta\beta} \end{pmatrix} iK \begin{pmatrix} 0 & i \\ -i & 0 \end{pmatrix} = \begin{pmatrix} \mathbf{F}^*_{\beta\beta} & -\mathbf{F}^*_{\beta\alpha} \\ -\mathbf{F}^*_{\alpha\beta} & \mathbf{F}^*_{\alpha\alpha} \end{pmatrix}. \tag{B.21}$$

This really only introduces two constraints, so we choose to eliminate $\mathbf{F}_{\beta\alpha}$ and $\mathbf{F}_{\beta\beta}$. This gives the final result of paired GHF, or

$$\begin{pmatrix} \mathbf{F}_{\alpha\alpha} & \mathbf{F}_{\alpha\beta} \\ -\mathbf{F}^*_{\alpha\beta} & \mathbf{F}^*_{\alpha\alpha} \end{pmatrix} \tag{B.22}$$

$\mathcal{A}$. Axial spin symmetry, e.g. rotation about spin z-axis.

Here we use the Pauli matrix

$$\sigma_3 = \begin{pmatrix} 1 & 0 \\ 0 & -1 \end{pmatrix} \tag{B.23}$$

And show that

$$\begin{pmatrix} 1 & 0 \\ 0 & -1 \end{pmatrix} \begin{pmatrix} \mathbf{F}_{\alpha\alpha} & \mathbf{F}_{\alpha\beta} \\ \mathbf{F}_{\beta\alpha} & \mathbf{F}_{\beta\beta} \end{pmatrix} \begin{pmatrix} 1 & 0 \\ 0 & -1 \end{pmatrix} = \begin{pmatrix} \mathbf{F}_{\alpha\alpha} & -\mathbf{F}_{\alpha\beta} \\ -\mathbf{F}_{\beta\alpha} & \mathbf{F}_{\beta\beta} \end{pmatrix} \tag{B.24}$$

which is only satisfied if

$$\mathbf{F} = \begin{pmatrix} \mathbf{F}_{\alpha\alpha} & \mathbf{0} \\ \mathbf{0} & \mathbf{F}_{\beta\beta} \end{pmatrix} \tag{B.25}$$

This gives us the complex version of UHF. We see invariance with respect to S_z results in two separate spin blocks, with no restriction on whether they take real or complex values, or the dimension of either spin block.

$\mathcal{A} \otimes \mathcal{T}$. Rotation about spin z-axis and time reversal.

We are now at the point where we examine the effect of invariance to multiple symmetry operations. One concern when considering multiple symmetry operations is that the order in which we perform symmetry operations matters. In general, symmetry operations do not commute, however we will see that for our purposes order does not matter. Because we insist on invariance, the multiple symmetries never actually act on each other, therefore we

don't need to consider the commutator between them. Or, put a different way, because each symmetry operation returns the system to its original state, we can consider each operation separately. The system contains no memory, so to speak, of the previous symmetry operation. We can show this another way using the BCH expansion. Consider two symmetry operations on F parameterized by "A" and "B":

$$e^{(-iA)}e^{(-iB)}Fe^{(iB)}e^{(iA)} = e^{(-iA)}[F + [F, iB] + \cdots]e^{(iA)} = e^{(-iA)}Fe^{(iA)} = [F + [F, iA] + \cdots] \tag{B.26}$$

Which is true if and only if

$$[F, iB] = [F, iA] = 0 \tag{B.27}$$

Which decouples A and B. Considering multiple symmetry operations only gives us more constraints, and order doesn't matter. Moving on to time reversal and z-axial spin symmetry. Using the results for time reversal symmetry, we have

$$\begin{pmatrix} 1 & 0 \\ 0 & -1 \end{pmatrix} \begin{pmatrix} \mathbf{F}_{\alpha\alpha} & \mathbf{F}_{\alpha\beta} \\ -\mathbf{F}^*_{\alpha\beta} & \mathbf{F}^*_{\alpha\alpha} \end{pmatrix} \begin{pmatrix} 1 & 0 \\ 0 & -1 \end{pmatrix} = \begin{pmatrix} \mathbf{F}_{\alpha\alpha} & -\mathbf{F}_{\alpha\beta} \\ \mathbf{F}^*_{\alpha\beta} & \mathbf{F}^*_{\alpha\alpha} \end{pmatrix} \tag{B.28}$$

Which means the off diagonals must go to zero, giving our final result of paired UHF,

$$\begin{pmatrix} \mathbf{F}_{\alpha\alpha} & \mathbf{0} \\ \mathbf{0} & \mathbf{F}^*_{\alpha\alpha} \end{pmatrix} \tag{B.29}$$

$\mathcal{A} \otimes \mathcal{K}$. Rotation about spin z-axis and complex conjugation.

We do a similar thing as above for rotation about spin z-axis and complex conjugation. This one is particularly easy to show, starting from the results of complex conjugation symmetry. Since symmetry with respect to K forces all matrix elements to be real, and we get the real version of the results of symmetry with respect to S_z, that is to say we get the real UHF equations.

$$\mathbf{F} = \begin{pmatrix} \mathbf{F}_{\alpha\alpha} & \mathbf{0} \\ \mathbf{0} & \mathbf{F}_{\beta\beta} \end{pmatrix}, \qquad (\mathbf{F} \in \mathbb{R}) \tag{B.30}$$

SU(2). Rotation about all spin axes.

To show invariance with respect to the spin group, it suffices just to consider any two spin rotations, since each spin operator can be generated by the commutator of the other two. You can show this using the Jacobi identity. Say we are looking the invariance of F with respect to generators A,B,and C, and $[A, B] = iC$ (like our spin matrices do). We want to show

$$[F, A] = [F, B] = 0 \implies [F, C] = 0 \tag{B.31}$$

The Jacobi identity tells us

$$[A, [B, F]] + [B, [F, A]] + [F, [A, B]] = 0 \tag{B.32}$$

Now, by definition the first two terms are zero, and we can evaluate the commutator of $[A, B] = iC$, which means if $[F, A] = [F, B] = 0$, then it must follow that $[F, C] = 0$ as well (the imaginary in front doesn't make a difference; expand to see). That being said, we can evaluate invariance with respect to all spin axes by using the results of S_z and applying the generator S_x defined by Pauli matrix σ_2 to it, where

$$\sigma_2 = \begin{pmatrix} 0 & 1 \\ 1 & 0 \end{pmatrix}. \tag{B.33}$$

Applying this gives

$$\begin{pmatrix} 0 & 1 \\ 1 & 0 \end{pmatrix} \begin{pmatrix} \mathbf{F}_{\alpha\alpha} & \mathbf{0} \\ \mathbf{0} & \mathbf{F}_{\beta\beta} \end{pmatrix} \begin{pmatrix} 0 & 1 \\ 1 & 0 \end{pmatrix} = \begin{pmatrix} \mathbf{F}_{\beta\beta} & \mathbf{0} \\ \mathbf{0} & \mathbf{F}_{\alpha\alpha} \end{pmatrix}, \tag{B.34}$$

which means that $\mathbf{F}_{\alpha\alpha} = \mathbf{F}_{\beta\beta}$, or

$$\mathbf{F} = \begin{pmatrix} \mathbf{F}_R & \mathbf{0} \\ \mathbf{0} & \mathbf{F}_R \end{pmatrix}, \qquad (\mathbf{F}_R \in \mathbb{C}). \tag{B.35}$$

Invariance in this symmetry group results in the complex RHF equations, where the alpha and beta spin blocks are equivalent. Thus orbitals are doubly occupied.

SU(2) $\otimes\mathcal{T}$. All spin rotations and time reversal.

Given the results we just obtained above, and understanding that time reversal contains the S_y operator, we only need to take the previous results and make them invariant to complex conjugation. This is very simple, and we see that

$$K \begin{pmatrix} \mathbf{F}_R & \mathbf{0} \\ \mathbf{0} & \mathbf{F}_R \end{pmatrix} K = \begin{pmatrix} \mathbf{F}_R^* & \mathbf{0} \\ \mathbf{0} & \mathbf{F}_R^* \end{pmatrix}. \tag{B.36}$$

In other words, we obtain the real RHF equations, since invariance with respect to complex conjugation forces the elements to be real.

Appendix C

PROOF OF THOULESS' THEOREM

The Thouless theorem[34] says that the effect of the $e^{\hat{T}_1}$ operator is to transform any single determinant into any other single determinant. In other words, we can write

$$|\phi\rangle = [\exp\left(\sum_{i=1}^{N}\sum_{a=N+1}^{\infty} t_i^a a_a^\dagger a_i\right)]|\phi_0\rangle \tag{C.1}$$

$$= e^{\hat{T}_1}|\phi_0\rangle \tag{C.2}$$

In this way, we can generate any single determinant in terms of another determinant with virtual orbitals (or single excitations) mixed in with it. This is often referred to as "orbital rotation". Minimizing the energy of a Slater determinant with respect to the rotation parameters (here the t_i^a amplitudes), we obtain the Hartree-Fock variational wave function. This is one manifestation the Brillouin's condition, and says that the Hartree-Fock reference will not interact (directly) with singly excited determinants. Thouless' theorem also explains why there is no such thing as a coupled cluster singles equation (as it is equivalent to the Hartree-Fock approximation. We do include single excitations in CCSD, but they enter only through contractions with higher excitations of the reference.)

Let's say we have a single N-electron Slater determinant. In second quantization this is written as

$$|\phi_0\rangle = a_1^\dagger a_2^\dagger \cdots a_N^\dagger|0\rangle = \prod_{i=1}^{N} a_i^\dagger|0\rangle \tag{C.3}$$

where N is the number of electrons in the N-electron wave function, and $|0\rangle$ is a vacuum. Let's say we know what this wave function $|\phi_0\rangle$ is, which is to say it will be our reference determinant. Now say we want to make a new single determinant $|\phi\rangle$ in terms of our reference

determinant. First we write our determinant:

$$|\phi\rangle = \tilde{a}_1^\dagger \tilde{a}_2^\dagger \cdots \tilde{a}_N^\dagger |0\rangle = \prod_{\alpha=1}^{N} \tilde{a}_\alpha^\dagger |0\rangle \tag{C.4}$$

The difference between $a^\dagger$ and $\tilde{a}^\dagger$ is simply that they create electrons in different (though not orthonormal) orbitals in our Slater determinant. We will assume that the sets of creation and annihilation operators form complete sets and are non-orthogonal with respect to each other. If this is the case, we can write one set in terms of the other like so:

$$\tilde{a}_\alpha^\dagger = \sum_{i}^{\infty} u_{\alpha i} a_i^\dagger \tag{C.5}$$

This is merely a change of basis. This suggests that we can write

$$|\phi\rangle = \prod_{\alpha=1}^{N} \tilde{a}_\alpha^\dagger |0\rangle = \prod_{\alpha=1}^{N} \left(\sum_{i}^{\infty} u_{\alpha i} a_i^\dagger \right) |0\rangle \tag{C.6}$$

Following the presentation of Thouless, we then split the sum over occupied and virtual spaces (with respect to the reference):

$$|\phi\rangle = \prod_{\alpha=1}^{N} \left(\sum_{i}^{\infty} u_{\alpha i} a_i^\dagger \right) |0\rangle = \prod_{\alpha=1}^{N} \left(\sum_{i}^{N} u_{\alpha i} a_i^\dagger + \sum_{m=N+1}^{\infty} u_{\alpha m} a_m^\dagger \right) |0\rangle \tag{C.7}$$

Since we assumed $|\phi\rangle$ and $|\phi_0\rangle$ were not orthogonal, we can choose an intermediate normalization, setting

$$\langle \phi_0 | \phi \rangle = \mathbf{1} \tag{C.8}$$

which implies that the transformation matrix composed of $u_{\alpha i}$ is unitary when α and i run from 1 to N (u is rectangular according to our change of basis definition in C.5). This means the square $N \times N$ subsection of u is invertible, and we represent its $N \times N$ inverse as $U_{i\alpha}$.

Equivalently,

$$\mathbf{uU} = \begin{bmatrix} \mathbf{u}_{(N\times N)} \\ \mathbf{u}_{N\times(N+1):\infty} \end{bmatrix} \mathbf{U} = \begin{bmatrix} \mathbf{I} \\ \mathbf{T} \end{bmatrix} \tag{C.9}$$

where

$$\mathbf{u}_{(N\times N)}\mathbf{U} = \mathbf{I} \qquad \text{or} \qquad \sum_{i=1}^{N} u_{\alpha i} U_{i\beta} = \delta_{\alpha\beta} \tag{C.10}$$

and conversely,

$$\mathbf{U}\mathbf{u}_{(N\times N)} = \mathbf{I} \qquad \text{or} \qquad \sum_{\alpha=1}^{N} U_{i\alpha} u_{\alpha j} = \delta_{ij} \tag{C.11}$$

and $\mathbf{T}$ matrix is the result of the parts of $\mathbf{u}$ that extend past the number of electrons N:

$$\mathbf{U}\mathbf{u}_{(N\times(N+1):\infty)} = \mathbf{T} \qquad \text{or} \qquad \sum_{\alpha=1}^{N} U_{i\alpha} u_{\alpha m} = t_{mi} \tag{C.12}$$

where $i \leq N$ and $m > N$ for the above equation. Because $\mathbf{U}$ is unitary, we can write N linearly independent combinations of the creation operators, each of which we'll call $\bar{a}_i^\dagger$.

$$\bar{a}_i^\dagger = \sum_{\alpha=1}^{N} U_{i\alpha} \tilde{a}_\alpha^\dagger \tag{C.13}$$

using equations C.5,C.10, C.11, and C.12 we can rewrite the above in terms of just our

reference creation and annihilation operators

$$
\begin{aligned}
\bar{a}_i^\dagger &= \sum_{\alpha=1}^{N} U_{i\alpha} \tilde{a}_\alpha^\dagger \\
&= \sum_{\alpha=1}^{N} U_{i\alpha} \sum_{j=1}^{\infty} u_{\alpha j} a_j^\dagger \\
&= \sum_{\alpha=1}^{N} U_{i\alpha} \left(\sum_{j=1}^{N} u_{\alpha j} a_j^\dagger + \sum_{m=N+1}^{\infty} u_{\alpha m} a_m^\dagger \right) \\
&= \sum_{\alpha=1}^{N} \sum_{j=1}^{N} U_{i\alpha} u_{\alpha j} a_j^\dagger + \sum_{\alpha=1}^{N} \sum_{m=N+1}^{\infty} U_{i\alpha} u_{\alpha m} a_m^\dagger \\
&= \sum_{j=1}^{N} \delta_{ij} a_j^\dagger + \sum_{m=N+1}^{\infty} t_{mi} a_m^\dagger \\
&= a_i^\dagger + \sum_{m=N+1}^{\infty} t_{mi} a_m^\dagger \\
\bar{\psi}_i &= \left(a_i^\dagger + \sum_{m=N+1}^{\infty} t_{mi} a_m^\dagger \right) |0\rangle
\end{aligned}
\tag{C.14}
$$

Thus, any new orbital may be generated by mixing in contributions from virtual orbitals. We

apply this to generating a new single determinant below.

$$
\begin{aligned}
|\psi\rangle &= \prod_{i}^{N} \bar{a}_i^\dagger |0\rangle \\
&= \prod_{i}^{N} \left(a_i^\dagger + \sum_{m=N+1}^{\infty} t_{mi} a_m^\dagger \right) |0\rangle \\
&= \prod_{i}^{N} \left(1 + \sum_{m=N+1}^{\infty} t_{mi} a_m^\dagger a_i \right) a_i^\dagger |0\rangle \\
&= \prod_{i}^{N} \left(1 + \sum_{m=N+1}^{\infty} t_{mi} a_m^\dagger a_i \right) a_i^\dagger |0\rangle \\
&= \prod_{i}^{N} \prod_{m=N+1}^{\infty} \left(1 + \sum_{m=N+1}^{\infty} t_{mi} a_m^\dagger a_i \right) |\psi_0\rangle \\
&= e^{\hat{T}_1} |\psi_0\rangle
\end{aligned}
\tag{C.15}
$$

We got to the second to last step by realizing that $\prod_{i}^{N} a_i^\dagger |0\rangle = |\psi_0\rangle$, and $a_i a_i |\psi_0\rangle = 0$. The fact that all terms in which the same creation operator occurs more than once is also the reason we can write the infinite product as an exponential.

Appendix D

DERIVATION OF THE EOM-MBPT2 EQUATIONS

We begin our perturbative treatment of the coupled cluster Schrödinger equations by partitioning the normal ordered Hamiltonian into the one-particle component $\hat{F}_N$ and the two-particle component $\hat{V}_N$ as a perturbation, with λ as a scalar ordering parameter.

$$\hat{H}_N = \hat{F}_N + \lambda \hat{V}_N \tag{D.1}$$

Similarly, we expand the $\hat{T}$ operator perturbatively

$$\hat{T} = \lambda \hat{T}^{(1)} + \lambda^2 \hat{T}^{(2)} + \lambda^3 \hat{T}^{(3)} + \cdots \tag{D.2}$$

Because of the exponential parameterization, the coupled cluster Schrödinger equation can be written as the infinite series

$$\hat{H}_N e^{\hat{T}} |\Phi_0\rangle = \hat{H}_N |\Phi_0\rangle + \hat{H}_N \hat{T} |\Phi_0\rangle + \frac{1}{2} \hat{H}_N \hat{T}^2 |\Phi_0\rangle + \cdots \tag{D.3}$$

$$= (\hat{F}_N + \lambda \hat{V}_N) |\Phi_0\rangle \tag{D.4}$$

$$+ (\hat{F}_N + \lambda \hat{V}_N)(\lambda \hat{T}^{(1)} + \lambda^2 \hat{T}^{(2)} + \lambda^3 \hat{T}^{(3)} + \cdots) |\Phi_0\rangle \tag{D.5}$$

$$+ \frac{1}{2} (\hat{F}_N + \lambda \hat{V}_N)(\lambda \hat{T}^{(1)} + \lambda^2 \hat{T}^{(2)} + \lambda^3 \hat{T}^{(3)} + \cdots)^2 |\Phi_0\rangle + \cdots \tag{D.6}$$

Collecting terms of like order λ yields, with $\bar{H}_N = \hat{H}_N e^{\hat{T}}$

$$\bar{H}_N^{(1)} = \hat{V}_N + \hat{F}_N \hat{T}^{(1)} \tag{D.7}$$

$$\bar{H}_N^{(2)} = \hat{V}_N \hat{T}^{(1)} + \hat{F}_N \hat{T}^{(2)} + \frac{1}{2} \hat{F}_N \hat{T}^{(1)} \hat{T}^{(1)} \cdots \tag{D.8}$$

At this point, we note that the perturbative scheme is formally exact. However, truncating $\hat{T}$ to include only single and double excitations ($\hat{T}_1$ and $\hat{T}_2$, respectively), we have through second order

$$\bar{H}_N^{(1)} = \hat{V}_N + \hat{F}_N\hat{T}_1^{(1)} + \hat{F}_N\hat{T}_2^{(1)} \tag{D.9}$$

$$\bar{H}_N^{(2)} = \hat{V}_N\hat{T}_1^{(1)} + \hat{V}_N\hat{T}_2^{(1)} + \hat{F}_N\hat{T}_1^{(2)} + \hat{F}_N\hat{T}_2^{(2)} + \frac{1}{2}\hat{F}_N\hat{T}_1^{(1)}\hat{T}_1^{(1)} + \frac{1}{2}\hat{F}_N\hat{T}_2^{(1)}\hat{T}_2^{(1)} + \hat{F}_N\hat{T}_1^{(1)}\hat{T}_2^{(1)} \tag{D.10}$$

Assuming canonical Hartree-Fock orbitals, we find that through second order our Hamiltonian matrix elements are, for the singles-singles block:

$$\begin{aligned}\langle\Phi_i^a|\bar{H}\hat{R}_1|\Phi_0\rangle &= f_{ac}r_i^c - f_{ki}r_k^a + \langle ak||ic\rangle r_k^c \\ &\quad - \frac{1}{2}\langle mn||ce\rangle t_{mn}^{ae(1)}r_i^c - \frac{1}{2}\langle km||ef\rangle t_{im}^{ef(1)}r_k^a + \langle km||ce\rangle t_{mi}^{ea(1)}r_k^c\end{aligned} \tag{D.11}$$

for the singles-doubles block:

$$\langle\Phi_i^a|\bar{H}\hat{R}_2|\Phi_0\rangle = \frac{1}{2}\langle al||cd\rangle r_{il}^{cd} - \frac{1}{2}\langle kl||id\rangle r_{kl}^{ad} \tag{D.12}$$

for the doubles-singles block:

$$\begin{aligned}\langle\Phi_{ij}^{ab}|\bar{H}\hat{R}_1|\Phi_0\rangle &= P(ij)\langle ab||cj\rangle r_i^c - P(ab)\langle kb||ij\rangle r_k^a \\ &\quad + P(ij)P(ab)\langle am||ce\rangle t_{mj}^{eb(1)}r_i^c - P(ij)P(ab)\langle km||ie\rangle t_{mj}^{eb(1)}r_k^a \\ &\quad - \frac{1}{2}P(ab)\langle kb||ef\rangle t_{ij}^{ef(1)}r_k^a + \frac{1}{2}P(ij)\langle mn||cj\rangle t_{mn}^{ab(1)}r_i^c \\ &\quad + P(ab)\langle ka||ce\rangle t_{ij}^{eb(1)}r_k^c - P(ij)\langle km||ci\rangle t_{mj(1)}^{ab}r_k^c\end{aligned} \tag{D.13}$$

and finally the doubles-doubles block:

$$\begin{aligned}\langle\Phi_{ij}^{ab}|\bar{H}\hat{R}_2|\Phi_0\rangle &= P(ab)f_{bc}r_{ij}^{ac} - P(ij)f_{kj}r_{ik}^{ab} \\ &+ \frac{1}{2}\langle ab||cd\rangle r_{ij}^{cd} + \frac{1}{2}\langle kl||ij\rangle r_{kl}^{ab} + P(ij)P(ab)\langle kb||cj\rangle r_{ik}^{ac} \\ &+ \frac{1}{4}\langle mn||cd\rangle t_{mn}^{ab(1)} r_{ij}^{cd} + \frac{1}{4}\langle kl||ef\rangle t_{ij}^{ef(1)} r_{kl}^{ab} \\ &+ P(ij)P(ab)\langle km||ce\rangle t_{mi}^{ea(1)} r_{jk}^{bc} - \frac{1}{2}P(ij)\langle km||cd\rangle t_{mj}^{ab(1)} r_{ik}^{dc} \\ &- \frac{1}{2}P(ij)\langle mk||ef\rangle t_{im}^{fe(1)} r_{kj}^{ab} - \frac{1}{2}P(ab)\langle kl||ce\rangle t_{ij}^{eb(1)} r_{lk}^{ac} \\ &- \frac{1}{2}P(ab)\langle mn||ec\rangle t_{mn}^{ae(1)} r_{ij}^{cb} \end{aligned} \tag{D.14}$$

Where $P(pq)$ is an antisymmetric permutation operator,

$$P(pq) = 1 - \mathcal{P}(pq) \tag{D.15}$$

Where $\mathcal{P}(pq)$ permutes the indices of p and q. These equations define the EOM–MBPT2 method.[188] Terms involving $t_i^{a(1)}$ are always zero when using a canonical Hartree-Fock reference. This, as well as the expression for $t_{ij}^{ab(1)}$, can be determined in the same manner as the so-called $\hat{T}_1$ and $\hat{T}_2$ equations in CCSD, projecting the singly and doubly excited determinant on the CCSD ground-state equations. For $t_i^{a(1)}$,

$$\begin{aligned}\langle\Phi_i^a|\bar{H}^{(1)}|\Phi_0\rangle &= 0 \\ &= f_{ab}t_i^{b(1)} - f_{ij}t_i^{a(1)} \end{aligned} \tag{D.16}$$

By the diagonal nature of the canonical Fock matrix elements, $t_i^{a(1)} = 0$. In a similar manner,

$$\begin{aligned} \langle \Phi_{ij}^{ab} | \bar{H}^{(1)} | \Phi_0 \rangle &= 0 \\ &= \langle ij||ab\rangle - (f_{ii} + f_{jj} - f_{aa} - f_{bb}) t_{ij}^{ab(1)} \\ t_{ij}^{ab(1)} &= \frac{\langle ij||ab\rangle}{\epsilon_i + \epsilon_j - \epsilon_a - \epsilon_b} \end{aligned} \tag{D.17}$$

This is the expression for $t_{ij}^{ab(1)}$ used in the solution of the EOM–MBPT2 equations. They are completely determined, and therefore no CCSD iterative scheme must be used to compute them prior to the EOM solutions. The working equations may then be solved using non-Hermitian variants of the Davidson algorithm.[189–192]